Universidade de Aveiro
2010

Departamento de Física

Amélia Olga Gonçalves Ankiewicz

Propriedades de nanoestruturas de semicondutores magnéticos diluídos auto-organizados

Properties of self-assembled diluted magnetic semiconductor nanostructures

Universidade de Aveiro
2010

Departamento de Física

Amélia Olga Gonçalves Ankiewicz

Propriedades de nanoestruturas de semicondutores magnéticos diluídos auto-organizados

Properties of self-assembled diluted magnetic semiconductor nanostructures

dissertação apresentada à Universidade de Aveiro para cumprimento dos requisitos necessários à obtenção do grau de Doutoramento Europeu em Física, realizada sob a orientação científica do Professor Doutor Nikolai A. Sobolev, Professor Associado do Departamento de Física da Universidade de Aveiro e sob co-orientação científica do Professor Doutor Marius Grundmann, Director do Instituto de Física Experimental II da Universidade de Leipzig (Alemanha).

Apoio financeiro da FCT no âmbito do projecto PTDC/FIS/72843/2006 e da bolsa SFRH/BD/21659/2005.

Apoio financeiro da rede de excelência SANDiE da União Europeia.

Financially supported by FCT in the framework of the project PTDC/FIS/72843/2006, and of the bursary SFRH/BD/21659/2005.

Financially supported by the SANDiE network of excellence.

o júri

presidente

Prof. Doutora Ana Maria Vieira da Silva Viana Cavaleiro
professora catedrática, Departamento de Química, Universidade de Aveiro, Portugal

Prof. Doutor Nikolai A. Sobolev
professor associado, Departamento de Física, Universidade de Aveiro, Portugal (orientador)

Prof. Doutor Marius Grundmann
professor catedrático, director do Instituto de Física Experimental II, Universidade de Leipzig, Alemanha (co-orientador)
.

Prof. Doutor Wolfgang Gehlhoff
professor catedrático, Instituto de Física de Estado Sólido, Universidade Técnica de Berlim, Alemanha

Prof. Doutor Werner Wesch
professor catedrático, Instituto de Física do Estado Sólido, Universidade de Jena, Alemanha

Prof. Doutor Armando Neves
professor associado, Departamento de Física, Universidade de Aveiro, Portugal

Prof. Doutora Fátima Cerqueira
professor auxiliar, Departamento de Física, Universidade do Minho, Portugal

acknowledgments

There are several people I would like to thank, for different reasons.
First of all, I am very thankful to my supervisor Prof. Dr. Nikolai Sobolev, for proposing this work to me and for the support and guidance through it at all times. I am also thankful to Prof. Dr. Marius Grundmann for the supervision and help throughout my work, and for kindly receiving me at the University of Leipzig.
I have not enough words to express my gratitude to Prof. Dr. Wolfgang Gehlhoff for all the fruitful scientific discussions, for the experimental guidance, and above all for his friendship.
I thank all of the colleagues from the Institute of Experimental Physics II at the University of Leipzig for their help and availability during my stays in Germany. In the same way, I also thank all the colleagues from the Technical University of Berlin. Additional thanks to Mrs. Grupe, Mrs. Heck, and Mrs. Wendisch for their kindness and help.
I am grateful to all my colleagues from the Physics Department of the University of Aveiro, especially Rui, Nuno, and Joana, for their support during this long journey.
I also would like to thank all of my professors at the University of Aveiro, who significantly contributed for my personal and academic education, and who were always accessible.
And last, but not least, I thank my friends and family, particularly my husband Bruno, my parents, and my grandmother, for their love and care, and for being their at all moments.

palavras-chave Magnetismo, ZnO, metais de transição, ressonância magnética

resumo

Este trabalho centra-se na investigação da possibilidade de se conseguir um semicondutor magnético diluído (SMD) baseado em ZnO.

Foi levado a cabo um estudo detalhado das propriedades magnéticas e estruturais de estruturas de ZnO, nomeadamente nanofios (NFs), nanocristais (NCs) e filmes finos, dopadas com metais de transição (MTs). Foram usadas várias técnicas experimentais para caracterizar estas estruturas, designadamente difracção de raios-X, microscopia electrónica de varrimento, ressonância magnética, SQUID, e medidas de transporte.

Foram incorporados substitucionalmente nos sítios do Zn iões de Mn^{2+} e Co^{2+} em ambos os NFs e NCs de ZnO. Revelou-se para ambos os iões dopantes, que a incorporação é heterogénea, uma vez que parte do sinal de ressonância paramagnética electrónica (RPE) vem de iões de MTs em ambientes distorcidos ou enriquecidos com MTs. A partir das intensidades relativas dos espectros de RPE e de modificações da superfície, demonstra-se ainda que os NCs exibem uma estrutura *core-shell*. Os resultados, evidenciam que, com o aumento da concentração de MTs, a dimensão dos NCs diminui e aumentam as distorções da rede. Finalmente, no caso dos NCs dopados com Mn, obteve-se o resultado singular de que a espessura da *shell* é da ordem de 0.3 nm e de que existe uma acumulação de Mn na mesma.

Com o objectivo de esclarecer o papel dos portadores de carga na medição das interacções ferromagnéticas, foram co-dopados filmes de ZnO com Mn e Al ou com Co e Al. Os filmes dopados com Mn, revelaram-se simplesmente paramagnéticos, com os iões de Mn substitucionais nos sítios do Zn. Por outro lado, os filmes dopados com Co exibem ferromagnetismo fraco não intrínseco, provavelmente devido a decomposição *spinodal*.

Foram ainda efectuados estudos comparativos com filmes de ligas de $Zn_{1-x}Fe_xO$. Como era de esperar, detectaram-se segundas fases de espinela e de óxido de ferro nestas ligas; todas as amostras exibiam curvas de histerese a 300 K. Estes resultados suportam a hipótese de que as segundas fases são responsáveis pelo comportamento magnético observado em muitos sistemas baseados em ZnO.

Não se observou nenhuma evidência de ferromagnetismo mediado por portadores de carga. As experiências mostram que a análise de RPE permite demonstrar directamente se e onde estão incorporados os iões de MTs e evidenciam a importância dos efeitos de superfície para dimensões menores que ~15 nm, para as quais se formam estruturas *core-shell*.

As investigações realizadas no âmbito desta tese demonstram que nenhuma das amostras de ZnO estudadas exibiram propriedades de um SMD intrínseco e que, no futuro, são necessários estudos teóricos e experimentais detalhados das interacções de troca entre os iões de MTs e os átomos do ZnO para determinar a origem das propriedades magnéticas observadas.

keywords Magnetism, ZnO, transtion metals, magnetic resonance

abstract

This work focuses on the study of the possibility of achieving an intrinsic diluted magnetic semiconductor (DMS) based on ZnO.

Detailed investigations of the structural and magnetic properties of transition metal (TM) doped ZnO structures, namely nanowires (NWs), nanocrystals (NCs), and thin films, were carried out. Various experimental techniques, such as X-ray diffraction, scanning electron microscopy, transmission electron microscopy, magnetic resonance, SQUID, and transport measurements were employed to structurally and magnetically characterize these samples.

For both the ZnO NWs and NCs, Mn and Co ions were successfully incorporated as substitutional Mn^{2+} or Co^{2+}, respectively, on Zn sites. For both types of doping, the TM incorporation was heterogeneous, since part of the electron paramagnetic resonance (EPR) spectrum stemmed from TM ions in distorted or TM enriched environments. Furthermore, in the case of the NCs, the relative intensities of the EPR spectra and surface modifications showed that the NCs exhibit a core-shell structure. Moreover, the results evidence decreasing NC size and increasing lattice distortions for increasing TM content. Finally, in the case of the Mn doped NCs, we were able to obtain the unique result that the shell thickness is very small, in the order of 0.3 nm, and that there is an accumulation of the Mn ions in the shell.

To clarify the role of charge carriers in mediating ferromagnetic interactions, Mn, Al and Co, Al co-doped ZnO films were investigated. The Mn doped ZnO samples were clearly paramagnetic, the Mn ions being substitutional on Zn sites. On the other hand, the Co doped samples exhibited weak ferromagnetic order, which we believe to most probably arise from spinodal decomposition.

Additionally, comparative investigations of Fe alloyed ZnO films were performed. As expected, second phases of spinel and iron oxide were found, and the samples exhibited ferromagnetic hysteresis loops at 300 K. These results support the indication that secondary phases are accountable for the magnetic behaviour detected in many ZnO systems.

No evidence of carrier mediated ferromagnetism was observed. The experiments show that the EPR analysis allows us to directly demonstrate whether and where the TM ions are incorporated and evidence the importance of the surface effects at material dimensions below ~15 nm, for which core-shell structures are formed.

The research carried out in the framework of this thesis demonstrates that for all studied samples, ZnO did not exhibit the behaviour of an intrinsic DMS, and in the future very detailed element specific investigations, both experimental and theoretical, of the exchange interactions of the transition metal ions with the ZnO host are necessary to assert the nature of the magnetic properties.

To my grandmother,

Amélia;

my husband,

Bruno;

and my daughter,

Inês Sofia.

TABLE OF CONTENTS

LIST OF PUBLICATIONS

1. A. O. Ankiewicz, W. Gehlhoff, J. S. Martins, A. S. Pereira, S. Pereira, A. Hoffmann, E. M. Kaidashev, A. Rahm, M. Lorenz, M. Grundmann, M. C. Carmo, T. Trindade, and N. A. Sobolev, *Magnetic and structural properties of transition metal doped zinc-oxide nanostructures*, Physica Status Solidi (b), **246**, 766 (2009).

2. A. S Pereira, A. O. Ankiewicz, W. Gehlhoff, A. Hoffmann, S. Pereira, T. Trindade, M. Grundmann, M. C. Carmo, and N. A. Sobolev, *Surface modification of Co-doped ZnO nanocrystals and its effects on the magnetic properties*, Journal of Applied Physics, **103**, 07D140 (2008).

3. A. O. Ankiewicz, W. Gehlhoff, E. M. Kaidashev, A. Rahm, M. Lorenz, M. Grundmann, M. C. Carmo, and N. A. Sobolev, *Electron Paramagnetic Resonance Characterization of Mn- and Co-Doped ZnO Nanowires*, AIP Conf. Proc., **893**, 63 (2007).

4. A. O. Ankiewicz, W. Gehlhoff, E. M. Kaidashev, A. Rahm, M. Lorenz, M. Grundmann, M. C. Carmo, and N. A. Sobolev, *Electron Paramagnetic Resonance in Transition Metal –Doped ZnO Nanowires*, Journal of Applied Physics, **101**, 024324 (2007).

5. A. O. Ankiewicz, N. A. Sobolev, J. P. Leitão, M. C. Carmo, R. N. Pereira, J. Lundsgaard Hansen, e A. Nylandsted Larsen, *Effect of Ge incorporation on the creation of luminescent defects in Si*, Nuclear Inst. and Methods in Physics Research B, **248**, 127 (2006).

LIST OF FIGURES

LIST OF TABLES

LIST OF ACRONYMS

AFC	automatic frequency control
AHE	anomalous Hall effect
BSE	backscattered electrons
CF	crystal field
CL	Cathodoluminescence
DMS	diluted magnetic semiconductor
DMSO	Dimethylsulfoxide
EDS	energy dispersive x-ray spectroscopy
EMR	electron magnetic resonance
EPR	electron paramagnetic resonance
EXAFS	extended X-ray absorption fine structure spectroscopy
FC	field cooling
FMR	ferromagnetic resonance
FS	fine structure
FWHM	full width at half maximum
HF	Hyperfine
LDA	local density approximation
MOCVD	metalorganic chemical vapour deposition
MR	Magnetoresistance
NC	Nanocrystal
NMR	nuclear magnetic resonance
NW	Nanowire
PIMOCVD	pulsed injection metalorganic chemical vapour deposition
PIXE	particle induced X-ray emission
PLD	pulsed laser deposition
PS	Polystyrene
RBS	Rutherford backscattering
RKKY	Ruderman-Kittel-Kasuya-Yosida
RSM	reciprocal space map
SEM	scanning electron microscopy
SH	spin Hamiltonian
SQUID	superconducting quantum interference device
TEM	transmission electron microscopy
TM	transition metal
TOPO	trioctylphosphine oxide
XMCD	X-ray magnetic circular dichroism
XPS	X-ray photoelectron spectroscopy
XRD	X-ray diffraction
ZFC	zero field cooling

ZFS	zero field splitting

LIST OF SYMBOLS

A	hyperfine constant
$\mathbf{A}$	hyperfine tensor
a	lattice parameter; cubic fine structure parameter
a_B	Bohr radius
B	magnetic field
$\mathbf{B}_1$	magnetic component of the microwave radiation
B_C	coercive field
C	Covalency
c	lattice parameter
D	axial fine structure parameter
$\mathbf{D}$	spin-spin interaction tensor
d	thickness; diameter
d_{hkl}	distance between lattice planes
E	energy; orthorhombic fine structure parameter
e	electron charge
E_g	band gap energy
$\mathbf{F}$	Force
F	fine structure parameter
g	g-factor
g_N	nuclear g-factor
$\mathscr{H}$	Hamiltonian operator
h	Planck constant
$\mathbf{I}$	nuclear spin operator
I	nuclear spin; intensity; current flow
K	anisotropy constant; Scherrer constant
k_F	Fermi wave vector
L	orbital quantum number
$\mathbf{L}$	total orbital angular momentum operator
l	mean free path; sample length
l, m, n	direction cosines
$\mathbf{l}_k$	individual orbital angular momentum
m	electron mass; number of nearest neighbours
M	Magnetization
m_I	nuclear spin quantum number
m_p	proton mass
M_S	electron spin quantum number

M_{Sat}	saturation magnetization
N	free carrier concentration; integer
N	number of centres
n_C	critical electron concentration
Q	nuclear quadrupole moment
q	Charge
r	mean distance between donors
r	Radius
R	electrical resistance
R_H	Hall coefficient
R_S	anomalous Hall coefficient
S	electron spin operator
S	electron spin
$\hat{S}$	effective spin
t	time; thickness
T	Temperature
T_C	Curie temperature
T_N	Néel temperature
U	crystalline potential
v	Velocity
V	Volume
W	line width
Z	atomic number
$\alpha_1, \alpha_2, \alpha_3$	direction cosines
β	Bohr magneton
β_N	nuclear magneton
γ	gyromagnetic ratio
δ	full width at half maximum
ΔB_{pp}	peak to peak line width
ε	effective particle size
ζ	effective strain
θ	polar angle between the quantization axis and the applied magnetic field (EPR); polar angle defining the orientation of the magnetization vector (FMR); incident angle (XRD)
λ	Wavelength
μ	magnetic dipole operator
μ	carrier mobility
μ_0	magnetic permeability of free space
ν	Frequency
ϱ	Resistivity

σ	Conductivity
φ	polar angle between the projection of the applied magnetic field in the *XY* plane and the *Y*-axis direction (EPR); azimuthal angle (FMR)
χ	magnetic susceptibility
ψ	wave function
Ω	relative orientation between a paramagnetic centre and the laboratory frame
ω	angular frequency
ω_0	Larmor frequency

1 INTRODUCTION

A renewed interest in the investigation of ZnO, a wide band gap semiconductor, has been prompted by the recent developments in the areas of transparent conductors for applications in photovoltaics and flat panel displays [Iwata (2005)], ferromagnetic semiconductors for spintronics [Pan (2008)], and the possibility of applying doped ZnO in photoelectrochemical water splitting [Wolcott (2009)].

The wide-band-gap zinc oxide-based diluted magnetic semiconductors (DMSs), in which a fraction of non-magnetic elements is substituted by magnetic transition metal (TM) ions, currently attract considerable attention due to their possible applications in spintronic and UV devices [Heo (2004*b*), Wang (2004), Pan (2008)]. Recently a new paradigm of electronics based on the spin degree of freedom of the electron, which places electron spin rather than charge at the very centre of interest, has began to emerge. The underlying basis for this new technology is to simultaneously use charge and electron degrees of freedom. Instead of using the spin only for storage information in magnetic-recording devices and, independently, the electron charge for information processing in semiconductor high frequency devices, there is a new goal for processing and storing information in a unique device by combining the use of spin and charge. Information can be encoded through the alignment of a spin (either "up" or "down") relative to a reference. These novel devices would be non-volatile, have high processing speed, low power consumption, and increased integration densities compared with the conventional semiconductor devices.

One of the triggers for the development of this field was the prediction by Dietl *et al.* (2000) of high temperature ferromagnetism in some magnetically doped wide-band-gap *p*-type semiconductors. Even though the *ab initio* calculations predicted that the incorporation of V, Cr, Fe, Co, or Ni in ZnO in the 5-25 % concentration range should give rise to metallic behaviour and a ferromagnetic state without need of additional doping [Katayama-Yoshida (2002), Sato (2000)], the experimental results are quite controversial even for bulk materials. For Mn and Co doped ZnO films, only weak ferromagnetism has usually been found [Diaconu (2005*a*), Sharma (2003), Ueda (2001)]. More recently, a giant magnetic moment of 6.1 β/Co and a high Curie temperature of 790 K have been observed in isolating ZnO films doped with 4 at. % Co grown at low temperature (200ºC) [Song (2006)]. As to nanostructures, their magnetic properties can be

completely different from their bulk counterparts [Liu (1998), Ohno (1999), Sellmyer (2001), Yu (2001)].

The work presented in this thesis aims to contribute to the clarification of the fundamental properties of magnetically doped ZnO. One of the crucial issues addressed here is the relation between the incorporation of the magnetic ions and the observation of intrinsic magnetic properties. Three kinds of magnetically doped ZnO structures were studied; namely nanowires, nanocrystals, and thin films. The main finding was that the studied materials do not exhibit a DMS behaviour and that the incorporation of the TM ions into the host lattice does not produce any ferromagnetic interaction for any of these structures. Furthermore, the investigations evidence the importance of surface effects for material dimensions inferior to ≈15 nm.

This thesis is organized in the following way: in chapter 2 the basic properties of ZnO are described and a summary of the current understanding in the field of ZnO-based DMSs is given; the theoretical fundaments of electron paramagnetic resonance and ferromagnetic resonance are introduced in chapter 3; chapter 4 contains the description of the experimental techniques; in chapters 5 – 8 the own experimental results are presented and discussed; finally, chapter 9 contains the summary of the main results, conclusions and the outlook for future work.

2 STATE OF THE ART

Magnetic semiconductors combining properties and functionalities of both semiconductors and ferromagnets have been driving an enormous scientific activity due to their potential applications in spintronics [Liu (2005)], where logic and memory operations could in principle be flawlessly integrated on a single device, and taking advantage of the already established fabrication processes. Diluted magnetic semiconductors (DMSs) are especially interesting for devices such as spin-based light-emitting diodes, sensors and transistors that use spin in addition to charge [Furdyna (1988)]. The main objective in the research field of DMSs for devices is the synthesis, characterization and application of semiconductors which exhibit significant carrier spin polarization at and above room temperature. In these materials, ferromagnetism is achieved by the incorporation of transition metals (TMs) (Sc, Ti, V, Cr, Mn, Fe, Co, Ni, and Cu) or rare earths (*e.g.* Eu, Gd, Er) into the semiconductor host. Both types of ions have partially filled *d* or *f* shells, respectively, which give rise to non-zero electron spin. There are many mechanisms that could produce magnetic ordering, and many of these could be present simultaneously. The discussion of the individual processes, particularly of the dominant ones, can be very enlightening. In DMSs, the delocalized conduction band electrons and valence band holes interact with the localized magnetic moments of the magnetic atoms. In general, when 3*d* TM ions substitute the cations of the host, the resultant electronic structure suffers strong hybridization of the 3*d* orbitals of the magnetic ion and mainly of the *p* orbitals of the neighbouring host anions. This hybridization originates a strong magnetic interaction between the localized 3*d* spins and the carriers in the host valence band [Furdyna (1988)]. The macroscopic magnetic behaviour is found to be strongly dependent on a number of parameters, including the concentration of the magnetic ions, the carrier density, and the crystal quality. Hence, the preparation methods play a crucial role in obtaining true DMSs. A major challenge is to prevent the formation of second phases that may dominate the magnetic properties of the semiconductor, since the magnetic ion concentrations are usually well above the solubility limits. These difficulties in maintaining single-phase diluted material, and the typical low magnetization produced by the diluted magnetic ions have raised large controversy in the scientific reports. The most usual DMSs, as for instance (Ga,Mn)As, exhibit relatively low Curie temperatures (T_C) (<≈170 K) [Nazmul (2002)], which limits their potential applications. The exchange coupling

between the dopant spins and the valence or conduction band carriers, the interaction responsible for the carrier spin polarization, is known to be sufficiently weak in conventional semiconductors such as GaAs, Si and Ge, so that magnetic ordering above cryogenic temperatures is extremely difficult to attain. On the other hand, in the beginning of the 21st century, the wide band gap materials GaN and ZnO seemed much more promising for obtaining high T_C [Erwin and Hellberg (2003)]. Figs. 2.1 and 2.2 illustrate this statement. Note that the wider the band gap, the larger the *p-d* hybridization, the smaller the spin-orbit interaction, and the smaller the lattice constants. Among the promising wide-band gap materials, ZnO is especially attractive because it is widely used in electronic applications, meaning that DMSs based on ZnO could be easily incorporated in the existing technologies. The theoretical predictions and the combination of the properties of ZnO inspired researchers all around the world, and a plethora of scientific reports appeared. It is worth mentioning that the theoretical assumptions, namely the high hole concentration, used by Dietl *et al.* (2000) have not yet been achieved for ZnO.

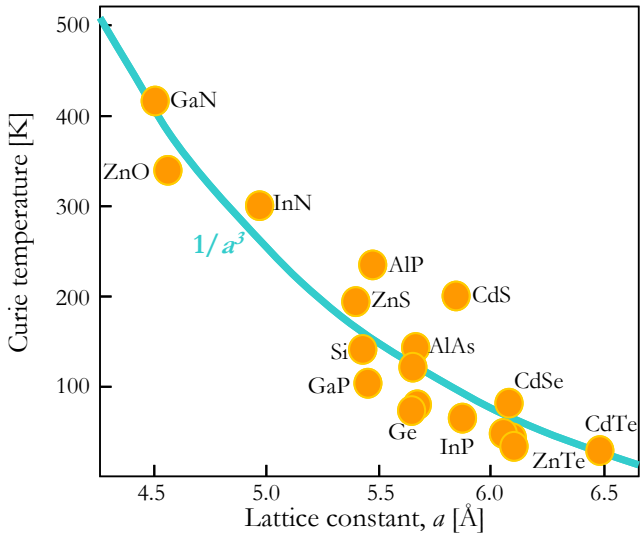

Fig. 2.1. Predicted Curie temperature as a function of the lattice constant for a variety of semiconductors [after S. C. Erwin (Naval Research Laboratory)]. This prediction is based on the full numeric evaluation of the mean-field solution of the Zener model for different host semiconductors [Erwin and Hellberg (2003)].

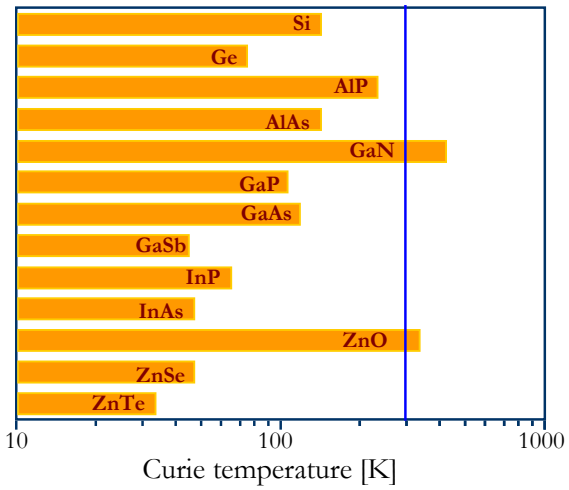

Fig. 2.2. Predicted Curie temperature as a function of the band gap [taken from Dietl (2000)]. The Curie temperatures were computed for various types of *p*-type semiconductors containing 5% Mn and 3.5×10^{20} holes per cm^3.

2.1 ZnO – THE HOST SEMICONDUCTOR

ZnO is an inorganic compound that normally crystallizes in the wurtzite (hexagonal) crystal structure as illustrated in Fig. 2.3, which is thermodynamically stable at normal ambient conditions, with lattice parameters of $a = 3.24982$ Å and $c = 5.20661$ Å [Maensiri (2006)]. Note that the lattice parameters are somewhat dependent on the free carrier and/or point defects concentrations. The oxygen atoms are arranged in a hexagonal close-packed lattice and the zinc atoms occupy half of the tetrahedral voids. The Zn atoms are tetrahedrally coordinated to four O atoms, where the Zn *d* electrons hybridize with the O *p* electrons. The structure is, thus, relatively open with all the octahedral and half the tetrahedral voids unoccupied. The Zn-O chemical bonding is essentially polar. However, there is a homopolar component of binding between the next nearest zinc and oxygen ions in the direction of the *c*-axis. A set of relevant physical properties of ZnO is given in Table 2.1.

ZnO is a direct gap semiconductor which exhibits strong luminescence in the UV, and has a stable exciton with binding energies up to 100 meV in superlattices [Chia (2003)]. Thus, stable laser operation at room temperature is achievable. Additionally, high-quality epitaxial films exhibit electron mobilities of 300 $cm^2\ V^{-1}\ s^{-1}$ at room temperature [Tsukazaki (2005)], and high saturation velocity of the electrons. Hence, there are possibilities for spin-based electronics and

optoelectronics using ZnO as the host semiconductor, given that it can be doped in a way that there is spin polarization in the majority carrier band.

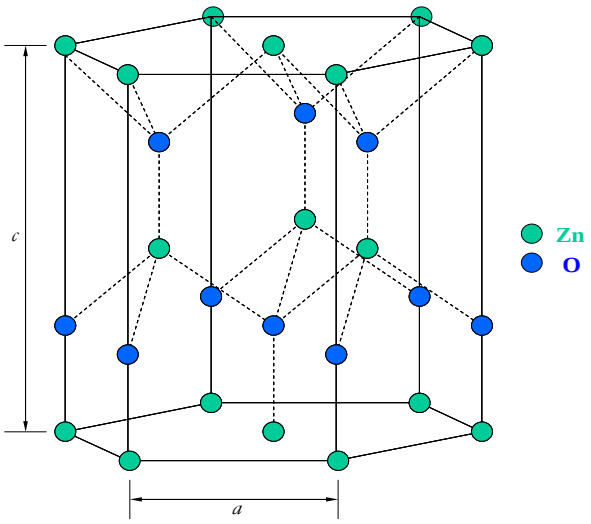

Fig. 2.3. Schematic representation of the ZnO wurtzite crystal structure.

Table 2.1. List of relevant physical properties for bulk wurtzite ZnO.

Physical property	ZnO	Reference
Lattice constants: *a*, *c*	3.24982 Å, 5.20661 Å	[Maensiri (2006)]
Band gap energy at 300 K	3.37 eV	[Özgür (2005)]
Exciton binding energy	60 meV	[Özgür (2005)]
Dielectric constants ε_∞, ε_0	3.52, 8.0	[Bundesmann (2002), (2006)]
Melting point	1975 ºC	[Özgür (2005), Triboulet (2003)]
Thermal conductivity	0.54 W cm^{-1} K^{-1}	[Triboulet (2003)]
Density	5665 Kg m^{-3}	[Jagadish and Pearton (2006)]

ZnO is readily doped *n*-type using Al, Ga, H, interstitial Zn, and intrinsic defects. It is much harder to dope ZnO *p*-type. The fact that ZnO has a relatively large band gap (3.37 eV at 300 K) combined with its high electron affinity (4.35 eV) makes it difficult to find acceptors with states that are easily ionized in ZnO at room temperature, since its valence band maximum is sufficiently far below the vacuum level. The problem is aggravated by the facility with which ZnO is doped *n*-type. The significant compensation of acceptors by unintentional donors, such as native defects or Al coming from sapphire substrates, limits achievable hole concentrations [Claflin (2006)]. Nevertheless, the natural candidates for *p*-type dopants in ZnO are the Group

15 anions. Despite the difficulties, numerous experimental results of *p*-type conductivity have been reported for various dopants in ZnO epitaxial layers, nanowires and bulk crystals [Liu (2003), Lin (2004), Lee (2004), Look (2005a), Xiang (2007), Cao (2008a), Cao (2008b)].

Intrinsic defects are one of the key features for understanding charge mechanisms in semiconductors. Local density approximation (LDA) calculations have explained why certain intrinsic defects tend to dope ZnO *n*-type and why others, such as the oxygen vacancy (V_O), are not expected to be shallow donors, regardless of the general conviction that they should be. Zhang's *et al.* (2001) calculations demonstrate that the formation energy of the interstitial Zn (Zn_{int}), which is a known shallow donor in ZnO [Thomas (1957), de la Cruz (1992)], is low under both Zn- and O-rich conditions. Furthermore, these calculations show that defects that would compensate Zn_{int}, such as O_{int} or Zn vacancies (V_{Zn}), have high formation energies. Similarly, although O_{int} and V_{Zn} are intrinsic acceptors, these defects' high formation energies prevent their spontaneous formation. Additionally, calculations by Janotti and Van de Walle (2005) demonstrate that the V_O defect, thought to be a shallow donor in ZnO, is in fact ineffective as a donor because its formation energy is predicted to be rather high (3.5 eV), and its ionization energy also is sufficiently high, so that even if V_O did form, it would not be thermally ionized at room temperature. Recent positron annihilation experiments on ZnO single crystals irradiated with 2 MeV electrons are consistent with V_O being a deep donor and V_{Zn} a deep acceptor [Tuomisto (2005)].

Other native defects in ZnO may be electrically active dopants as well, at least under certain preparation conditions. For example, Look *et al.* (2005b), from a detailed analysis of low-temperature photoluminescence spectra, suggested the formation of a defect complex consisting of Zn_{int} and substitutional N, being a shallow donor in bulk ZnO containing N impurities.

An additional interesting aspect is the observation of long spin lifetimes (188 ps) at room temperature in non-magnetically *n*-type doped ZnO [Ghosh (2005)], since practical spintronic applications require long spin coherence times.

Another advantage of ZnO is that it can be rather easily grown as single crystals, thin films, nanocrystals, and nanowires by different methods. Furthermore, this material has a low refractive index (2.0), is strongly resistant to high energy irradiation and has low toxicity [Özgür (2005)]. The combination of these properties makes ZnO an attractive material for several applications, such as optoelectronics, for producing light emitting devices.

2.2 Synopsis of current understanding on ZnO based DMSs

The theory explaining the physical processes responsible for ferromagnetism in DMSs is still not fully understood. Zener (1951a), (1951b), (1951c) first proposed that ferromagnetism was due to the exchange interaction between carriers and localized magnetic ions, indicating that simple superexchange between the magnetic ions does not produce a ferromagnetic interaction, but that indirect carrier mediated superexchange does. As a result, the DMS character is induced by the exchange interaction between the localized *d* shell electrons of the magnetic ions and the delocalized band carrier states (of the *s* or *p* origin). More recently, there have been several attempts to explain the experimental observations by developing models based on the mean-field theory, first principle calculations, and bound magnetic polarons (see Fig. 2.4).

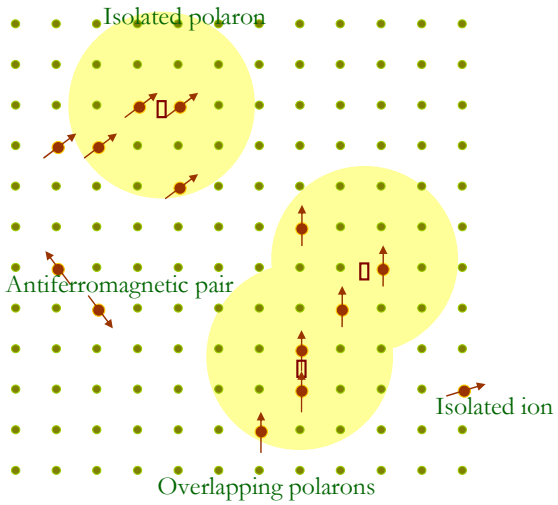

Fig. 2.4. Diagram illustrating magnetic polarons. A donor electron in its hydrogenic orbit couples with its spin anti-parallel to impurities with a 3*d* shell that is half-full or more than half-full. The figure is drawn for a magnetic cation concentration $x = 0.1$ and when the orbital radius of the magnetic cation is sufficiently large. Cation sites are represented by small circles. Oxygen is not shown; the unoccupied oxygen sites are represented by squares. (Taken from Coey *et al.* (2005)).

For instance, Coey *et al.* (2005) proposed the spin-split-orbit model, schematized in Fig. 2.5, which postulates that the ferromagnetism is mediated by shallow donor electrons that form bound magnetic polarons which, in turn, overlap to create a spin-split impurity band. The bound magnetic polarons are formed by the alignment of the spins of many transition-metal ions with that of much lower number of weakly bound carriers such as excitons within a polaron radius. The magnetic ions in different charge states couple virtually by the hopping of the "extra" electron from one ion to the other. Basically, the 3*d* electrons in the partially filled 3*d*

orbitals of neighbouring TM ions are allowed to hop between each other if the latter have parallel magnetic moments. Hence, the ferromagnetic exchange interaction is mediated by charge carriers in a spin-split impurity band formed by extended donor states; the impurity states hybridize with the *d* orbits of the TM ions.

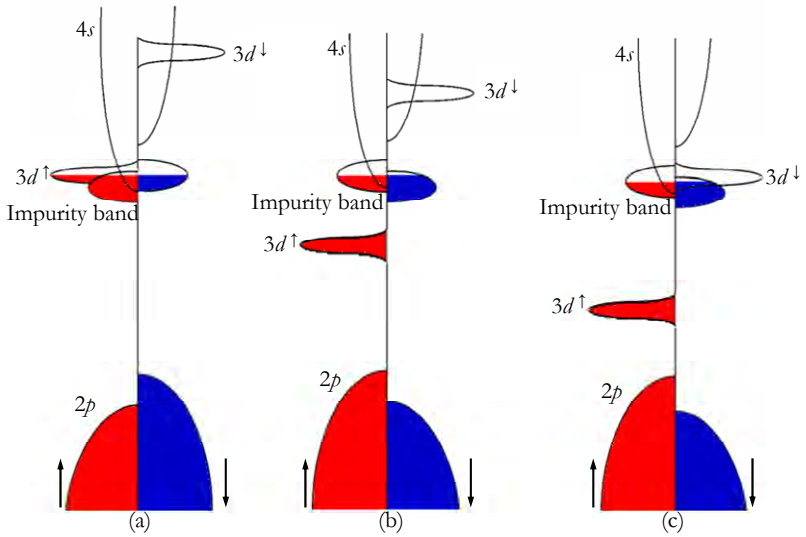

Fig. 2.5. Schematic density of states for (a) TM = Ti, (b) TM = Mn, and (c) TM = Co in TM-doped ZnO. The Fermi level lies in a spin-split donor impurity band. In the middle of the series, there is no overlap with the 3*d* levels, and exchange is weak, but towards the end of the series, the 3*d*↓ states overlap with the impurity band (c), which then has the opposite spin splitting for the same occupancy. High Curie temperatures would be found whenever unoccupied 3*d* states overlap with the impurity band, but not otherwise [Coey (2005)].

Of course, these models have limitations. However, it is very difficult, if not impossible, to find a universal model to explain all the observed DMS features, such as the wide range of Curie temperatures found for the same material [Pearton (2007)]. It should also be noted that the nature of the hybridization of the Mn 3*d* states and host *p*-states strongly depends on their relative energy position in the band structure, and that it would require substantial modifications to existing simple theories in order for them to successfully describe ferromagnetism in different semiconductors, such as GaN and ZnO. Nevertheless, sophisticated first-principles calculations have been carried out for a number of specific material systems since 2000 [see the review of Pearton *et al.* (2007)]. Very recently, Raebiger *et al.* (2009) reported interesting calculations, using a band-structure-corrected theory, which demonstrate that among the $3d^1$ – $3d^8$ series, the early Sc, Ti, and V are shallow donors, and that only the late Co and Ni have acceptor transitions in ZnO. The authors further show that long-range ferromagnetic interactions emerge due to partial

filling of 3*d* resonances inside the conduction band and, in general, require electron doping from additional sources.

Research on magnetic semiconductors is not so recent. In the 1980's, Story *et al.* (1986) demonstrated carrier mediated ferromagnetism in bulk $[(PbTe)_{1-x}(SnTe)_x]_{1-y}[MnTe]_y$ ($x = 0.72$, $y = 0.03$). Early on, II–VI compounds (such as CdTe, ZnSe, CdSe, CdS, etc.) doped with TM ions substituting their original cations were the most commonly studied DMSs [Furdyna (1988)]. However, these materials became less attractive for applications due to their low Curie temperatures and somewhat to the difficulty in doping these II–VI based DMSs *p*- and *n*-type. On the other hand, the conventional III–V semiconductors have been extensively applied for high speed electronic and optoelectronic devices [Liu (2005)]. More recently, the discovery of carrier mediated ferromagnetism in (Ga,Mn)As up to 172 K [Nazmul (2002)] renewed the interest in searching for new DMSs that retain their properties at and above room temperature. The properties of (Ga,Mn)As may be used as standards to test the authenticity of new candidates for high T_C DMSs. For instance, at low Mn concentrations ($x < 0.01$) the conductivity is reasonably low, nevertheless, the material exhibits ferromagnetic ordering at low temperatures, due to the formation of bound magnetic polarons [Chambers (2006)]. For $0.015 < x < 0.07$, the Mn-induced hole concentration scales with the Curie temperature, indicating a direct correlation between conductivity and magnetization [Matsukura (1998)]. Additionally, anomalous Hall effect measurements have shown that itinerant holes interact strongly with the Mn spin moments, and the ferromagnetism was claimed to have its origin in the Ruderman-Kittel-Kasuya-Yosida (RKKY) interaction mediated by holes [Matsukura (1998)]. X-ray magnetic circular dichroism (XMCD) measurements support the attribution of the origin of the observed ferromagnetism to a spin inequality in Mn-derived hole band states [Edmonds (2005)]. Furthermore, spin polarized carriers can be successfully injected from (Ga,Mn)As as demonstrated by polarized light emission from nonmagnetic quantum well structures in which (Ga,Mn)As works as a spin-polarized hole injector [Ohno (1999), Chye (2002), Van Dorpe (2004)]. Very recentely, Chiba *et al.* (2008) were able to electrically manipulate the magnetization in (Ga,Mn)As. The principle behind this research is that the magnetic anisotropy, which determines the magnetization direction, depends on the charge carrier concentration. Therefore, by applying an electric field using a metal-insulator-semiconductor structure, the authors were successful in controlling the hole concentration and, thereby, the magnetic anisotropy, allowing the manipulation of the magnetization direction. The advantage of this method is that it does

not require flowing currents in the device, but only the application of voltage. It is therefore highly compatible with the existing metal-oxide semiconductor technology used in microprocessors and random-access memory devices [Saitoh (2008)].

Large activity has been taking place in the investigation of novel DMSs based on GaN and ZnO since Dietl *et al.* (2000) predicted that these materials could exhibit ferromagnetism above room temperature, in the case of them being *p*-type (on the order of 10^{20} holes.cm^{-1}) and doped with ≈5 % Mn. In basic terms, this is to some extent due to the strong *p-d* hybridization that engages the valence band in the host. In this approach, the keys to a high T_C are a high density of states at the Fermi level and a large value of the *p-d* exchange integral. Furthermore, Sato *et al.* (2000) predicted that the ferromagnetic state $Co^{2+}(d^7)$ in Co doped *n*-type ZnO could be stabilized by *s-d* hybridization, indicating another possibility of achieving high Curie temperatures. Since these challenging theoretical predictions of Curie points above room temperature and the observation of room-temperature ferromagnetism in Co doped anatase TiO_2 [Matsumoto (2001)], one of the most interesting and stimulating scientific developments of the early 21st century has been the study of semiconductors doped with TMs with unpaired *d* electrons.

In the case of ZnO, the solubility of TM elements, namely Mn and Co, can reach up to 35% [Liu (2005)]. However, experimentally it is very difficult to obtain robust *p*-type doping of ZnO in the presence of high concentrations of TMs. The Mn doping is particularly attractive because the only potential second phase that contributes to the ferromagnetism is Mn_3O_4 with a Curie temperature below 50 K. Conversely, Co doping is more complicated, since Co in the metal form is ferromagnetic. On the other hand, in both ZnO thin films [Fukumura (2001)] and nanocrystalline powders [Mandal (2006)], the solubility limit for Fe was shown to be lower than 5 at. %, and the formation of Fe oxide secondary phases was concluded for values exceeding this limit.

Early on, Ueda *et al.* (2001) used pulsed laser deposition (PLD) to grow ZnO doped with Co, Mn, Cr and Ni. From the several dopant-host combinations, only Co doped ZnO was found to be ferromagnetic with a T_C of ≈280-300 K, and differences in magnetization were assumed to be due to differences in conductivity, indicating some form of carrier-mediated exchange interaction. However, other possibilities, such as magnetic secondary phase formation, could not be ruled out. Indeed, the magnetic moments per Co atom (1.8-2.0 β) were close to that of Co metal (1.7 β).

Kim *et al.* (2002) used PLD to grow paramagnetic and highly resistive epitaxial Co doped ZnO and found that for substrate temperatures below 600ºC and oxygen partial pressure $>\approx 10^{-5}$ Torr, homogeneous solid solutions could be grown for $x < \approx 0.25$. But, when changing the substrate temperature to 700ºC and the oxygen partial pressure to 10^{-6} Torr, they obtained Co metal precipitates, with the expected appearance of Co induced ferromagnetism and much lower resistivity as a result of partial film reduction. They also found experimental evidences of spin-glass behaviour in some of the $Zn_{1-x}Co_xO$ films. Conversely, polycrystalline powder samples of $Zn_{1-x}Co_xO$ have been found to be antiferromagnetic [Yoon (2003)].

Tuan *et al.* (2004) grew epitaxial Co doped ZnO by metalorganic chemical vapour deposition (MOCVD) and found that the material was consistently paramagnetic and highly resistive as grown. However, annealing in vacuum resulted in *n*-type conductivity and weak ferromagnetism between 5 K and 340 K. In contrast, PLD grown Co doped ZnO films, with various electron concentrations up to 4.61×10^{19} cm^{-3} at room temperature, showed only paramagnetism down to 2 K [Xu (2009)]. The authors also found that clustering instead of a uniform distribution of Co^{2+} ions may play a role, since a clear anomalous Hall effect was observed in the highly conducting Co doped ZnO films.

Recent investigations of Kaspar *et al.* (2008a) found no significant room temperature ferromagnetism in PLD grown Co doped ZnO thin films, for *n*-type conductivities in the range of 10^{-4}-10^{-5} Ω.cm, indicating that itinerant conduction band electrons alone are not sufficient to induce ferromagnetism in this system, even when the carrier concentration is a significant fraction of the magnetic dopant concentration. After annealing in Zn vapour, the Co doped ZnO thin films became weakly ferromagnetic [Kaspar (2008b)], but this ferromagnetism was proved not intrinsic, since X-ray photoelectron spectroscopy (XPS) depth profiling showed the presence of Co(0), and X-ray absorption fine structure indentified the CoZn ferromagnetic secondary phase. In contrast, Xu *et al.* (2008a) brought new hope for this material having found tunnelling magnetoresistance at 5 K in magnetic tunnel junctions with Co doped ZnO as a bottom ferromagnetic electrode and Co as a top ferromagnetic electrode prepared by PLD, demonstrating the spin polarization in Co doped ZnO.

As in the case of epitaxial film growth, wet chemical synthesis of Co doped ZnO has produced a range of results. For instance, Risbud *et al.* (2003) thermally decomposed mixed Co and Zn oxalates to produce $Zn_{1-x}Co_xO$ precipitates, yet none of the samples exhibited ferromagnetism. In contrast, Schwartz *et al.* (2003) found ferromagnetism in $Zn_{0.964}Co_{0.036}O$

nanoparticles grown by a reaction of Zn and Co acetates with ethanolic $N(CH_4)_4OH$. Recently, Belghazi *et al.* (2009) grew Co doped and Co,Al co-doped ZnO films by sol-gel process, and found weak ferromagnetism. Nevertheless, the comparative investigations between the two types of films showed no impact of the charge carriers on the magnetic behaviour of the material.

Despite the fact that the predictions only support ferromagnetism in *p*-type (Zn,Mn)O, there have been experimental reports on ferromagnetism in insulating (Zn,Mn)O [Jung (2002)] and *n*-type (Zn,Mn)O [Heo (2004a), Norton (2003b), Philipose (2006)]. Sharma *et al.* (2003) also showed that carrier-induced ferromagnetism can be obtained in either *p*-type or *n*-type ZnO with Mn concentration < 5 at.%. Later, Kundaliya *et al.* (2004) showed that processing (Mn, Zn)O under conditions similar to those used by Sharma *et al.* (2003) results in the formation of a vacancy stabilized and highly-defective Zn-doped Mn_2O_3 phase, rather than Mn doped ZnO. On the other hand, there are reports on PLD grown Mn doped ZnO films which exhibit either spin glass behaviour [Fukumura (2001)], weak ferromagnetism with very low T_C [Jung (2002)], or no ferromagnetism at all [Tiwari (2002)]. Straightforward electron paramagnetic resonance (EPR) measurements revealed that ZnO nanocrystals substitutionally doped with Mn have a pure paramagnetic behaviour [Norberg (2004), Zhou (2003)]. Kittilstved *et al.* (2005) found experimental evidence of carrier mediated ferromagnetism through chemical manipulation. They found clear evidence of a correlation between *p*-type doping and high-T_C ferromagnetism in Mn doped ZnO and an inverse correlation for Co doped ZnO. By spin coating Mn doped ZnO high-quality colloidal nanocrystals into films and changing the charge polarity of the carriers, Kittilstved *et al.* (2006) were able to switch the ferromagnetism on (*p*-type) and off (*n*-type). Similarly, the manipulation of the polarity of the doping in Co doped spin coated films was obtained, but in this case the ferromagnetic behaviour was produced by the *n*-type doping. The work of Diaconu *et al.* (2005a, 2005b, 2005c) indicates that both paramagnetic and antiferromagnetic interactions of the Mn ions occur in Mn doped ZnO thin films. Later the same group reported the observation of Curie temperatures above 375 K in PLD grown thin films using targets sintered at temperatures above 500 ºC [Diaconu (2007)]. More recently, Xu *et al.* (2008b) achieved room temperature ferromagnetism in PLD grown ZnO films co-doped with Mn and Nd, once more suggesting that co-doping is an efficient method for introducing levels into the ZnO band gap to mediate the ferromagnetic interaction.

However, these results remain controversial since several reports claimed that the magnetic signature arises from clustering or segregated phases [Han (2003), Norton (2003a), Kolesnik and Dabrowski (2004), von Bardeleben (2008)]. Another example of the effect of secondary phases can be found in a work on Fe and Cu co-doped ZnO films [Shim (2005)], where the presence of Zn ferrite phases was found to be the explanation for preliminary results pointing to a robust ferromagnetic diluted phase [Han (2002)]. Other authors have identified precipitates of Fe_3O_4 [Shinagawa (2006)], Ni [Zhou (2006a)], $ZnFe_2O_4$ [Zhou (2008a)] or Mn, Fe and Co [Blasco (2006)] as the origin of the detected room temperature ferromagnetism in ZnO based materials. This points to the need for further investigations using a variety of methods to establish the lattice position, charge state, and oxidation state of the TM in the host lattice, in order to clarify magnetic properties of these materials that are very sensitive to the preparation method.

An optimistic approach to phase separation is given by Dietl (2007). The author points out the relevance of two kinds of nanoscale spacial phase separations. The first is spinodal alloy decomposition (chemical phase separation) into regions incorporating either very large or very small concentration of the magnetic element. For instance, if the concentration of one of the constituents is small, it may appear in a form of coherent nanocrystals embedded by the majority component. The second is disorder-driven electronic phase separation into ferromagnetic bubbles containing a large carrier density, and immersed in a depleted paramagnetic environment. Mainly, the author argues that weakly localized or delocalized carriers are necessary to mediate the ferromagnetic interactions between the randomly distributed diluted magnetic spins. Moreover, the author suggests that, since the distribution of magnetic ions can be controlled by growth conditions, co-doping, and post-growth processing, it is possible to prepare a material which is either a uniform magnetic semiconductor or a hybrid semiconductor/ferromagnet composite system.

At this point, it is essential to make a distinction between true ferromagnetic semiconductors and those which simply show magnetic hysteresis. In a true DMS, the magnetic dopant spins preserve a remnant alignment under the influence of spin polarized free carriers, which may be introduced either by the magnetic dopant or by a secondary electronic dopant. In the case of $Zn_{1-x}Co_{1-x}O$, magneto-optical effects measured by MCD indicate that this is a true DMS with polarized carrier population [Ando (2001a), Heo (2004a)]. On the other hand, magnetic hysteresis can have other physical origins, such as magnetic secondary phase

formation, or intrinsic defects [Xu (2008c), Zhou (2008b), Coey and Chambers (2008)]. Additionally, nonmagnetic semiconductors with embedded secondary phase ferromagnetic particles may exhibit an anomalous Hall effect, indicating an internal magnetic force on free carriers [Denardin (2003), Shinde (2004)]. Yet, the possible spin polarization in the majority carrier band so far has not been proved controllable in a way that is useful for spin-based devices.

Despite such pullbacks, Pan *et al.* (2007) reported surprisingly strong room temperature ferromagnetism in C-doped ZnO films grown by PLD. Along with the first-principles calculations, experimental evidence was given that carbon ions substitute for oxygen and their *p*-orbits contribute to the local moments. This result was checked and confirmed by Zhou *et al.* (2008c) by introducing carbon into ZnO films by ion implantation.

For both theoretical and experimental investigations to arrive at valid structure–magnetic function relationships, well-characterized magnetically doped semiconductors of high structural quality must be generated and carefully studied. Doped TM oxides are extremely complex, principally when the desired doping levels approach the limits of solid solubility. The structural complications that can result in these materials require detailed materials characterization prior to drawing conclusions about the mechanism of magnetism. Magnetic contamination is very easy to occur, for example by simply using common stainless steel tweezers, and results in misleading magnetic signals [Abraham (2005), Salzer (2007)]. Additionally, there is the possibility of detecting pitfalls in search of magnetic order. For example, Salzer *et al.* (2007) found ferromagnetic behaviour of single crystalline sapphire substrates, which is partially removed after surface cleaning. Detailed analysis of artefacts and pitfalls, such as contamination of cleaving edges by Ney *et al.* (2008) demonstrate that hysteresis measurements are not a sufficient criterion to prove the existence of ferromagnetism if the size of the signal is small (below 4×10^{-7} emu). As will be shown is this work, EPR is a valuable technique that can give additional insight into the magnetic interactions in these materials, given its extreme sensitivity to the microscopic environment of the doping elements. The combination of such a sensitive magnetic technique with structural characterization results in feasible conclusions about the magnetic features of the materials. Additionally, high standards of cleanliness and purity which have been used in the semiconductor industry should be applied to DMS research.

3 THEORETICAL FRAMEWORK

3.1 ELECTRON PARAMAGNETIC RESONANCE

The phenomenon of electron paramagnetic resonance (EPR) was first found by Zavoiskii (1944) when he observed induced quantum transitions between Zeeman sublevels in his studies of paramagnetic relaxation and resonance spectroscopy in the radiofrequency band (10-100 MHz). The magnetic resonance phenomenon is based on magnetic dipolar moment transitions between Zeeman energy levels, in the presence of a static magnetic field, and it consists of the absorbance of the electromagnetic radiation related to the occurring transitions. Due to the unique information that the magnetic resonance spectra provide about the interactions of the magnetic dipolar moment (*i.e.* the electron in EPR or the nucleus in nuclear magnetic resonance (NMR)) with its surrounding, this experimental technique has become essential in several areas of natural sciences, such as Physics, Chemistry, Geology, Biology and Medicine.

As most of spectroscopic techniques, EPR measures the interaction between electromagnetic radiation and matter. Nevertheless, the majority of these techniques use the interaction with the electric-field component of the radiation. For absorption to occur, the energy of a quantum of radiation must be equal to the separation between certain energy levels, and the oscillating electric-field component must be able to interact with an oscillating electric dipole moment. Similarly, a permanent magnetic moment may interact with the magnetic component of the electromagnetic radiation, forming the basis for magnetic resonance spectroscopy. Generally, in magnetic resonance experiments, an external magnetic field is applied in order to align the magnetic moments and split the energy levels (Zeeman effect). Each electron has an intrinsic magnetic-dipole moment that arises from its spin, but in most systems electrons occur in pairs, and the net magnetic moment is zero. Hence, EPR can be applied to any system containing unpaired electrons or magnetic nuclei.

EPR is extremely sensitive to the microscopic environment of the centres, being a very powerful technique for studying the electronic structure of defects in semiconductors, as revealed by the fine structure (FS) of the absorption. EPR gives insight in the total angular momentum, and the local symmetry of point defects. Moreover, with this technique one can probe the chemical nature of defects provided by nuclear hyperfine (HF) interactions, revealing both the nuclear spin and the relative abundance of the involved isotopes. The anisotropy of

such interactions provides further information on the structure and symmetry of the centres. Given enough data and guidance from theory, one may construct an energy-level diagram from a spectrum. Comparison between an energy-level diagram and an observed spectrum shows that, of all possible transitions between the various levels, only a relatively few "allowed" transitions are observed. Hence, one has to take into account the selection rules in order to analyze the transitions intensities.

3.1.1 Hamiltonian operators

The basis of the interpretation of all EPR spectra in the solid state is the appropriate assignment of the spin transitions to the energy levels of the paramagnetic centres. These energy levels can be determined from the solutions of the eigenvalue problem:

$$\mathscr{H}\psi = E\psi, \tag{3.1}$$

where $\mathscr{H}$ is the Hamiltonian operator, which characterizes the interaction of the paramagnetic centre with itself, with the host substance, with the applied magnetic field and eventually with additional external interference. Since the exact solution of a many particle problem is not achievable in practice, one has to find the suitable approximation procedure in order to completely describe the system taking into account its experimental properties, but in a simple and clear way. The Hamiltonian operator of the full system may be approximated by a sum of individual operators $\mathscr{H}_i$. The perturbation theory may be applied taking into account the magnitude of the involved individual contributions.

Neglecting weak interactions, the Hamiltonian operator may be approximated by the following sum

$$\mathscr{H} = \mathscr{H}_F + \mathscr{H}_{CF} + \mathscr{H}_{LS} + \mathscr{H}_{SI} + \mathscr{H}_{IL} + \mathscr{H}_Q + \mathscr{H}_Z + \mathscr{H}_{SS}, \tag{3.2}$$

where:

i. The Hamiltonian for the free ion is

$$\mathscr{H}_F = \frac{\hbar}{2m}\sum_i \Delta_i - \sum_i \frac{Ze^2}{\mathbf{r}_i} + \frac{1}{2}\sum_i\sum_j \frac{e^2}{\mathbf{r}_{ij}}, \tag{3.3}$$

here Z is the atomic number, e is the electron charge, m is the electron mass, and $\mathbf{r}_{ij}$ is the radius vector of the i–th electron with respect to the j–th nucleus $\mathbf{r}_{ij} = \mathbf{r}_i - \mathbf{r}_j$. $\mathscr{H}_F$ causes energy splittings of the order of 10^4-10^5 cm^{-1}.

ii. The Hamiltonian of the crystal field $\mathscr{H}_{CF}$ considers the influence of the electric fields created by the neighbouring ions or molecules ("ligands"). The splitting values can be calculated by means of group theory. They depend on the orbital quantum number L and on the geometry of the crystal field (CF) and span the range from 10^5-10^1 cm^{-1}.

iii. $\mathscr{H}_{LS}$ is the Hamiltonian of the spin–orbit interaction, which in the case of the Russell–Saunders coupling is given by

$$\mathscr{H}_{LS} = \xi(r)\mathbf{L}\cdot\mathbf{S}, \tag{3.4}$$

where $\xi(r) = \frac{e}{2m^2c^2}\left(\frac{1}{2}\frac{\partial V}{\partial r}\right)$, $V(r)$ is the Hartree-Fock central field potential, **L** and **S** are the total orbital angular momentum and the electron spin operators, respectively. For the iron group ions, the splittings due to $\mathscr{H}_{LS}$ are of the order of 10^2 cm^{-1}.

iv. The Hamiltonian of the HF structure $\mathscr{H}_{SI}$ describes the interaction between the electron spins and the nuclear magnetic moment:

$$\begin{aligned}\mathscr{H}_{SI} = -g_e\beta g_N\beta_N\sum_k\left(\frac{\mathbf{S}_k\cdot\mathbf{I}}{\mathbf{r}_k^3} - \frac{3(\mathbf{r}_k\cdot\mathbf{S}_k)(\mathbf{r}_k\cdot\mathbf{I})}{\mathbf{r}_k^5}\right),\\ + \frac{8\pi}{3}g_e\beta g_N\beta_N\sum_k(\mathbf{S}_k\cdot\mathbf{I})\delta(\mathbf{r}_k)\end{aligned} \tag{3.5}$$

where **I** is the nuclear angular momentum and includes the spins as well as the nucleons orbital momenta. For the sake of brevity, one calls **I** nuclear spin. g and g_N are the electron and the nuclear g-factors, respectively, and β and β_N are the Bohr magneton and the nuclear magneton, respectively. The first term reflects the usual dipole–dipole interaction between the spin magnetic moments of the nucleus and of the electrons. The second term reflects the Fermi contact interaction and can be obtained from the first one by making $r \to 0$. The first term accounts for the HF interaction of the *p*–, *d*– and *f*–shell electrons with the nucleus. The *s*–electrons have a finite density at the nucleus. For them, the HF interaction is given by the second term. For the iron group, the HF splitting does not exceed 10^{-1} – 10^{-3} cm^{-1}.

v. The interaction of the nuclear spin with the orbital momentum of the electron is described by the Hamiltonian

$$\mathscr{H}_{IL} = g\beta g_N\beta_N\sum_k\left(\frac{\mathbf{l}_k\cdot\mathbf{I}}{r_k^5}\right), \tag{3.6}$$

with $\mathbf{l}_k$ being the operator of the individual orbital angular momentum. This interaction indirectly couples the nuclear and the electron spins, namely through the spin-orbit interaction.

vi. The Hamiltonian of the nuclear quadrupole interaction $\mathscr{H}_Q$ is given by

$$\mathscr{H}_Q = \frac{e^2 Q}{2I(I+1)} \sum_k \left(\frac{I(I+1)}{r_k^3} - \frac{3(\mathbf{r}_k \cdot \mathbf{I})}{r_k^5} \right), \tag{3.7}$$

and considers the electrostatic interaction of the CF with the quadrupole moment of the nucleus Q. The quadrupole interaction causes a level shift but no splitting. The interaction occurs only for $I \geq 1$ and the splitting is of the order of 10^{-3} cm^{-1} .

vii. The energy of the interaction of the external magnetic field **B** with the spin magnetic dipole moments of the electrons and of the nucleus is $g\beta\left(\mathbf{B} \cdot \sum_k (\mathbf{S}_k) \right) - g_N \beta_N (\mathbf{B} \cdot \mathbf{I})$ $= (g\beta \mathbf{S} - g_N \beta_N \mathbf{I}) \cdot \mathbf{B}$. In the case of a constant magnetic field the Zeeman Hamiltonian is given by

$$\mathscr{H}_Z = \beta(\mathbf{L} + g\mathbf{S}) \cdot \mathbf{B} - \beta_N g_N \mathbf{I} \cdot \mathbf{B}. \tag{3.8}$$

For the X–band ($\nu \approx 9$ GHz) and $g \approx 2$, $B \approx 3300$ G we obtain the quantum mechanical mean value of the Zeeman Hamiltonian $\langle \mathscr{H}_Z \rangle \approx 0.3\,\text{cm}^{-1}$. Since the ratio between the Bohr magneton and the nuclear magneton β/β_n is equal to ratio between the proton and electron masses m_p/m, the nuclear Zeeman term is small when compared to the electron one. Therefore, the nuclear Zeeman term may be neglected when the magnetic field at the nucleus due to the electron spin is significantly stronger than the applied magnetic field.

viii. The Hamiltonian $\mathscr{H}_{SS}$ describes the energy of the magnetic dipole–dipole interaction of the paramagnetic particles among each other (that is, the spin–spin interaction);

$$\mathscr{H}_{SS} = g^2 \beta^2 \sum_{i>k} \left(\frac{\mathbf{S}_i \cdot \mathbf{S}_k}{r_{ik}^3} - \frac{3(\mathbf{r}_{ik} \cdot \mathbf{S}_k)(\mathbf{r}_{ik} \cdot \mathbf{S}_i)}{r_{ik}^5} \right). \tag{3.9}$$

The fact that $\mathscr{H}_{SS} \propto \frac{1}{r_{ik}^3}$, leads to a strong dependence of the splitting on the concentration of the paramagnetic particles. In the paramagnetic salts (*e.g.* $MnCl_2$, $CuSO_4$), the splittings are of the order of 1 cm^{-1}. Because the spin–spin interaction makes the whole

picture very complicated, one often uses the method of "magnetic diluting". That means, the paramagnetic ions are diluted in a diamagnetic matrix (host crystal). If the concentration of the paramagnetic ions is ≤ 1 at. %, the spin–spin interaction can be neglected.

3.1.2 Spin Hamiltonian

The electronic states in a crystal are described by the solution of the Schrödinger equation which comprises the Hamiltonian that expresses the sum of all interactions concerning the involved nuclei and electrons [Kittel (1996)]. The solution of this equation is impossible to achieve in solids. Nevertheless, using some well known approximations, namely considering that the electron mass is much smaller than nuclear mass, the Born-Oppenheimer approximation, the one-electron approximation and the periodic properties of a perfect crystal, it can be shown that the wave functions of the electrons in the static lattice are of the Bloch type [Kittel (1996)]. Hence, the electronic structure of a perfect crystal consists of several energy bands, which may be separated by forbidden ones. In insulators and semiconductors, the valence band (highest occupied energy band) is completely filled with electrons. The transition between insulating and semiconductor materials is continuous and dependent on the value of the band gap energy E_g between the valence and conduction band.

The defects, such as impurities or imperfections, in the material may be described as a perturbation to the perfect crystal, introduced by a localized potential. This effect is taken into account by introducing a perturbation to the Hamiltonian of the perfect crystal. Depending on the nature of the defect, this perturbation may induce mid-gap levels (deep defects) due to strong localized potentials or levels near the band edges (shallow defects) owing to weak delocalized potentials.

The ground state of a paramagnetic ion in a crystal is usually composed of a group of electronic levels whose separation is of the order a few reciprocal centimetres, which is very small compared to the energy separation with respect to other electronic states. In this sense, to interpret a paramagnetic resonance spectrum one can use the approach of the spin Hamiltonian (SH) which only considers the interactions at the ground state level of the ion. Usually, a paramagnetic resonance spectrum is rather complex, composed of lines due to different electronic transitions. The magnetic field at which these transitions take place changes with the frequency of the applied radiation, and, in the case of anisotropic interactions, it will also be

dependent on the relative orientation of the applied magnetic field and the crystal axes. The set of data obtained from measurements with different frequencies and orientations, under correct interpretation, comprises meaningful information about the structure and chemical nature of the paramagnetic centre. This interpretation is carried out in the light of the SH whose form can frequently be guessed from some considerations of CF symmetry. Such a SH contains relatively few terms and the magnitude of the coefficients of these terms completely describes the experimental data. The behaviour of the involved group of levels can be represented by defining an "effective spin" $\widetilde{S}$, such that the number of levels in this group is given by $2\widetilde{S}+1$, as in an ordinary spin multiplet. It is noteworthy that in some cases the effective spin and the true spin of the ion coincide, *e. g.* if the orbital momentum is zero or it is "frozen in" by the CF. It is also required that the matrix elements between the various states determined by the full Hamiltonian are proportional to those of the SH.

All the contributions of an orbital singlet ground state and of the excited states are combined into constants and the terms in the SH depend on the magnetic field **B**, the electronic spin **S** and the nuclear spin **I**. Thus, in general the SH can be written as:

$$\mathscr{H} = \sum_{i,j} \left(\beta g_{ij} S_i B_j + D_{ij} S_i S_j + A_{ij} S_i I_j + \cdots \right), \tag{3.10}$$

where the first term corresponds to the electron Zeeman interaction, the second term accounts for the electron quadrupole interaction (FS and zero field splitting (ZFS)), and the third term represents the HF interaction due to the presence of nuclear magnetic dipole and electric quadrupole moments in the central or ligand ions. Depending on the special problem one must add other terms, such as the nuclear Zeeman interaction, the nuclear quadrupole interaction and the interaction between the electron spin and higher order octopole momentum. The parameters of the SH are determined by fitting of the eigenvalues of this operator to the observed spectrum. Subsequently, the computation of the parameters can take place for the complete analysis of the spectrum. In this sense, Abragam and Pryce (1951) developed the concept of the SH for the analysis of EPR spectra for the so-called mean crystal field (*i.e.* in the case of spin-orbit interaction < crystal field < Coulomb interaction between the electrons of the paramagnetic centre).

For determining the centre symmetry and computing the parameters of the SH, in most cases the assumption of a rigid crystal lattice in first approximation is sufficient. Nevertheless,

for the explanation of the temperature dependence of the parameters, the relaxation behaviour of the centres and the coupling to the crystal lattice vibration has to be considered. However, this is not valid for EPR spectra of manifold states with non or only partially quenched orbital degeneracy. In these cases (*e.g.* for orbital doublet and triplet states), using the effective Hamiltonian operators and neglecting the interaction of the electrons of the paramagnetic centres with the lattice vibrations (electron-phonon coupling) can lead to wrong results. Hence, in such cases the Hamiltonian operator (3.10) must include not only the electron and nuclear spin operators, but also contributions of the orbital momentum of the electrons of the paramagnetic centre.

Generally, the SH does not have an achievable analytical solution. Therefore, in practice, the eigenvalues of the system are determined numerically through approximation methods.

3.1.3 Crystal Symmetry

The theory of molecular orbitals describes the modifications of the binding in the first coordination sphere, which is proved to be the most significant in order to interpret the paramagnetic centre properties. The association degree between the electron and the central ion varies continuously between zero and infinity (usually normalized to 1). In the case that the electrons of an ion are completely bonded to the ion, while the set of ligand atoms are at an equilibrium distance in the first coordination sphere, we are in the presence of the CF model. In this model, the electrons of the ligands will remain, in the same way, completely attached to those atoms. Conversely, one has a completely covalent bond described by the ligand field model, in the case of the overlapping of the wave functions of the electrons of the paramagnetic centre and of the ligands, so that any of the electrons of either entities may be found with equal probability associated to any atom of the system, whether the central ion or the ligands. Both described cases represent extreme types of bonding which may be found in coordination complexes, being special cases of the molecular orbital treatment. Nevertheless, by means of that treatment, all intermediate degrees of electron sharing may also be described. Thus, it is usual to reserve the designation of *crystal field theory* for the extreme in which there is no overlapping of the wave functions of the electrons of the central ion and of the ligands, and to employ the term *ligand field theory* to all cases in which there is a non-zero degree of mixing.

In EPR we are particularly interested in studying paramagnetic centres. As a paramagnetic centre we understand an impurity, defect, dangling bond or charge carrier possessing a non-zero

angular momentum, normally including its close environment. The simplest way to treat the ligand field is to consider it as pure electrostatic interaction. The ligands may be regarded as localized ions in certain lattice sites that create a crystalline potential U, which reflects the local symmetry of the ionic environment. This will result in an energy splitting of the magnetic electrons, due to the presence of this crystal electric field (Stark effect).

A free ion has spherical symmetry, and if only its respective orbital momentum is considered, only one, three, five or seven linearly independent eigenfunctions belong to an *S*-, *P*-, *D*- or *F*-state, respectively. In this sense, *e.g.* a *D*-state is a fivefold orbitally degenerate state. The analysis through group theory shows that a crystal field with cubic symmetry (O_h or T_d) does not split a *S*- or a *P*-state, but the degeneracy of the other terms is partially lifted. The fivefold degenerate *D*-state is split by cubic symmetry in two states, one triplet (T_2) and one doublet (E) states, and a *F*-state is split into two triplet states (T_1 and T_2) and one orbital singlet state (A_2), as shown in Fig. 3.1. Furthermore, the corresponding calculations demonstrate that tetrahedral symmetry always inverts the sequence of the energy levels due to splitting in octahedral symmetry [Abragam and Bleany (1986)]. For example, the energy level sequence of an F-state of a free ion that is put into an octahedral crystal field is A_{2g}, T_{2g}, T_{1g},[1] so if it was put into a tetrahedral ligand field the energy level sequence would be T_1, T_2, A_2. CFs of lower symmetries cause further splitting of the states. The lifting of the degeneracy by non-cubic ligand fields frequently causes that transition metal (TM) ions have zero orbital angular momentum [van Vleck (1932)], which allows that these energy levels of the ion be essentially characterized by the spin (the effective spin). Therefore, the SH may be written as a function of the nuclear and electron spin operators, and the orbital angular momenta are included in the parameters of the different terms.

[1] Contrary to tetrahedral complexes, in octahedral ones there is an inversion symmetry centre and the terms are characterized by an additional index *g* (meaning pair), so, *e.g.* T_{1g} corresponds to T_1.

d^1	d^2	d^3	d^4	d^5	d^6	d^7	d^8	d^9
^2D	^3F	^4F	^5D	^6S	^5D	^4F	^3F	^2D
$^2T_2$	$^3T_1$	$^4A_2$	^5E	$^6A_1$	$^4T_1$	$^4T_1$	$^3A_2$	^2E
Ti^{3+}	V^{3+}	Cr^{3+}	Mn^{3+}	Fe^{3+}	Co^{3+}			
		V^{2+}	Cr^{2+}	Mn^{2+}	Fe^{2+}	Co^{2+}	Ni^{2+}	Cu^{2+}

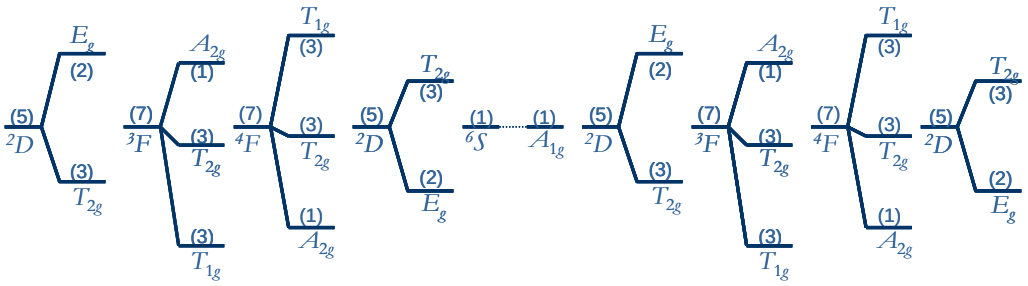

Fig. 3.1. Splitting of the ground state of the ions with valence configurations of d^1 to d^9 (Ti^{3+} to Cu^{2+}) in octahedral symmetry. In tetrahedral symmetry, the terms are inverted, *e.g.* for d^7 the ground state will be an orbital singlet (A_2).

3.1.4 Selection rules

The type of the interaction between the electromagnetic radiation and the spin system establishes the transition probability between the involved states, $|W_i\rangle$ and $|W_f\rangle$. Under resonance conditions, this transition probability is proportional to $\left|\langle W_i|\mathscr{H}_1|W_f\rangle\right|^2$, where $\mathscr{H}_1$ is the perturbation to the spin system by the magnetic component of the microwave radiation $\mathbf{B}_1$:

$$\mathscr{H}_1 = -\mathbf{B}_1 \cdot \boldsymbol{\mu}, \tag{3.11}$$

$\boldsymbol{\mu}$ is the total magnetic dipole operator of the spin system. Since generally we have $\mathbf{B}_1 \perp \mathbf{B}$, if we choose $\mathbf{B} \| Z$ and $\mathbf{B}_1 \| X$, the Hamiltonian operator will be:

$$\mathscr{H}_1 = g\beta B_1 S_X - g_n \beta_n B_1 I_X. \tag{3.12}$$

For the eigenfunctions of the SH $|M_S, m_I\rangle$, the matrix elements of $\mathscr{H}_1$ are

$$\begin{aligned}\langle M_S, m_I|\mathscr{H}_1|M_S', m_I'\rangle = g\beta B_1 \langle M_S|S_X|M_S'\rangle\langle m_I|m_I'\rangle \\ - g_N\beta_N\langle M_S|M_S'\rangle\langle m_I|I_X|m_I'\rangle\end{aligned}, \tag{3.13}$$

where M_S and m_I are the electron and nuclear spin quantum numbers, respectively. In the case of EPR transitions, these matrix elements are nonzero when $M_S = M_S \pm 1$ and $m_I' = m_I$ [Weil *et al.*

(1994)]. Therefore, under high-field conditions, the selection rules for detectable transitions in EPR are

$$\Delta M_S = \pm 1 \quad \text{and} \quad \Delta m_I = 0\,. \tag{3.14}$$

The transitions that obey these rules are commonly called allowed transitions and have a transition probability proportional to $(g\beta B_1)^2$. Other transitions are possible at low fields, where the eigenfunctions become linear combinations of the $|M_S, m_I\rangle$ states and the quantum numbers M_S and m_I are no longer appropriate. These transitions are known as "forbidden" transitions.

3.1.5 The anisotropy of the g-factor: doublet state

For a system with an odd number of electrons, the eigenvalues are at least doubly degenerate (Kramers degeneration) without an applied magnetic field. Hence, a Kramers doublet cannot be split by any crystal field. Neglecting the nuclear interactions, the interactions between the effective spin and the applied magnetic field can be described by the following SH operator

$$\begin{aligned}\mathscr{H} = \beta \mathbf{B}\cdot\mathbf{g}\cdot\mathbf{S} = \beta\{&g_{XX}B_X S_X + g_{YY}B_Y S_Y + g_{ZZ}B_{ZZ}S_{ZZ} + g_{XY}B_X S_Y + g_{YX}B_Y S_X + \\ &g_{XZ}B_X S_Z + g_{ZX}B_Z S_X + g_{YZ}B_Y S_Z + g_{ZY}B_Z S_Y\}\end{aligned}. \tag{3.15}$$

In the majority of the cases the relation $g_{ij} = g_{ji}$ is valid, and the non-diagonal elements can be eliminated by choosing the appropriate *X*, *Y*, and Z axes (designated as principal axes system). Hence, Eq. (3.15) is reduced to:

$$\mathscr{H} = \beta\{g_{XX}B_X S_X + g_{YY}B_Y S_Y + g_{ZZ}B_{ZZ}S_{ZZ}\}\,. \tag{3.16}$$

In the case of an arbitrary choice of the magnetic field direction, given the polar angles θ and φ relative to the principal axes of the *g*-tensor, Eq. (3.15) is given by[2]:

$$\mathscr{H} = \beta B\{g_X \sin\theta\sin\varphi S_X + g_Y \sin\theta\cos\varphi S_Y + g_Z \cos\theta S_Z\}\,. \tag{3.17}$$

Introducing the basis functions $|M_S\rangle = |\pm 1/2\rangle$, one gets the following eigenvalue problem

[2]For simplification, usually in the main axes system one sets: $g_{XX} = g_X, g_{YY} = g_Y, g_{ZZ} = g_Z$.

$$\begin{array}{c} \left|-\tfrac{1}{2}\right\rangle \qquad\qquad\qquad\qquad \left|+\tfrac{1}{2}\right\rangle \\ \left\langle -\tfrac{1}{2}\right| \\ \left\langle +\tfrac{1}{2}\right| \end{array} \begin{vmatrix} -\frac{1}{2} g_Z B\cos\theta - E & \frac{1}{2}(g_X B\sin\theta\sin\varphi + i g_Y B\sin\theta\cos\varphi) \\ \frac{1}{2}(g_X B\sin\theta\sin\varphi - i g_Y B\sin\theta\cos\varphi) & +\frac{1}{2} g_Z B\cos\theta - E \end{vmatrix} = 0 \,. \qquad (3.18)$$

Thus, the resulting eigenvalues are

$$E_{1,2} = \pm\frac{1}{2}\beta B\sqrt{g_Z^2\cos^2\theta + \sin^2\theta(g_X^2\sin^2\varphi + g_Y^2\cos^2\varphi)}\,, \qquad (3.19)$$

and the transition energy is given by

$$h\nu = E_2 - E_1 = g\beta B\,, \qquad (3.20)$$

were h is the Planck constant, and

$$g = \sqrt{g_Z^2\cos^2\theta + \sin^2\theta(g_X^2\sin^2\varphi + g_Y^2\cos^2\varphi)}\,. \qquad (3.21)$$

The Zeeman splitting and thus the energy states involved in the electron spin transition M_S = -1/2↔+1/2 become angular dependent, *i.e.* dependent on the direction of the applied magnetic field B relatively to the principle axes (Fig. 3.2). For axial symmetry, *i.e.* for tetragonal or trigonal symmetry, one selects the tetragonal and/or trigonal axis of the crystal field perturbation as the Z-axis[3] and Eq. (3.21) is simplified with $g_Z = g_\parallel$ and $g_X = g_Y = g_\perp$

$$g = \sqrt{g_\parallel^2\cos^2\theta + g_\perp^2\sin^2\theta}\,. \qquad (3.22)$$

In the case of a cubic crystal field, the magnetic properties must show likewise cubic or higher symmetry.[4] In this case, the g-value is isotropic, $g = g_X = g_Y = g_Z$, and the choice of the axes is arbitrary. Thus, a new coordinate system (X', Y', Z') becomes appropriate; B is selected to be parallel to Z', and the SH operator (3.17) is reduced to $\mathcal{H} = g\beta B S_{Z'}$ with eigenvalues $E_{1,2} = \pm\frac{1}{2} g\beta B$.

---

[3] The X- and Y-axes are equivalent in the plane perpendicular to the Z-axis, because of the axial symmetry. This is used frequently for simplification of the computation for axial symmetry. Thus, it is generally accepted that the direction of B is determined by an angle θ in the ZX-plane. Thus the spin Hamilton operator (3.16) is simplified to $\mathcal{H} = \beta B\{g_Z S_Z\cos\theta + g_\perp\sin\theta\}$.

[4] Strictly, the following is valid: generally spherical and cubic symmetry cannot be differentiated by a bilinear term as $g_{ij}B_iS_j$. Hence, in the SH operator, the group theory allowed Zeeman terms ~S^3B must be considered. However, these are different from zero only for $S \geq 3/2$. If this contribution is not to be neglected relatively to the normal Zeeman interaction, then a cubic angular dependence is observed, instead of a line arising at the same magnetic field value for arbitrary magnetic field directions (frequently designated as "standing line"). If one doesn't consider locally the difference between quantum-mechanical spin operators and vectors/tensors, then the situation is similar to crystal physics: spherical and cubic symmetry can only be differentiated if the properties are described at least by a 4th degree tensor (*e.g.* elasticity coefficients), since only these can differentiate a cubic (tetrahedral, octahedral) symmetry axis from spherical symmetry.

For the experimental determination of the parameters $g_{\parallel}$ and $g_{\perp}$, which describe the entire angular dependence in the case of axial symmetry, in agreement with the relation (3.22), one measures the resonance field for $B \parallel Z$ and $B \perp Z$. Similarly, in the case of orthorhombic symmetry, g_X, g_Y and g_Z, the resonance field values are determined for $B \parallel X$, $B \parallel Y$ and $B \parallel Z$.

If the paramagnetic centre is introduced in a crystal with higher symmetry than the point symmetry of the centre, several different but equivalent orientations of the centre exist. For example, for a centre with trigonal symmetry in a cubic crystal field, *e.g.* silicon with T_d symmetry, there are four equivalent centre orientations, thus for a general direction of the magnetic field all have different angles θ_i, and by rotating the magnetic field in a certain crystal plane, in agreement with Eq. (3.21), each one will exhibit a different angular dependence. Therefore, a clear determination of the centre symmetry (Laue symmetry) is possible.

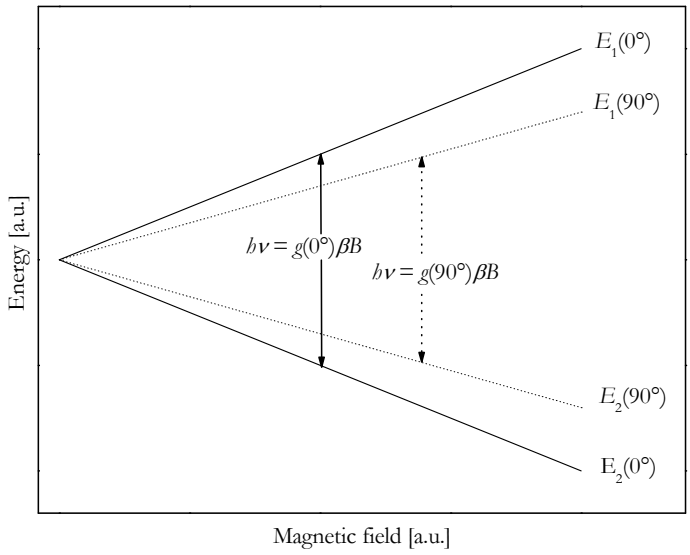

Fig. 3.2. Zeeman splitting and energy levels of the electron spin transitions for $S = 1/2$ and $B \parallel Z$ ($\theta = 0°$) und $B \perp Z$ ($\theta = 90°$), in the case of a centre with axial symmetry.

3.1.6 Zero field splitting: electronic quadrupole fine structure (S = 1, 3/2)

In a CF with cubic symmetry, without any applied magnetic field, the $2S+1$ energy levels are degenerate. By applying a magnetic field, the Zeeman effect splits the levels and the result is described by the Hamiltonian

$$\mathcal{H} = \beta \mathbf{B} \cdot \mathbf{g} \cdot \mathbf{S}. \tag{3.23}$$

Thereby a set of energy levels is produced with the same energy splittings. The allowed transitions occur between successive energy levels ($\Delta M_S = \pm 1$) separated by an energy of $g\beta B$, so that there are $2S$ possible transitions with the following resonant condition

$$h\nu = g\beta B. \tag{3.24}$$

This is illustrated in Fig. 3.3 for $S = 1$.

When there is a deviation from cubic symmetry, one must introduce a second degree FS term in the spin operator[5]

$$\mathbf{S} \cdot \mathbf{D} \cdot \mathbf{S} = \sum_{i,j} D_{ij} S_i S_j \,. \tag{3.25}$$

In the case of orthorhombic symmetry, the splitting due to the CF distortion is described by the term[6]

$$D\{S_Z^2 - \frac{1}{3}S(S+1)\} + E\{S_X^2 - S_Y^2\}\,. \tag{3.26}$$

In the case of axial symmetry, $E = 0$ and the SH operator including the Zeeman interaction is given by[7]:

$$\mathcal{H} = \beta B\{g_Z S_Z \cos\theta + g_\perp S_X \sin\theta\} + D\{S_Z^2 - \frac{1}{3}S(S+1)\}\,. \tag{3.27}$$

---

[5] **D** is a symmetric traceless tensor: $D_{ij} = D_{ji}$, $D_{XX} + D_{YY} + D_{ZZ} = 0$. By projecting the **D** tensor into its principal axis system (X', Y', Z') one gets: $\begin{pmatrix} D_{X'X'} & 0 & 0 \\ 0 & D_{Y'Y'} & 0 \\ 0 & 0 & D_{Z'Z'} \end{pmatrix}$, where the common definition is: $D_{X'X'} = -1/3D + E$, $D_{Y'Y'} = +1/3D + E$; $D_{Z'Z'} = 2/3D$. Wherefrom follows that $D = 3/2 D_{Z'Z'}$, $E = 1/2(D_{X'X'} - D_{Y'Y'})$. For axial symmetry, the orthorhombic contribution is zero, thus $E = 0$.

[6] Here one must always consider that in this way of writing, the orthorhombic distortion is expressed in the principal axis system (X, Y, Z).

[7] Considering footnote 4.

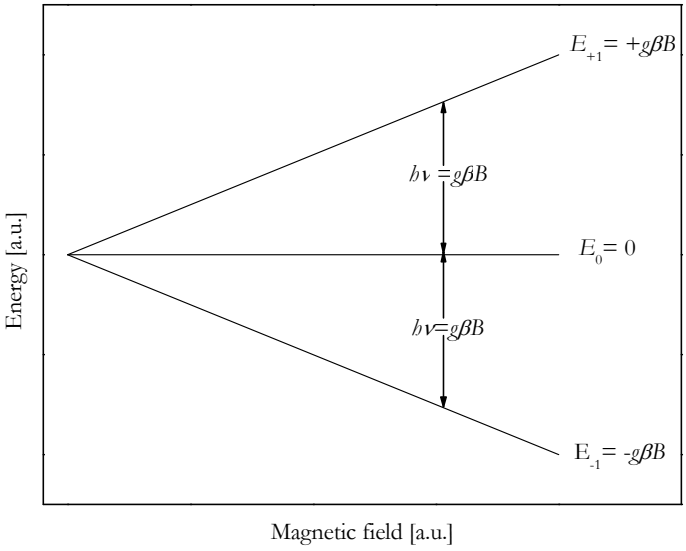

Fig. 3.3. Zeeman splitting for a triplet state $S = 1$ in a crystal field with cubic symmetry. Both the allowed resonant transitions occur when the condition $h\nu = g\beta B$ is fulfilled.

And for a triplet state with $S = 1$, with the basis functions $|M_S\rangle$ ($\Delta M_S = \pm 1$), the corresponding eigenvalues are given by the following equation[8]

$$\begin{array}{c} \\ \langle +1| \\ \langle 0| \\ \langle -1| \end{array} \begin{vmatrix} |+1\rangle & |0\rangle & |-1\rangle \\ G_Z\cos\theta + 1/3D - E' & 1/\sqrt{2}G_\perp \sin\theta & 0 \\ 1/\sqrt{2}G_\perp \sin\theta & -2/3D - E' & 1/\sqrt{2}G_\perp \sin\theta \\ 0 & 1/\sqrt{2}G_\perp \sin\theta & -G_Z\cos\theta + 1/3D - E' \end{vmatrix} = 0\,, \tag{3.28}$$

where the abbreviations $G_Z = g_Z\beta B$ und $G_\perp = g_\perp\beta B$ are employed. The solutions are only analyzed for two different cases, namely $B \| Z$ and $B \perp Z$. For $B \| Z$, the non diagonal terms vanish because $\sin\theta = 0$, and therefore one gets the following eigenvalues:

$$E_{|+1\rangle} = \frac{1}{3}D + G_Z \qquad E_{|0\rangle} = -\frac{2}{3}D_Z \qquad E_{|-1\rangle} = \frac{1}{3}D - G_Z\,. \tag{3.29}$$

The energy level splittings are illustrated in Fig. 3.4, together with the allowed transitions ($\Delta M_S = \pm 1$), corresponding to $h\nu = |D \pm g_Z\beta B_Z|$ and, for a more complete picture, the forbidden

[8]To avoid confounding between the orthorhombic distortion E with the energy eigenvalues, the latter are designated as E'.

transitions ($\Delta M_S = \pm 2$) with $h\nu = 2g_Z\beta B_Z$ are also indicated. From Eq. (3.28), for $B \perp Z$ ($\sin\theta = 1$), one gets:

$$\left(\frac{1}{3}D - E'\right)^2\left(-\frac{2}{3}D - E'\right) - 2G_\perp^2\left(\frac{1}{3}D - E'\right) = 0\,. \tag{3.30}$$

From where the solution follows:

$$E'_1 = \frac{1}{3}D\,. \tag{3.31}$$

Dividing Eq. (3.30) by $1/3D\text{-}E'$, one gets the quadratic equation

$$E'^2 + \frac{1}{3}DE' - \frac{2}{9}D^2 - 2G_\perp^2 = 0\,. \tag{3.32}$$

with the solutions

$$E_{2,3} = -\frac{1}{6}D \pm \frac{1}{2}d\sqrt{1 + \left(\frac{2g_\perp\beta B}{D}\right)^2}\,. \tag{3.33}$$

From Eqs. (3.31) and (3.33), the resulting energy splitting as a function of the applied magnetic field is represented in Fig. 3.5. The eigenfunctions corresponding to the three eigenvalues are linear combinations of the three basis functions $|+1\rangle$, $|0\rangle$ and $|-1\rangle$. Thus, the transitions between all three energy levels are allowed, and with sufficiently high microwave frequency ν, the three transitions can be observed. In very strong magnetic fields ($g\beta B >> D$) the amplitudes of the eigenfunctions become weaker than the basis functions by a factor of the order of magnitude of $(D/g_\perp\beta B)^2$, in good approximation.

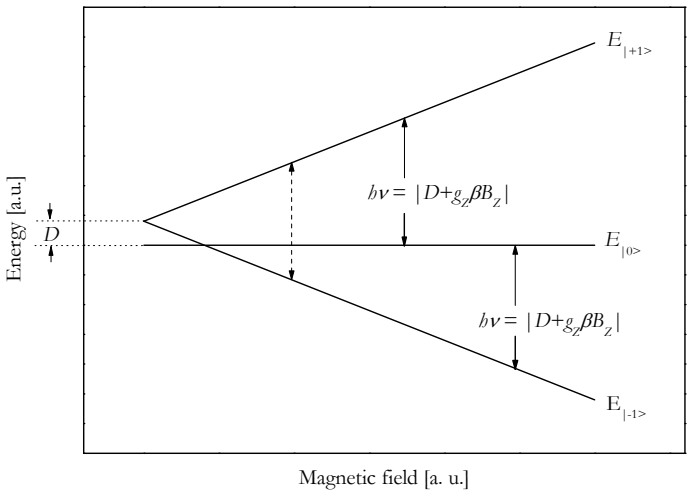

Fig. 3.4. Zeeman splitting and the allowed transitions ($\Delta M_S = \pm 1$) (—) as well as the forbidden transitions ($\Delta M_S = \pm 2$) (---) for the SH (3.27) with $S = 1$, and $B \parallel Z$. For exactly $B \parallel Z$, the transition probability of the forbidden transitions is zero.

Finally, we will address the spin quartet state ($S = 3/2$) in a CF with axial symmetry ($D \neq 0$, $E = 0$). Similarly to the case of the triplet state ($S = 1$), the SH is given by Eq. (3.27), but with the basis functions $\left|M_S\right\rangle$ (M_S = -3/2, ..., +3/2), and the energy determinant is as follows:

$$\begin{array}{c|cccc} & \left|+\frac{3}{2}\right\rangle & \left|+\frac{1}{2}\right\rangle & \left|-\frac{1}{2}\right\rangle & \left|-\frac{3}{2}\right\rangle \\ \left\langle+\frac{3}{2}\right| & \frac{3}{2}G_Z\cos\theta + D - E' & \frac{\sqrt{3}}{2}G_\perp\sin\theta & 0 & 0 \\ \left\langle+\frac{1}{2}\right| & \frac{\sqrt{3}}{2}G_\perp\sin\theta & \frac{1}{2}G_Z\cos\theta - D - E' & G_\perp\sin\theta & 0 \\ \left\langle-\frac{1}{2}\right| & 0 & G_\perp\sin\theta & -\frac{1}{2}G_Z\cos\theta - D - E' & \frac{\sqrt{3}}{2}G_\perp\sin\theta \\ \left\langle-\frac{3}{2}\right| & 0 & 0 & \frac{\sqrt{3}}{2}G_\perp\sin\theta & -\frac{3}{2}G_Z\cos\theta + D - E' \end{array} = 0 \qquad (3.34)$$

For $B \| Z$ ($\sin\theta = 0$), (3.34) is a diagonal determinant concerning the basis functions $\left|M_S\right\rangle$ and the four corresponding eigenvalues are immediately determined:

$$\begin{aligned} E_{\left|\pm\frac{3}{2}\right\rangle} &= \pm\frac{3}{2}g_Z\beta B + D, \\ E_{\left|\pm\frac{1}{2}\right\rangle} &= \pm\frac{1}{2}g_Z\beta B - D. \end{aligned} \qquad (3.35)$$

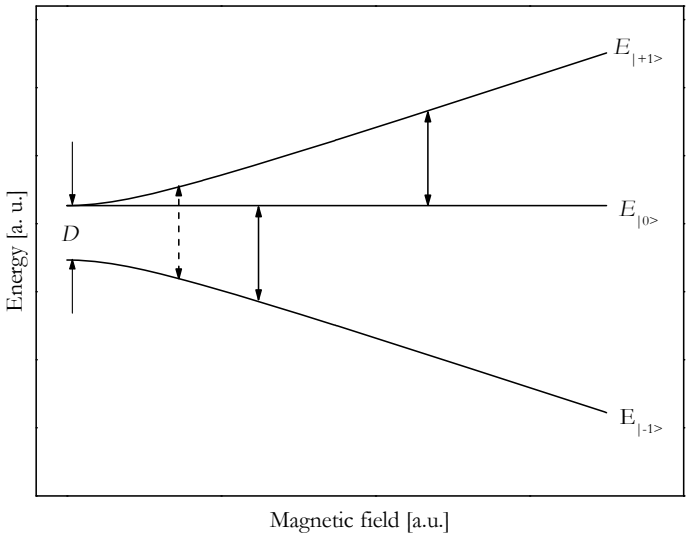

Fig. 3.5. Zeeman splitting and the allowed transitions ($\Delta M_S = \pm 1$) (—) as well as the forbidden transitions ($\Delta M_S = \pm 2$) (---) for the SH (3.27) with $S = 1$, and $B \perp Z$.

For a positive D,[9] the energy level diagram is shown in Fig. 3.6, Under the assumption that the ZFS is smaller than the microwave energy ($2D < h\nu$), $2S = 3$ allowed resonance lines are observed. The parameters $g_Z = g_\parallel$ and D can be determined from the line positions of these three transitions.

For $B \perp Z$ the energy determinant (3.34) is simplified due to $\cos\theta = 0$ and $\sin\theta = 1$:

$$\begin{vmatrix} +D-E' & \frac{\sqrt{3}}{2}G_\perp & 0 & 0 \\ \frac{\sqrt{3}}{2}G_\perp & -D-E' & G_\perp & 0 \\ 0 & G_\perp & -D-E' & \frac{\sqrt{3}}{2}G_\perp \\ 0 & 0 & \frac{\sqrt{3}}{2}G_\perp & +D-E' \end{vmatrix} = 0 \tag{3.36}$$

from where one finds the solutions:

$$\begin{aligned} E_1' &= E_{\left|+\frac{3}{2}\right\rangle} = +\frac{g_\perp\beta B}{2} + \sqrt{(g_\perp\beta B)^2 - g_\perp\beta BD + D^2}, \\ E_2' &= E_{\left|+\frac{1}{2}\right\rangle} = -\frac{g_\perp\beta B}{2} + \sqrt{(g_\perp\beta B)^2 + g_\perp\beta BD + D^2}, \\ E_3' &= E_{\left|-\frac{1}{2}\right\rangle} = +\frac{g_\perp\beta B}{2} - \sqrt{(g_\perp\beta B)^2 - g_\perp\beta BD + D^2}, \\ E_4' &= E_{\left|-\frac{3}{2}\right\rangle} = -\frac{g_\perp\beta B}{2} - \sqrt{(g_\perp\beta B)^2 + g_\perp\beta BD + D^2}. \end{aligned} \tag{3.37}$$

The corresponding eigenfunctions $\left|\hat{M}_S\right\rangle$ are linear combinations of the basis functions $\left|M_S\right\rangle$. The energy level splitting diagram is shown in Fig. 3.7. The degeneracy for $B = 0$ (doubly degenerate spin state with a ZFS equal to $2D$) is lifted by the magnetic field.

For $2D < h\nu$ all six possible transitions are observed, including the three 'allowed' transitions $\Delta M_S = \pm 1$, and due to the mixture of the wave functions, the two 'forbidden' transitions $\Delta M_S = \pm 2$ and the 'forbidden' transition $\Delta M_S = \pm 3$. The parameters $g_\perp$ and D can be determined from the corresponding six equations.

---

[9] For a negative D, the arrangement of the energy levels is inverted; however the line positions remain unchanged. Thus, generally the sign cannot be determined from the measurement of the angular dependence of the line positions. Nevertheless, it can be determined by the temperature dependence of the signal intensity. Due to the occupation probabilities of the energy levels, at very low temperatures only the lower levels are occupied and, from the temperature dependence of the signal intensity one can determine the D-sign.

Thus, the three parameters $g_{\parallel}$, $g_{\perp}$ and D are over determined by the resonance equations for $B \| Z$ and $B \perp Z$, because there are more equations than unknown quantities. Therefore, the parameters can be averaged, considering the different measuring accuracies for the different magnetic field ranges.

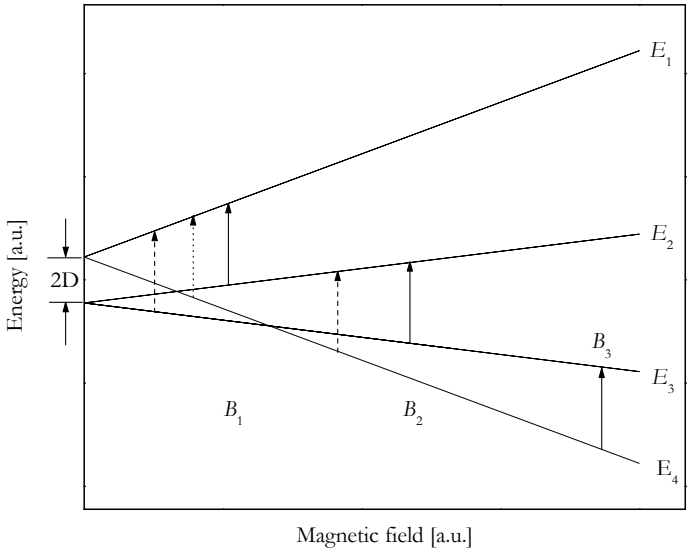

Fig. 3.6. Zeeman splitting and the possible six electron spin transitions for $h\nu > 2D$: three allowed transitions $\Delta M_S = \pm 1$ (—) as well as the two forbidden transitions for $\Delta M_S = \pm 2$ (---) and one forbidden transition for $\Delta M_S = \pm 3$ (....), corresponding to the SH (3.27) with $S = 3/2$ and $B \| Z$.

Hence, for $B \| Z$, the relation $\left|\hat{M}_S\right\rangle = \left|M_S\right\rangle$ is valid, *i.e.* the eigenfunctions $\left|\hat{M}_S\right\rangle$ are equal to the appropriate basis functions $\left|M_S\right\rangle$, and therefore only the three allowed transitions $\Delta M_S = \pm 1$ can be observed for this magnetic field.

In the case of $2D >> h\nu$, and if high enough magnetic fields are not achievable, one can only observe transitions within the spin doublet $\left|\pm 1/2\right\rangle$. This isolated doublet can then be described by the simple SH

$$\mathcal{H} = g_{eff} \beta B \tilde{S} \tag{3.38}$$

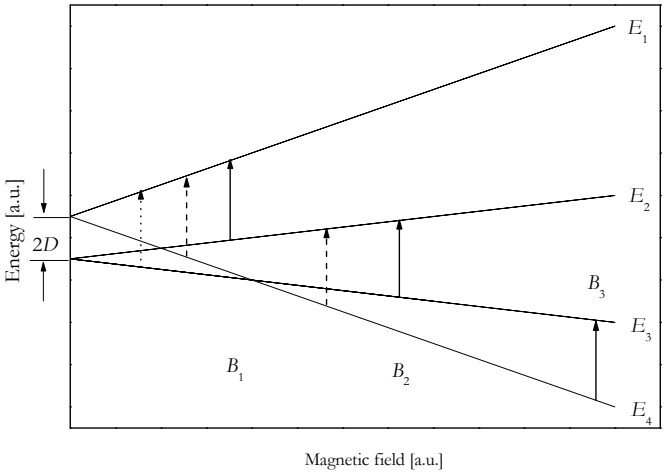

Fig. 3.7. Zeeman splitting and the possible six electron spin transitions for $h\nu > 2D$: three allowed transitions $\Delta M_S = \pm 1$ (—) as well as the two forbidden transitions for $\Delta M_S = \pm 2$ (---) and one forbidden transition for $\Delta M_S = \pm 3$ (....), corresponding to the SH (3.27) with $S = 3/2$ and $B \perp Z$.

with the effective spin $\widetilde{S} = 1/2$. Neglecting terms of the order of $\left(\frac{g\beta B}{2D}\right)^2$, the line positions may be described in first order by

$$g_{eff} = \sqrt{(g_Z^2 \cos^2\theta + (2g_\perp)^2 \sin^2\theta} \tag{3.39}$$

i.e. similarly to the spin doublet $S = 1/2$, if one sets

$$\begin{aligned} g_Z(eff) &= g_Z = g_\parallel \\ g_Z(eff) &= 2g_\perp \end{aligned} \quad . \tag{3.40}$$

This example shows how the choice of the effective spin can take place for the parametric description of the spectra. If the ground state of an ion is a spin doublet, the EPR spectra can always be described with an effective spin 1/2 and with its effective *g*-values, if the next higher energy levels lie much higher, $\Delta >> h\nu$. Considering the second order contributions given by perturbation theory, one gets the equation

$$g_{eff} = \sqrt{(g_Z^2 \cos^2\theta + (2g_\perp)^2 \sin^2\theta} \times \left[1 - \frac{3}{2}\left(\frac{g_\perp \beta B}{2D}\right)^2 \frac{\sin^2\theta(3\sin^2\theta - 1)}{3\sin^2\theta + 1}\right], \tag{3.41}$$

for the relation between the description with the effective spin $\widetilde{S} = 1/2$ by Eq. (3.38) and the description with the true spin $S = 3/2$ by the SH operator (3.27). Consequently, the result for the extreme line positions is given by:

$$\begin{aligned} g_{eff} &= g_Z = g_{\parallel} && B \parallel Z, \\ g_{eff} &= 2g_{\perp}\left[1-\frac{3}{16}\left(\frac{g_{\perp}\beta B}{2D}\right)^2\right] && B \perp Z. \end{aligned} \tag{3.42}$$

3.1.7 Fine and hyperfine structure of Mn^{2+} in a cubic crystal field

Here we address a classical practical example of an EPR spectrum. The ground state of the Mn^{2+} free ion is the orbital singlet ^6S. This state always remains as the ground state with the incorporation of Mn^{2+} in solids with a cubic CF, as long as the magnitude of the CF does not exceed a critical value[10]. For ions with an S ground state and an electron spin $S \geq 2$ (*e.g.* Mn^{2+}, Fe^{3+} with $S = 5/2$), usually one must also consider fourth order spin operators, in order to have a complete description of the possible spectra. The SH operator including these terms in a cubic CF without considering the HF transitions is given by

$$\mathscr{H} = g\beta B + \frac{1}{6}a\left[S_X^4 + S_Y^4 + S_Z^4 - \frac{1}{5}S(S+1)(3S^2+3S-1)\right] \tag{3.43}$$

where X, Y, Z are the cubic crystal axes. The second term describes the cubic FS splitting. Assuming that this FS splitting is small when compared to the Zeeman interaction, its contribution to the energy eigenvalues can be described in a good approach by first order perturbation theory. In this approximation, one gets[11]:

$$E_M = g\beta B M_S + \frac{a}{120}\left[1-5(l^2m^2+m^2n^2+n^2l^2)\right]\times\left(35M_S^4 - \frac{475}{2}M_S^2 + \frac{2835}{10}\right) \tag{3.44}$$

where l, m and n are the direction cosines between the quantization direction (the magnetic field direction) and the cubic CF axes, and M_S is given by the values $M_S = -5/2, ..., +5/2$. Between these $(2S + 1) = 6$ energy levels there are $(2S) = 5$ allowed intense transitions with $\Delta M_S = \pm 1$. In agreement with Eq. (3.44), the line positions are determined by the relations

$$h\nu = E(M_S) - E(M_S - 1) \tag{3.45}$$

from which we get:

---

[10] If the critical crystal field strength is exceeded by Dq/B~8, then the low spin state $^2T_2$ becomes the ground state.

[11] Thus, the fine structure operators are to be projected into the respective quantization direction of the Zeeman terms **Bg**, and to be computed with the eigenfunctions of the Zeeman terms $|M\rangle$. Since in the case of isotropic g, the quantization direction is given directly by the direction of the external applied magnetic field.

$$\begin{aligned} M_S = \pm 5/2 \leftrightarrow \pm 3/2 \qquad & h\nu = g\beta B \pm 2a\left[1-5(l^2m^2+m^2n^2+n^2l^2)\right] \\ M_S = \pm 3/2 \leftrightarrow \pm 1/2 \qquad & h\nu = g\beta B \mp \frac{5}{2}a\left[1-5(l^2m^2+m^2n^2+n^2l^2)\right] \\ M_S = +1/2 \leftrightarrow -1/2 \qquad & h\nu = g\beta B \end{aligned} \tag{3.46}$$

The angular dependence for these five FS line positions is represented as a function of the magnetic field in Fig. 3.8, for the rotation of the magnetic field in a {110} plane.

Each one of the electron spin transitions is split by the HF interaction of the d^5 electrons with the nuclear spin I of Mn (natural abundance 100%) into $(2I + 1) = 6$ HF lines. The SH operator for the HF interaction must be added to the SH (3.43) in order to describe this HF interaction:

$$\mathcal{H}_{HF} = \mathbf{S}\cdot\mathbf{A}\cdot\mathbf{I} \tag{3.47}$$

In the present case, the HF interaction can be assumed as isotropic and Eq. (3.38) is simplified[12]

$$\mathcal{H}_{HF} = AS_\xi I_\xi + \frac{1}{2}A(S_+I_- + S_-I_+) \tag{3.48}$$

where the ξ-axis is determined by the quantization direction **Bg** due to the Zeeman term, *i.e.* for an isotropic g, this direction is determined by the applied magnetic field.

If one regards the SH operator (3.48) as the perturbation operator, then the contribution in first order perturbation theory is

$$E^{(1)}_{Mm} = \langle M_S, m_I | \mathcal{H}_{HF} | M_S, m_I \rangle = AM_S m_I \tag{3.49}$$

causing a splitting into $2I + 1$ equidistant energy levels, with the separation between adjacent levels being proportional to the nuclear spin quantum number. The second order contribution is given by[13]

---

[12] The spin raising and lowering operators $S_\pm$ are definied by: $S_\pm = S_X \pm iS_Y$, so that $S_X = 1/2(S_+ + S_-)$ and $S_Y = (1/2i)(S_+ - S_-)$, and in equation (3.48) X and Y are to be taken as perpendicular to the ξ-axis.

[13] It is valid for $S_\pm | M_S' \rangle = \sqrt{S(S+1)-M_S'(M_S'\pm 1)}\,| M_S' \pm 1 \rangle$, and similarly $I_\pm | m_I' \rangle = \sqrt{I(I+1)-m_I'(m_I'\pm 1)}\,| m_I' \pm 1 \rangle$, thus only the following two matrix elements are not zero in Eq. (3.50): $\langle M_S, m_I | S_+I_- | M_S - 1, m_I + 1 \rangle = \sqrt{S(S+1)-M_S(M_S-1)}\sqrt{I(I+1)-m_I(m_I+1)}$ and $\langle M_S, m_I | S_-I_+ | M_S + 1, m_I - 1 \rangle = \sqrt{S(S+1)-M_S(M_S+1)}\sqrt{I(I+1)-m_I(m_I-1)}$. Therefore, for Eq. (3.50) one gets $E^{(2)}_m = \frac{1}{4}\frac{[S(S+1)-M_S(M_S-1)][I(I+1)-m_I(m_I+1)]}{g\beta B} - \frac{1}{4}\frac{[S(S+1)-M_S(M_S+1)][I(I+1)-m_I(m_I-1)]}{g\beta B}$.

$$E_{Mm}^{(2)} = \sum_{M',m'\neq M,m}\left(\frac{\left|\langle M_S,m_I\left|\mathscr{H}_{HF}\right|M_S,m_I\rangle\right|^2}{E_M^{(0)}-E_{M'}^{(0)}}\right) = \frac{A^2}{2g\beta B}\left\{M_S\left[I(I+1)-m_I^2\right]+m_I\left[M_S^2-S(S+1)\right]\right\} \tag{3.50}$$

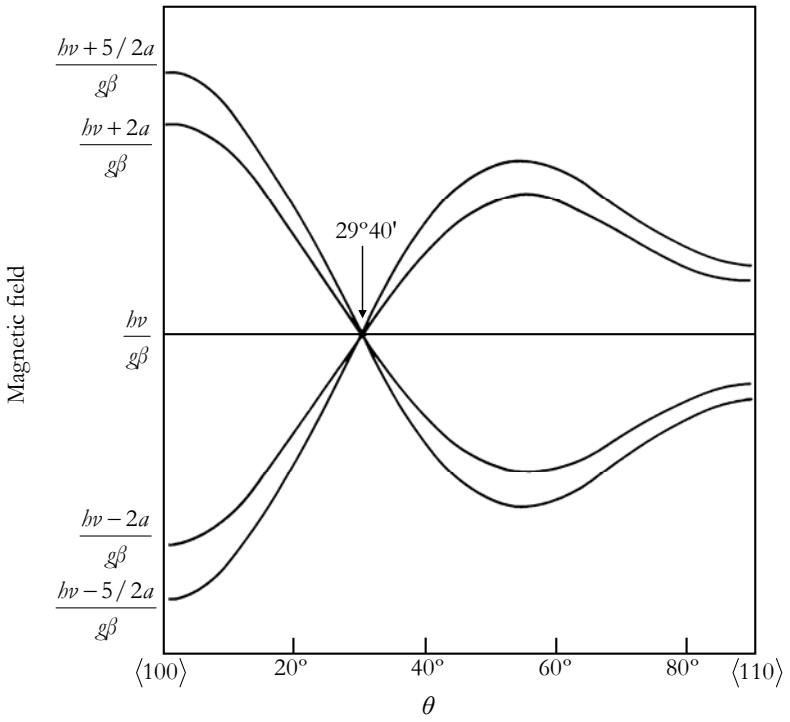

Fig. 3.8. Angular dependence of the fine structure for a ^6S ground state in a cubic crystal field as a function of the magnetic field and for the rotation of the magnetic field in a {110} plane.

Hence, in second order perturbation theory, the HF levels are no longer equidistant, and additionally, the electron spin levels are also different. The contribution $h\nu_{HF}$ to the transition energy, due to the HF interaction results in the transitions with $\Delta M_S = \pm 1$ and $\Delta m_I = 0$. Hence, from Eqs. (3.49) and (3.50) one gets

$$h\nu_{HF} = E_M^{(1)} - E_{M-1}^{(1)} + E_M^{(2)} - E_{M-1}^{(2)} = Am_I + \frac{A^2}{2g\beta B}\left\{\left[I(I+1)-m_I^2\right]+m_I(2M_S-1)\right\} \tag{3.51}$$

Due to the second order contribution, the distances between consecutive HF lines, equidistant in first order, become different and dependent on the electron spin transition. For the transition $M_S = -1/2 \leftrightarrow +1/2$, the second term in the bracketed term is omitted, and Eq. (3.51) is simplified:

$$h\nu_{HF} = E_{1/2}^{(1)} - E_{-1/2}^{(1)} + E_{1/2}^{(2)} - E_{-1/2}^{(2)} = Am_I + \frac{A^2}{2g\beta B}\left[I(I+1) - m_I^2\right] \tag{3.52}$$

From Eqs. (3.46) and (3.52), one can determine the total energy $h\nu$ of the six HF transitions for the electron spin transition $M_S = -1/2 \leftrightarrow +1/2$ with $\Delta m_I = 0$

$$h\nu = E_{1/2} - E_{-1/2} = g\beta B + Am_I + \frac{A^2}{2g\beta B}\left[I(I+1) - m_I^2\right] \tag{3.53}$$

The line positions of these six HF transitions relative to the electron spin transition $M_S = -1/2 \leftrightarrow +1/2$ is therefore independent of the magnetic field direction. Considering the HF interaction in second order of perturbation theory, the distances between the HF transitions are no longer equal.

If one observes powder samples instead of single crystals, the line positions of the electron spin transitions $M_S = \pm 5/2 \leftrightarrow \pm 3/2$, $M_S = \pm 3/2 \leftrightarrow \pm 1/2$ are strongly broadened, because of their strong dependence on the magnetic field direction, due to the different orientations of the different crystallites. Therefore, what becomes experimentally essential is only the transition which is in first order independent of the direction of the magnetic field, the $M_S = -1/2 \leftrightarrow +1/2$ transition, and the corresponding hyperfine structure.

3.1.8 Relaxation phenomenon

When the microwave radiation quanta are absorbed, they may excite the electrons to higher energy levels or even induce stimulated emission of those that already are in excited states. These transitions between Zeeman levels take place with the same probability. The spontaneous emission probability is proportional to ν^3, being observed in the optical range (10^{14} a 10^{15} GHz). In the microwave energy range ($\approx 10^{10}$ GHz), the probability of spontaneous emission is about fifteen orders of magnitude lower when compared to the optical range. That means that the spontaneous radiation can be neglected at the RF and microwave frequencies, and that the natural width of the magnetic resonance lines is very small.

The Einstein relations state that the stimulated emission and absorption coefficients are equal. Let us now consider two states n_1 and n_2, being the first one the ground state and the second one the first excited state. Absorption happens when n_1 is more populated than n_2, and the signal intensity is proportional to the population difference between these two states. When both states are equally populated, in average there will be no absorption and the system is

saturated, with no energy transfer occurring between the *ac* magnetic field and the spin system. Fortunately, there are some interactions between the electrons and their surrounding causing spin flips accompanied by the energy transfer to other degrees of freedom of the system. This process, *i.e.* non-radiative less transitions between n_1 and n_2 states, is called *spin–lattice relaxation*. Moreover, there are interactions of paramagnetic particles among each other causing a redistribution of the energy in the subsystem of spins. This is the *spin–spin relaxation*.

In the theory of the paramagnetic relaxation, the proposal has proven very fruitful to consider the magnetization process of a paramagnetic substance a two-step one. First, equilibrium is established within the spin system, and then an energy exchange between the spin system and the lattice occurs. Here we ascribe to the "lattice" all other degrees of freedom of our paramagnetic substance. It is quite clear that such a treatment is only possible if the spin–spin interactions are much stronger than the spin-lattice ones.

3.1.9 Powder spectrum

In a single crystal, the resonance field or frequency depends on the orientation of the single crystal with respect to the applied magnetic field, and EPR analysis yields both the whole set of SH parameters and the orientation of the principal axes of the local ligand field with respect to crystallographic axes. In the case of powders and polycrystalline solids, this relative orientation cannot be determined because the paramagnetic centres are randomly oriented with respect to the applied field, so that each orientation has the same probability of occurring. Then the magnetic resonance spectrum, referred to as a *powder spectrum*, is an average over the resonance conditions for all possible orientations of the paramagnetic centre, and the interpretation is only based on the determination of the SH parameters, whose values reflect the local symmetry of the paramagnetic centre.

Nevertheless, if the paramagnetic spectrum is completely isotropic, it can be examined in a powder without loss of resolution. On the other hand, in a powder the spectrum of any ion that is anisotropic will naturally spread out; the details of the spectrum will be lost to a considerable extent, and the information may be significantly reduced.

In most cases an analytical expression is not possible, and one must resort to computer-based numerical integration techniques to calculate the powder spectrum $S(B)$.

Generally, the resonance position $B_{res}(\Omega)$, the intensity $I(\Omega)$ and the line width $W(\Omega)$ depend on the relative orientation Ω between the paramagnetic centre and the laboratory frame.The powder spectrum is an integral function[14] of the field. The origin of the integral function is the orientation-dependent single crystal spectrum. Thus, one must integrate over all possible orientations of the paramagnetic centre to obtain the powder spectrum

$$S(B) = \oint_{\Omega} I(\Omega) f\left[B - B_{res}(\Omega), W(\Omega)\right] d\Omega . \tag{3.54}$$

If, for simplicity, one neglects the line width W, one obtains the delta spectrum

$$S(B) = \oint_{\Omega} I(\Omega) \delta_D\left[B - B_{res}(\Omega)\right] d\Omega , \tag{3.55}$$

where δ_D is the Dirac delta function. Applying the Heaviside function $\frac{dH}{dx} = \delta_D(x)$ to Eq. (3.55), one gets

$$S(B) = \frac{d}{dB} \oint_{\Omega} I(\Omega) H\left[B - B_{res}(\Omega)\right] d\Omega , \tag{3.56}$$

and, consequently,

$$S(B) = \frac{d}{dB} \oint_{B \geq B_{res}(\Omega)} I(\Omega) d\Omega . \tag{3.57}$$

This means that the powder spectrum is a weighted surface integral over all orientations where B_{res} is smaller than the given B.

3.2 FERROMAGNETIC RESONANCE

Ferromagnetic resonance (FMR) or spin resonance at microwave frequencies in ferromagnets is similar in principle to EPR. The total electron magnetic moment of the substance precesses about the direction of the applied magnetic field, and the energy is strongly absorbed from the microwave field when its frequency equals the precessional frequency. As an analogy, one may think of the macroscopic vector **S** representing the total spin of the ferromagnet as quantized in the applied magnetic field, with energy levels separated by the usual Zeeman energies (the magnetic selection rule $\Delta M_S = \pm 1$ only allows transitions between adjacent levels). However, there are unusual features in ferromagnetic resonance, which include very large transverse

[14] Note that an integral function is defined as $F(x) = \int f(x,t)\, dt$.

susceptibility components χ' and χ''; the shape of the sample plays a major role; the strong exchange coupling between ferromagnetic electrons tends to suppress the dipolar contribution to the line width; and saturation effects occur at low microwave power levels.

Nevertheless, as other resonance phenomena, FMR is characterized by the resonant magnetic field and by the line shape and width. One may use measurements of the line position at different frequencies and geometries to determine parameters that characterize the magnetic materials, such as the magnetization and the magnetic anisotropy. FMR may also be useful to evaluate magnetic inhomogeneities which may not be analysed by other experimental methods.

The following FMR theory is described in detail in the book of Vonsovskii (1966).

The magnetic moment precesses about the static magnetic field at the Larmor frequency ω_0. When a spin finds itself in a uniform magnetic field **B**, it is subjected to a binary that tends to align its magnetic moment with the magnetic field in order to reach a configuration of minimum energy.

In quantum theory, the angular precession frequency $\boldsymbol{\omega}_0$ of the orbiting spin, the Larmor frequency, is given by

$$\boldsymbol{\omega}_0 = \gamma \mathbf{B} \tag{3.58}$$

where $\gamma = g\mu_B / \hbar$ is the gyromagnetic ratio. In FMR the local field may differ by a few kG from the applied magnetic field, due to the internal field produced by the aligned magnetic moments. To describe this situation, one may introduce the concept of effective magnetic field, *i.e.* one may take into account the contributions of the interactions occurring in the ferromagnetic material assuming that the spins responsible for the ferromagnetic properties precess at the frequency ω_0 about the effective field $\mathbf{B}_{eff}$ instead of **B**. Hence, Eq. (3.58) takes the form $\boldsymbol{\omega}_0 = \gamma \mathbf{B}_{eff}$, and the equation of motion for the magnetization **M** is given by

$$\frac{d\mathbf{M}}{dt} = -\gamma \mathbf{M} \times \mathbf{B}_{eff} . \tag{3.59}$$

Let us consider a spherical coordinate system, where the orientations of the magnetization vector relatively to the Cartesian coordinate system (*X*, *Y*, *Z*) defined by the polar θ and azimuthal φ angles are given by:

$$M_X = B\sin\theta\cos\varphi; \quad M_Y = M\sin\theta\sin\varphi; \quad M_Z = M\cos\varphi, \tag{3.60}$$

as illustrated in Fig. 3.9. Hence, the effective magnetic field radial, polar and azimuthal components may be written as:

$$\begin{aligned} B_M &= B_X \sin\theta\cos\varphi + B_Y \sin\theta\sin\varphi + B_Z \cos\theta, \\ B_\varphi &= B_X \cos\theta\cos\varphi + B_Y \cos\theta\sin\varphi - B_Z \sin\theta, \\ B_\theta &= -B_X \sin\varphi + B_Y \cos\varphi \end{aligned} \quad . \tag{3.61}$$

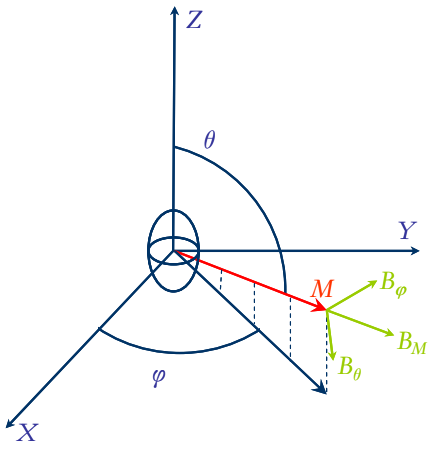

Fig. 3.9. Graphical representation of the internal effective field components B_M, B_φ, B_θ in a spherical coordinate system.

Moreover, taking into account that the first time derivative of M in spherical coordinates is $\dot{M}\hat{M} + M\dot{\theta}\hat{\theta} + M\sin\theta\dot{\varphi}\hat{\varphi}$, assuming that the magnetization is constant, the equations of motion are now given by

$$\begin{aligned} \dot{\theta} &= \gamma B_\varphi, \\ \dot{\varphi} &= -\frac{\gamma}{\sin\theta} B_\theta. \end{aligned} \quad , \tag{3.62}$$

In a state of thermodynamic equilibrium, the direction of the ferromagnetic magnetization vector **M** coincides with the direction of the internal effective field $\mathbf{B}_M$, which magnitude is determined by the free energy F per unit volume:

$$B_M = -\frac{\partial F}{\partial M}, \tag{3.63}$$

and, in this case, the components of the effective field along the directions θ and φ are absent. The equilibrium orientation of the magnetization vector **M** defined by the angles θ_0 and φ_0 is determined by the free energy minimum

$$F_\theta \equiv -\frac{\partial F}{\partial \theta} = 0; \qquad F_\varphi \equiv -\frac{\partial F}{\partial \varphi} = 0\,. \tag{3.64}$$

In this way, working out the free energy's minimum allows us to obtain unambiguously the equilibrium direction of the magnetization vector only if it is homogenous over the whole sample or if the system may be defined as an ensemble of homogeneously magnetized regions.

Let us now consider the situation in which the system is not in equilibrium, *i.e.* when small deviations from the magnetization equilibrium position occur. In this case, the conditions (3.64) are no longer valid and the magnetization will be changed by the polar and azimuthal components of the internal effective magnetic field which are no longer zero

$$B_\theta = -\frac{F_\theta}{M}; \qquad B_\varphi = -\frac{F_\varphi}{M\sin\theta}\,. \tag{3.65}$$

If one considers that the deviations from the equilibrium given by

$$\delta\theta(t) = \theta(t) - \theta_0; \qquad \delta\varphi(t) = \varphi(t) - \varphi_0\,, \tag{3.66}$$

are small relatively to the equilibrium values (θ_0 and φ_0), one may write the free energy expression in terms of a linear expansion of the terms F_θ and F_φ :

$$F_\theta = F_{\theta\theta}\delta\theta + F_{\theta\varphi}\delta\varphi; \qquad F_\varphi = F_{\varphi\theta}\delta\theta + F_{\varphi\varphi}\delta\varphi\,, \tag{3.67}$$

where $F_{\theta\theta}$, $F_{\varphi\varphi}$, $F_{\theta\varphi}$, $F_{\varphi\theta}$ are the second derivatives of the free energy with respect to the angles, calculated for the equilibrium position. Combining Eqs. (3.62), (3.65) and (3.67) one obtains a linear system of equations that describe the magnetization vector small oscillations relatively to the equilibrium positions:

$$\begin{aligned} -\frac{M}{\gamma}\sin\theta_0 \cdot \delta\dot{\theta} &= F_{\varphi\theta}\delta\theta + F_{\varphi\varphi}\delta\varphi, \\ \frac{M}{\gamma}M\sin\theta_0 \cdot \delta\dot{\varphi} &= F_{\theta\theta}\delta\theta + F_{\theta\varphi}\delta\varphi. \end{aligned} \tag{3.68}$$

This system of homogenous equations has the periodic solutions $\delta\theta$, $\delta\varphi \approx \exp(i\omega t)$. The precession of a total magnetic moment with free energy F occurs at a frequency ω given by the resonance condition

$$\omega = \frac{\gamma}{M\sin\theta_0}\sqrt{F_{\theta\theta}F_{\varphi\varphi} - F_{\theta\varphi}^2}\,. \tag{3.69}$$

Although Eq. (3.69) is mathematically correct, it is physically not convenient. The origin of the different terms in F is not clear due to the angular dependent mixing. In this sense, the following relation was derived [Baselgia (1988)]:

$$\left(\frac{\omega}{\gamma}\right)^2 = \frac{1}{M^2}\left[F_{\theta\theta}\left(\frac{1}{\sin^2\theta_0}F_{\varphi\varphi} + \frac{\cos\theta_0}{\sin\theta_0}F_{\theta}\right) - \left(\frac{1}{\sin\theta_0}F_{\theta\varphi} - \frac{\cos\theta_0}{\sin^2\theta_0}F_{\varphi}\right)^2\right]. \tag{3.70}$$

So, in order to obtain the resonance frequency of the system, it is necessary to have a concrete expression for the free energy that describes the system and that depends on the orientation of the magnetization. Generally, a free energy per unit volume may be described by the sum of its contributions

$$F = F_0 + F_{dem} + F_a + F_{m\cdot e} + F_{exch} + F_d + F_{surf}\,, \tag{3.71}$$

where F_0 represents the interaction energy of the magnetization with the external field (Zeeman energy), which depends on the angle between the magnetic field and the magnetization, F_{dem} is the energy of the demagnetizing field of the surface "magnetic charges", F_a is the magnetocrystalline anisotropy energy which depends on the relative orientation of the magnetization and the crystal principle axes, $F_{m.e}$ corresponds to the magneto-elastic energy which is a function of the direction of the magnetization and the stresses, F_{exch} stands for the exchange energy connected to the spatial inhomogeneity of the magnetization, F_d is the energy of the inter-domain boundary layers, and finally F_{surf} is related to the surface of sample. The term expressing the exchange energy related to the molecular field that produces the spontaneous magnetization was not included because it does not depend on the orientation of the magnetization.

The effect on the resonance phenomenon of the shape of the sample, of crystal anisotropy, stresses, inhomogeneous magnetization and domain structure are determined by the components of the effective internal magnetic field, being its relevance dependent on the material properties and on the experimental conditions.

If the external magnetic field is sufficiently strong to magnetize the sample to a state approaching saturation, the sample's behaviour will be identical to that of one region of spontaneous magnetization, and the term F_d would be removed from Eq. (3.71). On the other hand, in weak external fields, the sample has a random magnetization region structure, which is energetically favourable, and in this case the system is extremely sensitive to the presence of impurities and to small perturbations of the crystal lattice.

When the samples are highly conductive, the microwave field is able to penetrate only a thin surface layer, leading to inhomogeneity of the magnetization. In this case, besides the losses related to the ferromagnetic resonance, there also are losses due to Foucault currents induced in the conductive sample by the microwave magnetic field. These circulating currents create magnetic fields that oppose the effect of the changing field (Lenz's law). Hence, the homogeneous magnetization is reached only when the dimensions of the sample are large enough so that the material exhibits ferromagnetic properties, and are simultaneously small enough when compared with the thickness of the skin layer. For ferromagnetic semiconductors, the Foucault currents and the surface effect may be neglected, because the conductivity of these materials is $10^8 – 10^{13}$ smaller than that of metals and alloys.

The significance of the contribution of the internal effective field components due to the magnetocrystalline anisotropy is related to the type of sample, and is most relevant for single crystals. In the majority of cases, its influence is very small when compared to the external field, nevertheless in some substances, such as cobalt, its contribution is comparable to that of the demagnetizing field so that the magnetocrystalline anisotropy has to be considered.

The contributions of internal stresses, arising from growth processes or even from experimental conditions, have a relatively small effect on the resonance conditions.

Finally, the demagnetizing fields depend on the dimensions and on the shape of the samples, and have approximately the same order of magnitude of the applied magnetic field, in the case of a ferromagnetic material.

3.2.1 Magnetocrystalline anisotropy energy

The magnetic anisotropy is the direction dependence of a material's magnetic properties. A magnetically isotropic material has no preferential direction for its magnetic moment in zero field, while a magnetically anisotropic material will align its moment to an easy axis.

The magnetocrystalline anisotropy is a special case of magnetic anisotropy and may be defined as the energy cost per atom to align its magnetization from one crystallographic direction to another. Consequently, the orientation of the magnetization is given by the equilibrium condition determined by the minimum of the magnetic part of the total energy of the system.

The spin-orbit coupling is the direct source of magnetocrystalline anisotropy energy. The orbital momentum of bulk 3*d* metals is almost quenched due to cubic symmetry. The *g*-factor for bulk 3*d* metals is close to the *'spin-only'* value (2.0023), which means that the magnetism in these transition metals can be ascribed mainly to the spin of the delocalized 3*d* electrons. The electron spin, however, is weakly coupled to the orbital momentum via spin-orbit coupling[15], and consequently the energy of the system depends on the relative orientation between the magnetization (spin orientation) and the crystal axes.

If we assume that in a solid the CF forces the electron to move in a certain crystallographic plane, the electron spin will be aligned in a direction normal to this plane[16]. In such way, a uniaxial anisotropy can arise regardless of the shape of the crystal. Large magnetocrystalline anisotropy energy can be expected in ultra thin films due to the reduced symmetry of distorted lattices, interfaces, surfaces, and the presence of microscopic roughness. It is shown by a perturbation theory that the energy difference between easy and hard direction is related to the anisotropy of the orbital momentum [Bruno (1989)]. This part of the magnetocrystalline anisotropy energy (the electronic part) is defined as the difference in the total energy of the system for two different directions of the magnetization. Once one realizes that the magnetocrystalline anisotropy energy is a quantity describing the interaction between the electron spin and the lattice, it is intuitively clear that changes of the lattice constant will affect the magnetic properties.

The saturation magnetization $\mathbf{M}_{Sat}$ is reached when the field is high enough to align all individual magnetization vectors with the applied field. In order to calculate the resonance frequency, we must have a concrete expression of the anisotropy energy, which may be represented as an exponential series with respect to the direction cosines α_1, α_2, α_3 of the magnetization vector relative to the crystal's principal axes [Vonsovskii (1966)]:

$$F_a = K_0 + K_1\left(\alpha_X^2\alpha_Y^2 + \alpha_Y^2\alpha_Z^2 + \alpha_Z^2\alpha_X^2\right) + K_2\alpha_X^2\alpha_Y^2\alpha_Z^2 + \cdots, \tag{3.72}$$

---

15 For 3*d* transition metals, the orbital is largely quenched, but not completely. Furthermore, when the cubic crystalline symmetry is broken through lattice distortion, the quenching of the orbital momentum is partially lifted.

16 On the atomic level, the crystal field exerted on the moving electrons by the neighbouring atoms will force the orbitals to align with the crystal field. The orbital momentum of the electron is coupled to the electron spin via the spin-orbit coupling. Consequently, the crystal field influences the spin direction through the orbital momentum. Therefore, the magnetocrystalline anisotropy energy and the anisotropy of the orbital momentum will have similar symmetry.

where K_0, K_1 and K_2 are the 'zero', the first and second anisotropy constants. The 'zero' anisotropy constant corresponds to the energy of a single crystal magnetized to saturation along the easy axis. In the case of crystals with hexagonal symmetry one gets

$$F_a = K_0 + K_1 \sin^2\theta + K_2 \sin^4\theta \,, \tag{3.73}$$

where θ is the angle between the magnetization vector and the hexagonal symmetry axes. The constants K_1 and K_2 represent energy densities (J.m^{-3}), being strongly dependent on the temperature. Generally, one finds values of F_a in the range $10^2 - 10^7$ J.m^{-3}, which corresponds to an energy per atom of the order of $10^{-8} - 10^{-3}$ eV. When the constants K_1 and K_2 are positive, the energy is minimized for $\theta = 0^o$, and this is the easy axis of the crystal.

3.2.2 Shape anisotropy

The energy term of the demagnetizing field arises due to *shape anisotropy*, which is related to the shape of the sample and arises from magnetostatic effects (*e.g.* dipolar interactions). Due to the periodic ordering of the dipoles within a crystal lattice, the magnetic interaction energy depends on the orientation of the dipoles relative to the crystal lattice. For example, in the case of thin films, due to this shape anisotropy, the free energy is minimized when the magnetization is aligned with the plane of the film, as expressed by

$$F_{shape} = \frac{1}{2}\mu_0 M^2 \cos^2\theta \,, \tag{3.74}$$

where θ is the angle between the normal to the film and the magnetization vector, and μ_0 is the free space permeability. This demagnetizing effect is produced by the uncompensated magnetic dipoles on the surface of the sample.

4 EXPERIMENTAL METHODS

In this chapter I will address and describe the main experimental methods used for material growth, magnetic and structural characterization of the samples in this work, namely pulsed laser deposition (PLD), electron magnetic resonance (EMR), superconducting quantum interference device (SQUID) magnetometry, Hall effect, X-ray diffraction (XRD), scanning electron microscopy (SEM), and transmission electron microscopy (TEM).

4.1 PULSED LASER DEPOSITION

Pulsed laser deposition has been proven to be a versatile technique for the growth of high-quality ZnO-based thin films [Lorenz (2005), (2008)]. PLD is a growth method by condensation of a laser plasma ablated from a single target, excited by the high-energy laser pulses far from equilibrium. PLD uses high-power laser pulses with an energy density of more than 108 W cm^{-2} to melt, evaporate, excite, and ionize material from a single target. This laser ablation produces a transient, highly luminous plasma plume that expands rapidly away from the target surface. The ablated material is collected on an appropriately placed substrate surface upon which it condenses and a thin film nucleates and grows. PLD is a conceptually fairly easy process which is shown schematically in Fig. 4.1. A pulsed high-power laser beam is focussed onto a target surface in order to produce a high power density. Upon the laser energy absorption, the target material is evaporated, excited and ionized. A highly luminous plasma plume is formed and expands away from the target. Finally, the ablated species condense on a substrate surface. The fact that the plasma plume faces the substrate perpendicularly results in a better lateral homogeneity of the species arriving at the substrate for thin film growth. Relevant from a more practical point of view is that the ablation takes place on a short time scale, in the nanosecond range, to minimize the dissipation of the laser energy beyond the volume of the melted and ablated surface layer of the target. Only within this condition, thermal destruction of the target together with phase segregation will be avoided. Furthermore, a well known major advantages of PLD is that the relative concentration of elemental species within the plasma plume corresponds to the chemical composition of the target material. Compared to other common growth techniques, such as molecular beam epitaxy (MBE) or metal organic vapour deposition (MOCVD), PLD is an advantageous technique since it is faster, it offers great experimental

versatility, and it enables the production of complex multicomponent samples from a single target source.

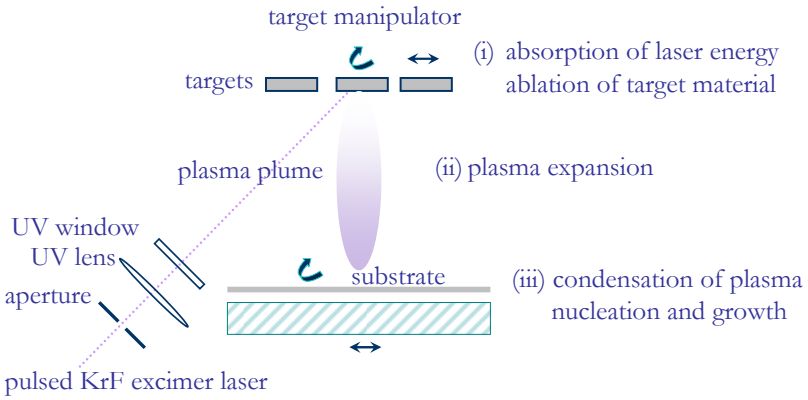

Fig. 4.1. Scheme of a typical PLD setup for large-area film growth [Lorenz (2008)].

To grow ZnO-based nanostructures Lorenz *et al.* (2005) developed a unique low-vacuum PLD process, which was used to grow the nanowires studied in this thesis. At the University of Leipzig, the deposition chamber, schematically represented in Fig. 4.2, consists of a T-shape quartz tube with an outer diameter of 30 mm. A pulsed high-power KrF excimer laser beam (248 nm) is guided to the deposition chamber inside a protection shielding, enters along the centre bar of the T, and is focused by a UV lens on the cylindrical target surface of one of the rotating PLD targets. In this system one can fit up to three targets onto the linear rotary feedthrough bar, allowing in situ modulation of the chemical composition of the nanostructures. An encapsulated heater is built around the quartz tubes, so that the temperature at which the nanostructures are grown may be varied between room temperature and 950 ºC. The gas flow is directed from the target towards the substrate and thus supports the transport of material from the plasma plume.

The position of the nanostructures can be pre-determined by a catalyst pattern on the substrate prior to growth. In this work, gold was used as a growth catalyst in the form of colloidal particles, and Ar was used for the background gas flow.

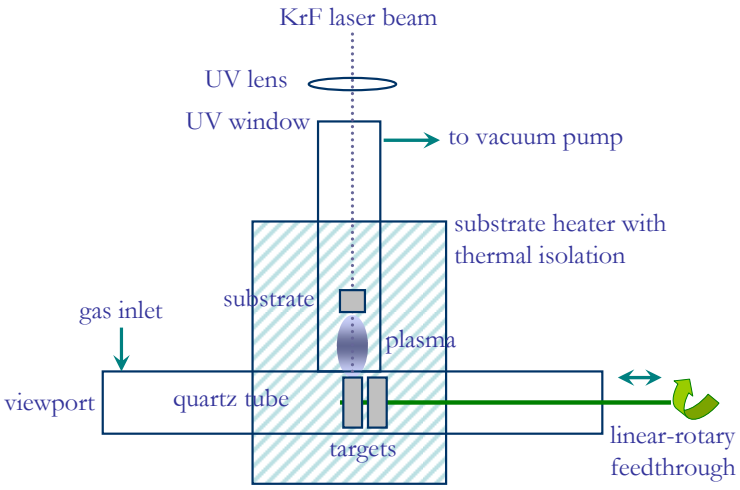

Fig. 4.2. Top view scheme of the high-pressure PLD setup for nano-heterostructures [Lorenz (2005)].

4.2 Electron magnetic resonance

Electromagnetic radiation may be understood as the coupling between electric and magnetic fields perpendicular to the direction of propagation, both oscillating at the same frequency ν. In EMR, referring to both electron paramagnetic and ferromagnetic resonances (EPR and FMR), the commonly used frequency range is 1-100 GHz.

In a common EMR system, the electromagnetic radiation frequency is kept constant while the magnetic field is swept. The level splitting (Zeeman effect) occurs due to the static field which is applied to the sample. By sweeping the magnetic field, the separation between the energy levels is varied, until this separation is equal to the microwave photon energy (resonance condition). A typical EMR spectrometer, as shown in Fig. 4.3, may be divided into the following parts:

1. Microwave bridge
2. Microwave cavity
3. Electromagnet and power supply
4. Field modulation unit
5. Signal Channel ("Console")
6. User interface (Computer)

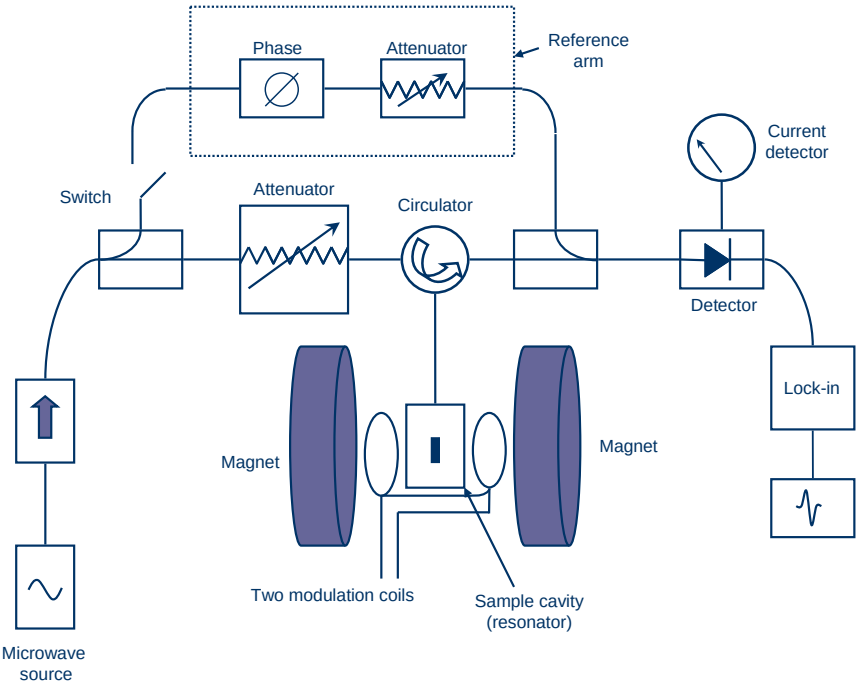

Fig. 4.3. Block diagram of an EMR homodyne spectrometer. Taken from Pilbrow (1990).

First, it is necessary to have a microwave source and all accessories to guide, control and detect the microwave radiation (waveguides, attenuators, circulators, and other elements that compose the microwave bridge). The *microwave bridge* functions both as a microwave source and a detector of the radiation reflected from the resonant cavity. In the microwave range ($1 \leq \nu \leq 100$ GHz) the radiation is generated by a klystron or a Gunn diode which is provided with an automatic frequency control (AFC). In our X-band (≈9.4 GHz) spectrometer, the microwaves are generated through a Gunn diode, a semiconductor oscillator that is widely used to produce relatively low power signals at microwave frequencies. The emitted microwave frequency depends on the thickness of the active region. The output radiation, almost monochromatic, is determined by mechanical tuning of the cavity. This is achieved by placing an adjustable screw into the waveguide cavity. In the case of the used Q-band (≈34 GHz), since the Gunn oscillator is linked to a waveguide, the frequency is not permanent, and manual adjustments can be done during the tuning process before each experiment. For measuring EMR in the absorption mode, the AFC regulates the spectrometer in a way that the dispersion part of the susceptibility is ruled out by stabilizing the source frequency to the resonance frequency of the cavity. To control the power output of the microwave source, there exists a variable attenuator that blocks the flow of the microwave radiation. A frequency counter measures the radiation

frequency. A circulator forces the incident microwave radiation to the microwave cavity and directs the reflected power to the detector. The static magnetic field is generated by an *electromagnet* equipped with a stabilizing, sweeping and measuring system. In order to reduce the signal to noise, a modulation and phase sensitive detection method (*lock-in*) is applied. The *signal channel* is built into the console that contains the required electronics for the phase sensitive detection. Modern *X*-band spectrometers achieve a sensitivity of about 10^9 spins per mT under standard conditions. While in optical spectroscopy one modulates the radiation intensity, in EMR the applied magnetic field is modulated. The static applied magnetic field is overlapped by an *ac* magnetic field produced by a pair of Helmholtz coils. If the modulation amplitude is smaller than 1/2 the absorption signal line width, the derivative of the absorption signal is correctly reproduced for most of the practical objectives. The microwave power reflected from the cavity is split into two components: one transmits the frequency error signal to the AFC and the other goes to the preamplifier. The latter is filtered by a lock-in detector (commonly operating at 100 kHz) that eliminates a large part of the noise. The reference arm guides the microwave power from the source directly to the detector, promoting an appropriate biasing of the working point of the detector.

The cavity where the sample is placed is the *resonant cavity*, a metal box that aids the amplification of weak signals from the sample, and which dimensions are equal to the microwave length, creating a standing wave pattern. The cavity walls are highly conductive in order to increase the quality factor. Different shapes of resonators may be employed for measuring EMR [Poole (1983)]. The commonly used resonators are the cylindrical TE_{011} and the rectangular TE_{102} cavities. In both cavities the electric field standing wave is aligned in the plane perpendicular to the vertical axis. The location of the maximum of the microwave magnetic field $\mathbf{B}_1$ corresponds to the location of the minimum of the electric field component. Usually, $\mathbf{B}_1$ is chosen perpendicular to the static magnetic field direction, and the sample should be placed where $\mathbf{B}_1$ has its maximum value.

The cavity may be represented by a parallel resonant circuit which is tuned with the waveguide in order to equalize the impedances and, in consequence, reduce the reflection to zero. The coupling of the cavity to the waveguide and the tuning are accomplished by mechanically varying the position of a screw that covers a small coupling hole in the cavity wall (iris). In the case of the critical coupling, all of the microwave energy is stored in the cavity, being dissipated in the form of heat, and there is no power reflection. When the

resonance conditions are satisfied, part of the radiation in the cavity is absorbed by the sample, causing a change in the impedance, and consequently, of the coupling between the cavity and the microwave guide. Hence, part of radiation is now reflected and sent to the detector which converts that reflected radiation into measurable electrical current. The latter represents the EMR signal.

The *quality factor* of the empty cavity, Q, describes how well the cavity stores the microwave energy. To compare measurements performed in different cavities, one must know the quality factors Q_e of the unloaded resonators:

$$Q_e = \frac{2\pi(\text{energy stored in the resonator per cycle})}{\text{dissipated energy per cycle}}. \tag{4.1}$$

The higher the energy loss, the lower is the sensitivity of the spectrometer. Some of the microwave energy can be lost to the side walls of the cavity, since electrical currents are generated which contribute to heat production. In order to reduce the dielectric losses and to enhance the magnetic absorption, the sample is placed in an electric field minimum and a magnetic field maximum. Thus, larger signals and higher sensitivities can be obtained. In addition, there are energy losses due to the cavity coupling hole. These losses may be quantified by the coupling quality factor Q_r and the dielectric factor Q_ε, respectively. Thus, the overall quality factor Q is given by summing the reciprocals of the different factors [Poole (1983)],

$$Q = \frac{1}{Q_e} + \frac{1}{Q_r} + \frac{1}{Q_\varepsilon}. \tag{4.2}$$

An estimate of the quality factor of the resonator is given by

$$Q = \frac{\nu}{\Delta\nu}, \tag{4.3}$$

where ν is the microwave frequency and $\Delta\nu$ is the full width at half maximum (FWHM) of the cavity resonance curve [Poole (1983)]. Cylindrical cavities generally have a significantly higher Q_e factor than rectangular ones. It is noteworthy that the sensitivity of the EMR is proportional to the product of the quality factor Q by the filling factor η. The filling factor is a measure of the efficiency with which the microwave magnetic field is concentrated at the sample. Derived expressions of η for particular cases commonly observed in EMR experiments may be found in the book of Poole (1983). In general, the filling factor is proportional to the ratio between the

sample volume and the cavity volume. Thus, the increase of the sample volume raises the value of the filling factor, whereas Q tends to decrease due to the dielectric losses. Thus, the optimum sample size for the highest sensitivity is strongly dependent on the used microwave frequency and sample properties.

EMR spectra are usually sensitive to the sample temperature. To control this measurement parameter, a cryogenic system is required (which may be coupled to a heating system).

The EMR spectra were measured in the X-band (≈ 9.4 GHz) and in the Q-band (≈ 34 GHz) at temperatures between 4 and 300 K using a Bruker ESP 300E spectrometer equipped with Oxford Instruments continuous flow helium cryostats, appropriate for each one of the frequency cavities.

4.3 SQUID MAGNETOMETRY

Magnetization measurements are very useful to determine the type of magnetic ordering in a sample. Ferromagnetic materials are easily identified by their characteristic hysteresis loop. An external magnetic field is applied until the sample experiences saturation, as the individual domains align along the direction of the applied field. When the magnetic field is removed, the magnetization doesn't disappear. Instead, some of the domains remain aligned with the removed field. The presence of an external opposing magnetic field large enough to cancel out the remnant magnetization, the coercive field, is necessary to saturate the spins in the opposite direction. Thus, one obtains a symmetric hysteresis loop.

SQUID magnetometry is one of the most sensitive methods available to detect magnetic fields, and uses the electron-pair wave coherence and the Josephson effect to perform this task. A SQUID sensor consists of two parallel Josephson junctions within a superconducting ring. A Josephson junction is formed by two superconductors separated by a thin insulating layer (superconductor – isolator – superconductor). The Josephson effect consists of the tunnelling with phase coherence of electrons through a thin isolating layer placed between two superconductors. Electrons in superconductors minimize their energy by forming Cooper pairs, as temperature drops below the critical temperature at which superconductivity sets in. Due to the quantum mechanical nature of the Cooper pairs, they propagate through the lattice without dissipating energy. If a constant current bias is maintained across the ring as illustrated in Fig.

4.4, the current divides equally between the two Josephson junctions. Only a multiple of the magnetic flux quantum can flow through the superconducting ring (flux quantization). If the applied flux is not an exact multiple of the flux quanta, the excess flux is cancelled by a circulating current around the ring. The circulating current will flow in a direction which cancels any excess flux. If the current flows clockwise, it will add to the top Josephson junction's current and subtract from the lower one. Applying a linearly changing magnetic flux will cause the circulating current to vary as a sinusoid (similarly to the Young's double-slit interference), and can be measured as a voltage across the SQUID.

This technique is very useful to obtain information about the magnetic properties of the samples from their hysteresis loop and from their initial magnetization curve. The parameters that one can obtain are the susceptibility χ, the coercive field B_C, the remnant magnetization M_R, and the saturation magnetization M_{Sat}.

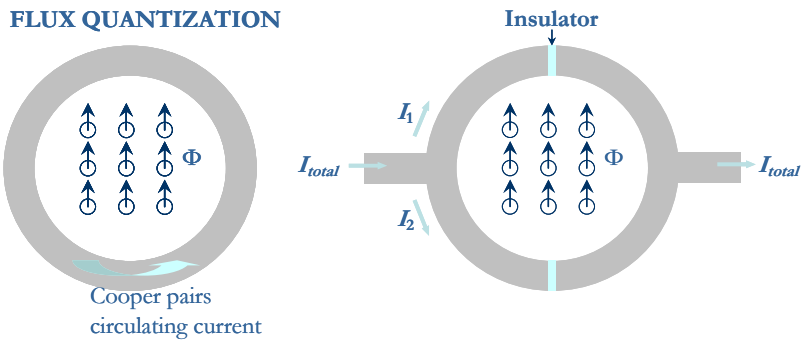

Fig. 4.4. Superconducting quantum interference device (SQUID): the principle of magnetic flux quantization by the Cooper pairs current; Josephson junction within a superconducting ring.

4.4 HALL EFFECT AND MAGNETORESISTANCE

The Hall effect is used to characterize semiconductor materials, since, when complemented with conductivity measurements, it allows the determination of the type, concentration and mobility of the charge carriers. With isolated conductivity measurements in semiconducting materials one can only determine the product between the carrier concentration and mobility.

The Hall effect is based on Lorentz's law which establishes the relation between the force produced on a moving charge carrier and the magnetic and electric fields. This effect may be

used to distinguish a *p*- from an *n*-type semiconductor, and to simultaneously measure the carrier mobility and concentration.

Let's consider a charge q which moves with a velocity $\mathbf{v} = v_x \hat{\mathbf{i}}$ in a magnetic field $\mathbf{B} = B_z \hat{\mathbf{k}}$ (see Fig. 4.5). The force **F** acting on the charge q is given by:

$$\mathbf{F} = q\mathbf{v} \times \mathbf{B} . \tag{4.4}$$

For both positive (hole) and negative (electron) charge carriers, the magnetic force points in the negative direction of the *y*-axis. In the case of a *p*-type semiconductor, an accumulation of positive charge will occur at $y = 0$, while in the case of a *n*-type semiconductor, a negative charge accumulation will be observed. At $y = l$, for each of the latter cases, an excess of charge carriers with a sign opposite to that of the carriers accumulated at $y = 0$ will take place.

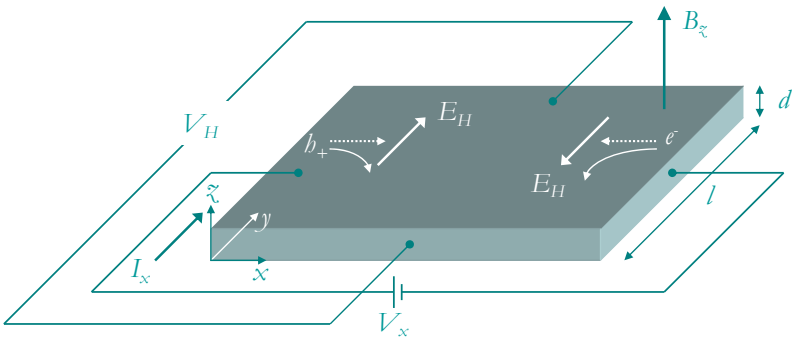

Fig. 4.5. Schematic representation of the Hall effect [Neamen (2003)].

The excesses of charge observed along the *y*-axis create an electric field (Hall field) E_H along this direction, which in the stationary state originates a force acting on the charge carriers which has the same magnitude as the magnetic force given in Eq. (4.4), hence:

$$qE_H = qv_x B_z . \tag{4.5}$$

The potential difference created along the *y* direction is called the transverse Hall voltage V_H which is given by

$$V_H = E_H l = v_x B_z l . \tag{4.6}$$

Assuming that a constant current I_x flows along the *x* direction, the Hall voltage may be expressed by:

$$V_H = \frac{I_x B_z}{qnd} = \frac{I_x B_z R_H}{d}, \tag{4.7}$$

where n is the carrier concentration, d is the sample thickness, and $R_H = 1/(qn)$ is the Hall coefficient. Both the Hall voltage and the Hall coefficient are positive in the case of a *p*-type semiconductor, and negative for a *n*-type semiconductor.

Taking into account the well known definitions of current density and conductivity σ, the carrier mobility μ can be determined from the values of V_H and R_H:

$$\mu = R_H \sigma \,. \tag{4.8}$$

The carrier type, mobility, and conductivity of a semiconducting material can be determined through the measurement of the resistivity ϱ using the van der Pauw method illustrated in Fig. 4.6. To use the van der Pauw configuration, the sample shape is arbitrary, nevertheless, the thickness must be homogeneous and much smaller than the width and length of the sample, and four small peripheric Ohmic contacts are necessary. In these conditions, the resistivity ϱ is given by

$$\varrho = \frac{1}{\sigma} = \frac{\pi d}{2\ln 2}\left(R_{AB,DC} + R_{CB,DA}\right) = \frac{\pi d}{2\ln 2}\left(\frac{V_D - V_C}{I_{AB}} + \frac{V_D - V_A}{I_{CB}}\right), \tag{4.9}$$

where $R_{ij,pq}$ is the sheet resistance between the contacts i and j for a current flowing from i to j, and the potential difference is measured between the contacts p and q (see Fig. 4.6).

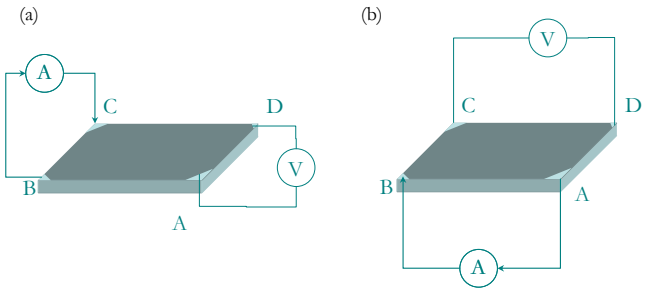

Fig. 4.6. Van der Pauw configuration for measuring (a) V_{DA} and (b) V_{DC}.

In the case of diluted magnetic semiconductors, the van der Pauw technique allows to check how the magnetic properties of the material influence its electric properties. For instance, up to what extent does an applied magnetic field change the materials resistance (magnetoresistance, MR), or if one can observe an anomalous Hall effect (AHE) which arises due to peculiar spin scattering mechanisms.

The Hall resistivity is known to be a sum of ordinary and anomalous Hall terms, $\varrho = R_H B + R_S \mu_0 M$ where R_H is the ordinary Hall coefficient, and R_S is the anomalous Hall coefficient. The first term describes the ordinary Hall effect, linear in B, and the second term represents the AHE proportional to the magnetization M [Higgins (2004)]. The anomalous Hall term is usually attributed to asymmetric scattering processes involving the spin-orbit interaction between the conduction electrons and the magnetic moments in the material.

In the presence of a magnetic field, the conductivity usually decreases, because the path length between the contacts gets larger. Hence, the charge carriers suffer more collisions than for $B = 0$. These longer paths lead to increased resistance. This change of electrical resistance produced in metals or semiconductors upon application of a magnetic field B is dubbed MR which is usually characterized by the non-dimensional parameter:

$$MR = \frac{R(B) - R(0)}{R(0)} \times 100\%, \tag{4.10}$$

where $R(0)$ is the resistance at zero field, and $R(B)$ is the resistance at the applied magnetic field B. For low applied magnetic fields, the field dependence of a semiconductor MR can be described by:

$$R(B) = R_0 + aB^2, \tag{4.11}$$

where a is a constant. At high fields, the MR can rise faster than B^2, increase linearly with B, or tend to a constant (*i.e.* saturate), depending on the material.

Negative MR occurs when the magnetic disorder and the corresponding scattering are reduced due to the magnetic field induced spin alignment. When electron interference takes place, a correction to the conductivity associated to the negative MR is necessary. This is due to the so-called weak localization regime, and the conductivity is enhanced due to constructive quantum interference.

4.5 X-RAY DIFFRACTION

In 1913, the physicists Sir W.H. Bragg and Sir W.L. Bragg[17] developed a relationship that expresses mathematically the diffraction pattern produced by an incident X-ray beam on a crystal:

[17] The discovery of X-ray diffraction was made simultaneously by the Braggs and by M. von Laue.

$$2d_{hkl}\sin\theta = n\lambda\,, \tag{4.12}$$

where θ is the incident angle, d_{hkl} is the distance between atomic layers in a crystal, λ is the wavelength of the incident X-ray beam, and n is an integer. As illustrated in Fig. 4.7, this observation is based on constructive interference of monochromatic X-rays, commonly denoted as X-ray diffraction. Note that the possible d-spacings are determined by the shape and size of the unit cell. Therefore the possible 2θ values at which one can observe reflections are determined by the unit cell dimensions. On the other hand, the intensities of the reflections are determined by the distribution of the electrons in the unit cell. The highest electron density is found around atoms, and the intensities depend on what kinds of atoms are present and where they are located in the unit cell.

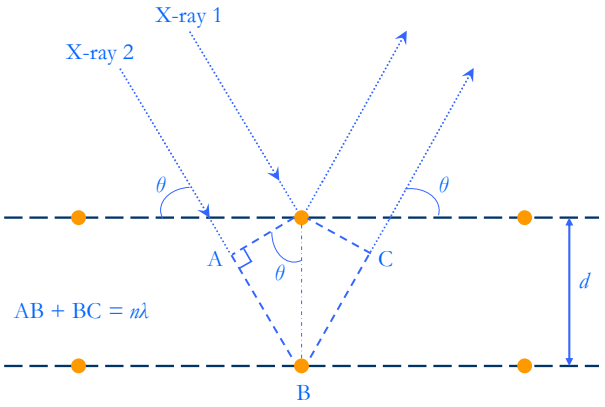

Fig. 4.7. Schematic representation of Bragg's law for an X-ray diffraction pattern of a crystal.

As it is know from standard solid state physics text books [*e.g.* Kittel (1996)], for orthorhombic lattices there is the following relation between the spacing of lattice planes d_{hkl} and the Miller indices h, k and l associated with this family of planes:

$$\left(\frac{1}{d_{hkl}}\right)^2 = \left(\frac{h}{a_1}\right)^2 + \left(\frac{k}{a_2}\right)^2 + \left(\frac{l}{a_3}\right)^2\,, \tag{4.13}$$

Usually, in crystals that exhibit sixfold symmetry, such as ZnO, four axes of reference are used (Fig. 4.8). Three of them lie in a plane at 120° to one another (a_1, a_2, a_3) and the forth axis c is perpendicular to the plane spanned by the others. As a consequence, in hexagonal crystal systems four so-called Miller-Bravais indices h, k, i and l, are used. However, i depends of h and k:

$$i = -(h + k), \tag{4.14}$$

hence, in this notation, d_{hkl} is given by [Vainshtein (1994)]:

$$\frac{1}{d_{hkl}^2} = \frac{4}{3a^2}\left(h^2 + k^2 + hk\right) + \frac{l^2}{c^2}, \tag{4.15}$$

where $a = a_i$ and c are the lattice parameters of the hexagonal crystal.

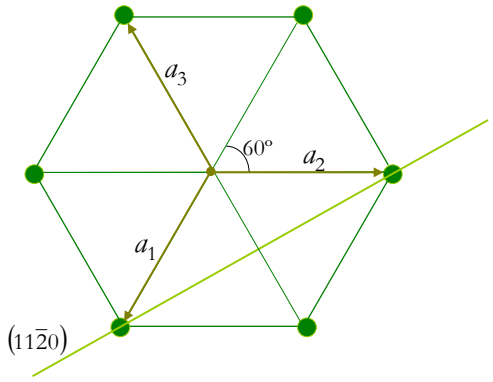

Fig. 4.8. Hexagonal lattices are described by four principle vectors. The forth axis stands perpendicular to the plane spanned by (a_1, a_2, a_3).

XRD is most widely used for characterization of crystalline materials, determination of unit cell dimensions, measurement of sample purity, determining lattice mismatch between film and substrate, determining the orientation of a single crystal or grain, finding the crystal structure of an unknown material, and measuring the size, shape and internal stress of small crystalline regions.

The spectral line width of the XRD pattern also gives valuable information about the samples. The line broadening can be produced by instrumental effects, by the small crystallite dimensions, and by lattice distortions. The instrumental contribution is relatively small and can be estimated by using a calibration sample. The crystallite dimension is related to the regions in which the diffraction is coherent, and, after removing the instrumental contributions, may be estimated using the Scherrer equation [Klug and Alexander (1974)]:

$$D_v = \frac{K\lambda}{\delta \cos\theta}, \tag{4.16}$$

where D_v is the volume weighted crystallite size, K is the Scherrer constant, and δ is the full width at half maximum (FWHM) of the XRD peak located at angle θ. However, this approach neglects the effect that the strain can have on the crystallite size. Williamson and Hall (1953)

proposed a simplified method of interpreting the line broadening in terms of lattice strain and crystallite size, which is expressed by:

$$\frac{\delta \cos\theta}{\lambda} = \frac{1}{\varepsilon} + \frac{\zeta \sin\theta}{\lambda}, \tag{4.17}$$

where ε and ζ and are the effective particle size and the effective strain, respectively. The effective particle size taking strain into account is estimated by plotting $\delta \cos\theta / \lambda$ vs. $\sin\theta/\lambda$.

X-ray diffractometers consist of four basic elements: an X-ray tube, a sample holder, a monochromator, and an X-ray detector. X-rays are emitted by a cathode ray tube. Electrons are produced by heating a filament, and then are accelerated toward a target by applying a voltage, and bombard the target material. When the electrons have sufficient energy to remove inner shell electrons of the target material, characteristic X-ray spectra are produced. These spectra consist of several components, the most common are K_α and K_β, and the specific wavelengths are characteristic of the target material (Cu, Fe, Mo, or Cr). Filtering, with foils or crystal monochromators, produces the monochromatic X-rays needed for diffraction, which are then collimated and directed onto the sample. As the sample and detector are rotated, the intensity of the reflected X-rays is recorded.

In this work, the XRD measurements were collected on a commercial PanAnalytical X'pert MPD diffractometer, equipped with a curved graphite monochromator and the X'Celerator detector, using Cu $K_{\alpha 1,2}$ radiation ($\lambda K_{\alpha 1}$=1.54060 Å, $\lambda K_{\alpha 2}$=1.54443 Å with $I(K_{\alpha 2})/I(K_{\alpha 1})$=1/2). The XRD scans were performed in the conventional θ-2θ reflection geometry, at room temperature. In order to correct for any errors that may arise due to sample height displacement, instrumental zero offset, sample transparency, we have used a certified standard NIST SRM660a (LaB_6 powder). Besides allowing to obtain accurate peak positions, the LaB_6 certified powder was also used as a line profile standard to determine the instrumental broadening as a function of the diffracting angle.

4.6 Scanning electron microscopy

The technology used in the SEM is based on television techniques. This method is suitable for collecting images of samples with conductive surfaces. The surface of the object is scanned with a focused electron beam point by point. The interactions of the electron beam with atoms at or

near the surface of the sample generate signals that give information about the sample's topography, chemical composition, crystalline structure and orientation. Generally, a 2-dimensional image is generated over a selected area of the surface of the sample. This technique is normally used to generate high-resolution images of shapes of objects, revealing details of about 1 to 5 nm in size, and to show spatial variations in chemical compositions.

In a typical SEM, an electron beam is emitted from a cathode. The electron beam is accelerated by an applied voltage and reaches energies ranging from a few hundred eV to 40 keV. This beam is then focused by one or two condenser lenses to a spot of about 0.4 nm to 5 nm in diameter. The beam passes through pairs of deflector plates, which deflect the beam in the *x* and *y* axes so that it scans over a rectangular area of the sample surface. When the incident electrons interact with the sample, the electron kinetic energy is dissipated producing a variety of signals. These signals include secondary electrons, backscattered electrons (BSE), diffracted backscattered electrons (that are used to determine crystal structures and orientations), electromagnetic radiation (characteristic X-rays that are used for elemental analysis), visible light (cathodoluminescence, CL), heat, and transmitted electrons. Each one of these signals may be used to form an image; as long as there exists an appropriate detector to convert the observed effect into an electric signal. Usually these specialized detectors are not all present on a single machine. Secondary electrons and backscattered electrons are commonly used for imaging samples. The first ones are most valuable for showing morphology and topography of the samples, while the second ones are most valuable for illustrating contrasts in composition in multiphase samples. Electronic amplifiers of various types are used to amplify the signals which are displayed as variations in brightness on a cathode ray tube. The beam current absorbed by the sample can also be detected and used to create images of the distribution of the sample current. The scanning of the display is synchronized with that of the beam on the sample in the microscope. The resulting image is thus a map of the intensity distribution of the signal being emitted from the scanned area of the sample. The image is digitally captured and displayed on a computer. A basic diagram of a typical SEM instrument is shown in Fig. 4.9.

In this work, the scanning electron microscopy (SEM) measurements were performed with a CamScan CS 44 Microscope using 10 keV electrons.

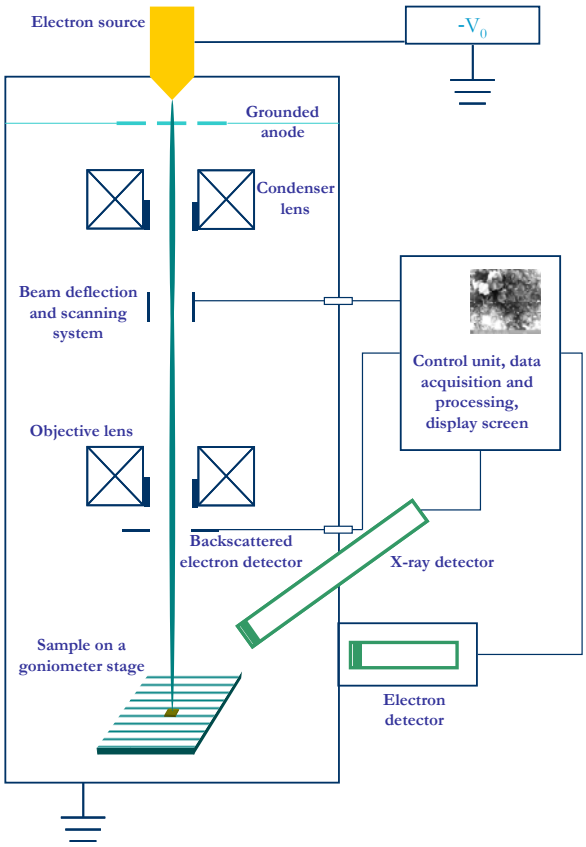

Fig. 4.9. Basic diagram of a scanning electron microscope.

4.7 TRANSMISSION ELECTRON MICROSCOPY

While SEM produces images essentially similarly to a television, by the scanning principle, the image produced by TEM is formed by lenses, and the sample is observed in transmission mode. The TEM performance depends on the possibility of preparing a sufficiently thin sample to transmit the electron beam without significant energy losses. The image formation is thus intimately connected with diffraction, because when going through the sample, the electron waves interact with the sample and suffer phase and amplitude variations. These variations produce the image contrast. If one knows how the different structures change the transmitted electron waves, one can obtain information about the sample's microstructure. The main advantage of TEM is its resolution, due to the small wave length of the electrons. A typical TEM system is schematically represented in Fig. 4.10.

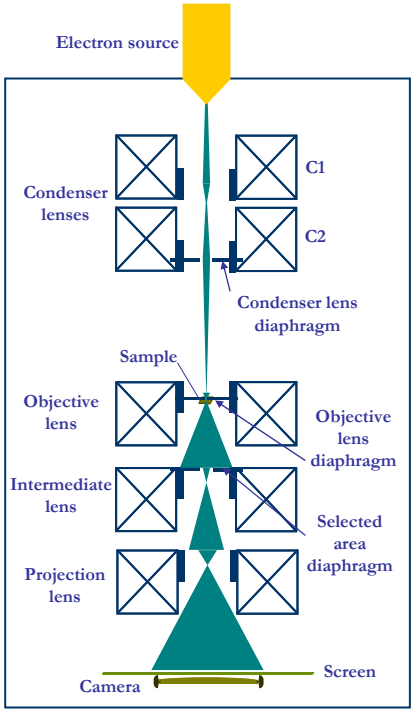

Fig. 4.10. Basic diagram of a transmission electron microscope.

The electron beam is produced by a cathode. The electrons are accelerated by a high voltage. Usually, the accelerated electrons may have energies in the range of 10 to 300 keV. The higher the acceleration voltage, the shorter are the electron waves and the higher is the resolution power. Nevertheless, this factor is hardly ever limiting. The resolution of the electron microscopy is usually limited by the aberrations of the lens systems, and particularly by the sample preparation technique. Modern systems have powers of resolution down to 0.5 Å. The lens systems consist of electric coils generating a magnetic field. The beam is first focused by a pair of condenser lenses (C1 and C2). The first lens is strong, and originates a very small image of the source, which is projected by the second lens that is much weaker onto the sample surface. This second lens is equipped with a diaphragm that controls the beam intensity. The beam then passes through the sample, where it is partially deflected. The degree of deflection depends on the electron density of the sample. The greater the mass of the atoms, the greater is the degree of deflection. After passing through the sample, the scattered electrons are collected by an objective which has a short focal distance. Thereby an image is formed that is subsequently enlarged by an additional lens system, composed by two lenses, the intermediate one and the projection one. Consequently, the formed image is projected on a fluorescent

screen. Alternatively, it can be documented on a photographic material. Photos taken with electron microscopes are always black and white. The degree of darkness corresponds to the electron density of the sample.

Ideally, it should be possible to interpret a TEM image in terms of the samples' microstructure. However, the image contrast can arise due to several mechanisms, and can depend crucially on the microscope working conditions, such as the exact sample orientation and the defocusing of the objective lens. Furthermore, the electrons may be dispersed elastically or inelastically. These dispersion mechanisms also influence the image contrast in different ways. Due to the large mass difference between electrons and ions, the energy of the elastically dispersed electrons is approximately the same as the energy of the incident ones. The purely elastic dispersion produces a perfect punctual correlation between the object and the image. On the other hand, the inelastically dispersed electrons suffer energy losses, and consequently are not focused on the theoretical image plane (due to their large dispersion angle), which generates a reduction in the image's clearness and contrast.

The opening of the objective lens is limited by a circular diaphragm placed in the posterior focal plane. Only the electrons dispersed within a certain angle pass through the aperture. The result is a uniform intensity in the image plane, with the exception of the image of a dispersing element (the image of this kind of element appears dark on a bright background).

It is also important to note that the sample preparation is quite tricky. The samples must be very thin, in order to be able to transmit the radiation, and proper to place in vacuum. Additionally, one must not disregard the fact that the samples are irradiated with an electron beam, and that there is no guarantee that there will be no changes due to this interaction.

5 ZnO TRANSITION METAL DOPED NANOWIRES

This chapter is dedicated to a detailed study of the incorporation of Mn or Co into the lattice of ZnO nanowires (NWs) synthesized on *a*-plane sapphire substrates by high-pressure pulsed laser deposition (PLD). The samples were characterized by scanning electron microscopy (SEM) and electron paramagnetic resonance (EPR) in the X-band (≈9.3 GHz) from T = 4 to 300 K. The results presented in this chapter were published in the following papers: (i) AIP Conf. Proc., **893**, 63 (2007); (ii) Journal of Applied Physics **101**, 024324 (2007); (iii) Physica Status Solidi (b), **246**, 766 (2009).

5.1 SAMPLE GROWTH AND STRUCTURAL CHARACTERIZATION

The ZnO NWs were synthesized on 10 × 10 mm^2 *a*-plane sapphire substrates by high-pressure PLD with a KrF excimer laser [Lorenz (2005), Rahm (2006)]. A gold catalyst was applied prior to deposition in order to achieve the vapour–liquid–solid growth of ZnO nanowires. The growth temperature varied between 780 and 880ºC. The different rotating ZnO targets of the three NWs samples were prepared from 5N powders, pressed and sintered for 12 hours at 1150ºC in air, nominally containing 3 at. % Mn, 10 at% Mn or 5 at. % Co. Argon was used as a carrier gas at a background pressure of 100 mbar and a constant flow rate of 100 sccm. The target-to-substrate distance was varied between 10 and 20 mm, and 4800 - 12000 pulses were used to ablate the targets with a laser energy density of about 2 $J.cm^{-2}$.

Elemental analysis using particle induced X-ray emission (PIXE) and Rutherford Backscattering (RBS) of the NW samples grown from the 3 at. % Mn, and 5 at. % Co PLD targets was carried out by Rahm *et al.* (2006). For the first sample, the Mn content was more inhomogeneous varying between 0.20 and 0.75 at. %, while for the second sample, the Co content measured at 7 different spots varied between 0.15 and 0.3 at. %. In both cases, the measurements indicate that the doping content in the nanowires is much lower than that expected from the targets compositions.

The morphology of the samples was characterized by SEM measurements, performed with a CamScan CS 44 Microscope using 10-keV electrons. Typical SEM pictures of the studied NWs are given in Fig. 5.1, evidencing the good quality and the alignment of the NWs perpendicular to the substrate surface. The NWs are about 1 μm long and exhibit diameters

ranging from 60 nm to 150 nm. The structures have a hexagonal cross-section, mimicking the hexagonal crystal structure of ZnO.

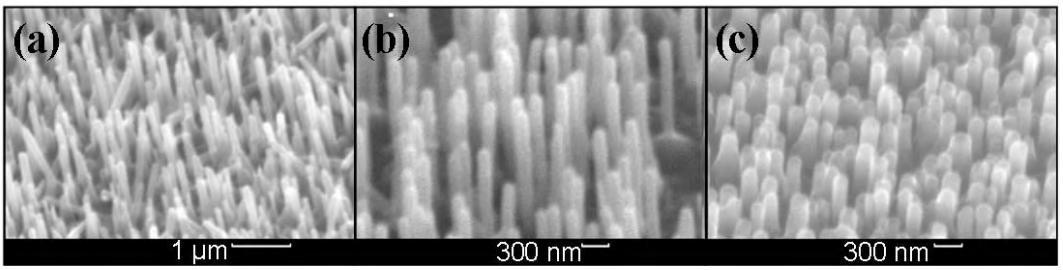

Fig. 5.1. Typical SEM images of ZnO: 5 at. % Co (a); ZnO: 3 at. % Mn (b) and ZnO: 10 at. % Mn. All pictures were taken under a 45º viewing angle.

5.2 ELECTRON PARAMAGNETIC RESONANCE STUDY

ZnO crystallizes in the wurtzite structure $P6_3mc$ with a C_{3v} point symmetry for the substitutional sites. Each metallic ion is surrounded by an almost perfect tetrahedral arrangement of O^{2-} ions. The crystal field (CF) experienced by the Zn ion has a dominant cubic component and a weaker trigonal one. As for all 3*d* transition metal (TM) ions, Co and Mn are expected to substitute Zn atoms. In their neutral charge state (as referred to the charge state of the Zn ion), the ions have $3d^7$ and $3d^5$ electron valence configurations, yielding ${}^4A_2$ and ${}^6A_1$ ground states for the free ions, respectively. Furthermore, as the ionic radii of the substitutional TM ions are obviously different from the Zn ionic radius, it is reasonable to consider that there will exist a local distortion of the lattice structure, which will be a trigonal distortion, as the doping with TM ions changes the distance between the central ion and the surrounding oxygen ions along the C_3 axis. Ju-Fen *et al.* (2006) showed that for substitutional Fe^{3+} is ZnO, for which the ionic radius (0.64 Å) is inferior to that of Zn^{2+} (0.74 Å), a compression is observed along the hexagonal *c*-axis. In this sense, as both ionic radius of Co^{2+} (0.79 Å) and Mn^{2+} (0.80 Å) are larger than that of the Zn^{2+} ion, one should expect elongation along the hexagonal *c*-axis.

5.2.1 Mn Incorporation

The experimental angular dependencies of the EPR spectra of the Mn doped ZnO NWs samples is given in Figs. 5.2 and 5.3.

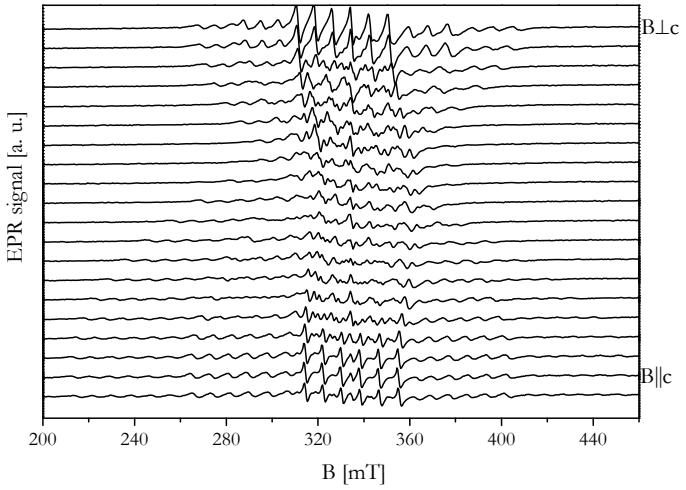

Fig. 5.2. Experimental angular dependence of the EPR spectra of Mn^{2+} in ZnO nanowires (nominal content of 3 at. %), measured in the X-band at 4.2 K.

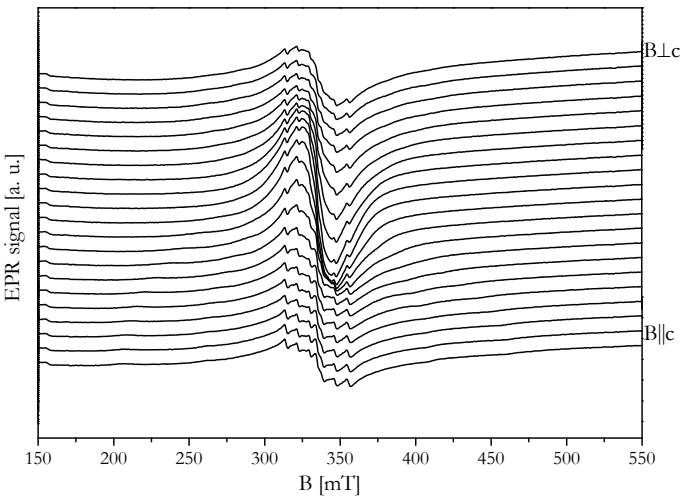

Fig. 5.3. Experimental angular dependence of the EPR spectra of Mn^{2+} in ZnO nanowires (nominal content of 10 at. %), measured in the X-band at 4.2 K.

In the case of manganese, the trigonal component of the CF and the spin-orbit interaction split the $S = 5/2$, ${}^6A_1$ ground state into three Kramers doublets $E_{\pm 1/2}$, $E_{\pm 3/2}$, and $E_{\pm 5/2}$ with zero-field splittings (ZFSs) equal to $2D$ and $4D$, respectively. The spin Hamiltonian (SH) for $S = 5/2$ and $I = 5/2$ is given by [Kreissl (1990)]:

$$\mathscr{H} = \beta \mathbf{B}\cdot\mathbf{g}\cdot\mathbf{S} + \mathbf{S}\cdot\mathbf{A}\cdot\mathbf{I} + D\left[S_Z^2 - \frac{35}{12}\right] - \frac{(a-F)}{180}\left[35S_Z^4 - \frac{475}{2}S_Z^2 + \frac{2835}{16}\right] + \frac{a\sqrt{2}}{36}\left[S_Z\left(S_+^3 - S_-^3\right) + \left(S_+^3 - S_-^3\right)S_Z\right] \tag{5.1}$$

with $S_\pm = S_X \pm S_Y$, where D and F are the axial fine structure (FS) parameters given by the spin operators in second and fourth order, respectively, and a is the cubic FS parameter. The crystal c-axis (cubic [111] axis) was chosen as the quantization axis Z, with X and Y being, in cubic notation, the $[11\bar{2}]$ and $[\bar{1}10]$ axes, respectively.

The following energy eigenvalues for $B \parallel c$ may be inferred from the SH given by Eq. (5.1) [Schneider (1962, 1963)]:

$$\begin{aligned} W_{\pm 5/2} &= \pm g\beta B_0 + \frac{D}{3} - \frac{(a-F)}{2} \pm \sqrt{\left[3D + \frac{(a-F)}{6} \pm \frac{3}{2}g\beta B_0\right]^2 + \frac{20}{9}a^2}, \\ W_{\pm 3/2} &= \pm\frac{3}{2}g\beta B_0 - 2\frac{D}{3} + (a-F), \\ W_{\pm 1/2} &= \mp g\beta B_0 + \frac{D}{3} - \frac{(a-F)}{2} \pm \sqrt{\left[3D + \frac{(a-F)}{6} \mp \frac{3}{2}g\beta B_0\right]^2 + \frac{20}{9}a^2}. \end{aligned} \tag{5.2}$$

As the parameter a is small when compared to the Zeeman energy and to D, the terms proportional to $20a^2/9$ can be neglected in a good approximation, and the line positions for the FS transitions are therefore given by:

$$\begin{aligned} B_{+5/2\leftrightarrow+3/2} &= B_0 - 4D' + \frac{4}{3}(a'-F') \\ B_{+3/2\leftrightarrow+1/2} &= B_0 - 2D' - \frac{5}{3}(a'-F') \\ B_{+1/2\leftrightarrow-1/2} &= B_0 \\ B_{-1/2\leftrightarrow-3/2} &= B_0 + 2D' + \frac{5}{3}(a'-F') \\ B_{-3/2\leftrightarrow-5/2} &= B_0 + 4D' - \frac{4}{3}(a'-F') \end{aligned} , \tag{5.3}$$

with $B_0 = h\nu/(\beta g)$. The prime indicates that the values are in magnetic field units (mT).

As presented in Table 5.1, the SH parameters for substitutional Mn^{2+} in ZnO do not vary significantly with temperature. Hence, Fig. 5.4 illustrates the expected line positions and the corresponding transitions in the energy level diagram which was calculated with the EasySpin software package [Stoll (2006)] for $B \parallel c$ at 300 K, using the SH parameters obtained by

Schneider *et al* (1962, 1963). In this diagram, one can clearly observe the Zeeman splitting, the fine and the hyperfine (HF) structures. Note that, because in this case the sign of D is negative, the set of allowed transitions (in red) observed at the lowest field corresponds to the set of transitions $|-5/2\rangle \leftrightarrow |-3/2\rangle$.

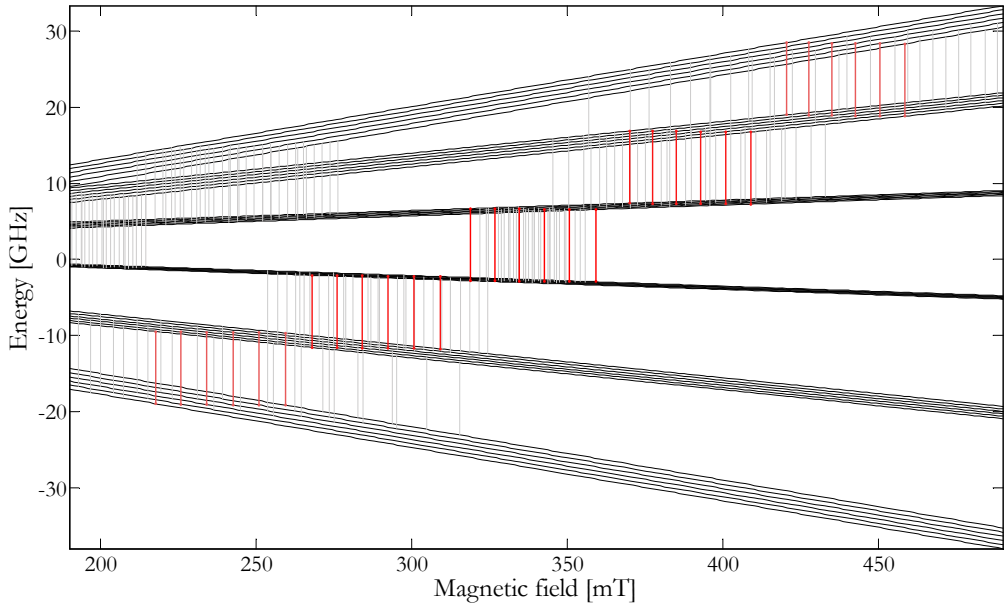

Fig. 5.4. Diagram of the energy levels for the EPR (X-band) transitions of substitutional Mn^{2+} in ZnO. The energy levels were calculated using the spin Hamiltonian parameters obtained by Schneider *et al.* (1962, 1963) for 300 K. The transitions represented by red lines correspond to the allowed ones, while the gray lines correspond to the "forbidden" ones.

By fitting the experimental spectra with the Minirock program [Denninger (2006)], we extracted the line positions for $B \parallel c$ ($\theta = 0°$). This way we have determined $g_{\parallel}$, $A_{\parallel}$, D and $|a\text{-}F|$ is given in Table 5.1. The SH parameters values are very close to the ones observed for Mn doped single crystals [Schneider (1962, 1963)], and do not vary significantly with the Mn content, in the studied Mn concentration range, as observed also by Diaconu *et al.* (2005b) in Mn doped ZnO thin films.

Additionally, as can be observed in Fig. 5.5, with increasing Mn content the line width increases due to the dipole-dipole interaction of the paramagnetic ions. Moreover, for the highest nominal concentration, x_{Mn} = 10 at.%, a superimposed unresolved broad line appears, indicating an inhomogeneous distribution of Mn, in other words, there are regions with lower

Mn concentrations (resolved spectrum), and regions with a higher concentration of Mn (unresolved spectrum), where the HF structure of the spectra is obscured by the dipole-dipole broadening and breaks down due to the exchange interaction.

Table 5.1. SH parameters for the EPR spectra of Mn^{2+} in ZnO nanowires, measured at 4.2 K. Except for g, all values are given in 10^{-4} cm^{-1}.

X	3 at. %	10 at. %	Schneider (1962, 1963) (77 K)	Schneider (1962, 1963) (300 K)	Hausmann and Huppertz (1968) (295 K)
$\lvert A_{\parallel}\rvert$	76 ± 1	78 ± 3	74.96 ± 0.05	74.10 ± 0.05	73.93 ± 0.02
$g_{\parallel}$	2.003 ± 0.001	2.000 ± 0.002	2.0014 ± 0.0002	2.0012 ± 0.0002	1.9984 ± 0.0002
D	-231 ± 0.1	-230 ± 3	-231.6 ± 0.4	-236.2 ± 0.4	-235.28 ± 0.04
$\lvert a\text{-}F\rvert$	6 ± 1	7 ± 3	5.26 ± 0.05	5.23 ± 0.05	5.44 ± 0.04

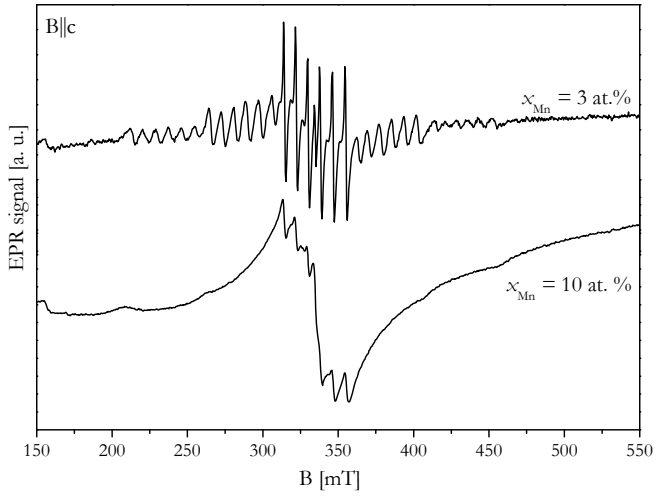

Fig. 5.5. Experimental EPR spectra for $B \parallel c$ of Mn^{2+} in ZnO nanowires with two different nominal Mn contents (3 and 10 at. %), measured in the X-band at 4.2 K.

5.2.2 Co Incorporation

In the case of substitutional Co^{2+} ($3d^7$) state on the Zn sites the atomic ^4F ground state splits under the influence of the tetrahedral component of the CF into a $^4A_2$ orbital singlet state and two orbital triplets, $^4T_2$ and $^4T_1$. The first excited state $^4T_2$ is separated from the lowest level by the amount $10Dq \approx 4000$ cm^{-1} [Koidl (1977)]. The value of $10Dq$ is much larger than the thermal energy at room temperature; hence the occupations of all excited states are much smaller than those of the ground-state levels. The EPR signal is therefore determined almost

entirely by the properties of the singlet ground state $^4A_2$, with only a small admixture from the higher lying excited states. Under the action of the trigonal component of the CF and the spin-orbit coupling both triplets and the singlet undergo further splitting. The fourfold degenerated ($S = 3/2$) $^4A_2$ ground state divides into two Kramers doublets $E_{\pm 1/2}$ and $E_{\pm 3/2}$ with a ZFS equal to $2D$, where the doublet $E_{\pm 1/2}$ ($S = \pm 1/2$) is the lowest, in agreement with the optical [Koidl (1977)] and EPR results [Estle and De Wit (1961)]. Taking into account these results, the EPR data can be described by the following SH [Abragam and Bleany (1986)]:

$$\begin{aligned}\mathscr{H} &= \beta B\left(g_{\parallel}\ \cos\theta S_Z + g_{\perp}\sin\theta S_X\right) \\ &+ A_{\parallel}\ S_Z I_Z + A_{\perp}\left(S_X I_X + S_Y I_Y\right) + D\left[S_Z^2 - \frac{1}{3}S(S+1)\right],\end{aligned} \tag{5.4}$$

once again, the label Z (or $\parallel$) applies for the c-axis (hexagonal [0001] axis of ZnO) and X, Y (or $\perp$) apply for all axes perpendicular to it. In the present case, $I = 7/2$. As in this case the ZFS is much larger than the Zeeman energy, only the electron spin transitions $M_S = \left|\pm 1/2\right\rangle$ within the $S = 3/2$ manifold can be observed in the available magnetic fields up to 1.5 T. The corresponding spectrum can therefore be described in good approach by the effective SH given by:

$$\mathscr{H} = \beta \mathbf{B}\cdot\mathbf{g}'\cdot\mathbf{S}' + \mathbf{S}'\cdot\mathbf{A}'\cdot\mathbf{I}, \tag{5.5}$$

with an effective spin $S' = 1/2$ and taking into account the HF interaction in the doublet. In this approach, the angular dependence of the line positions B_M of the allowed HF transitions ($\Delta m_I = 0$) within the $\left|\pm 1/2\right\rangle$ spin doublet is given by the resonance condition

$$h\nu = \beta g'(\theta) B_M(\theta) + A'(\theta) m_I, \tag{5.6}$$

where θ is the angle between the c-axis and the applied external magnetic field B. The effective g-value $g'(\theta)$ is related with the g-values used in equation (5.4) in the $S = 3/2$ manifold in first order by [Kreissl (1990)]:

$$g'(\theta) = \sqrt{g_{\parallel}^2\ \cos^2(\theta) + (2g_{\perp})^2 \sin^2(\theta)}, \tag{5.7}$$

and the apparent HF constant $A'(\theta)$ by

$$A'(\theta) = \frac{\sqrt{g_{\parallel}^2 A_{\parallel}^2\ \cos^2(\theta) + 16 g_{\perp}^2 A_{\perp}^2 \sin^2(\theta)}}{g'(\theta)}. \tag{5.8}$$

Hence, for $B \parallel c$ ($\theta = 0°$) the apparent g and A values g' and A' are equal to $g_\parallel$ and $A_\parallel$, respectively, while for $B \perp$ c ($\theta = 90°$) one obtains:

$$g' = 2g_\perp \text{ and } A'_\perp = 2A_\perp. \tag{5.9}$$

Whereas for $\theta = 0°$ the parameters g' and A' are identical to the corresponding g- and A-values, the exact diagonalization of the SH (Eq. (5.4)) gives very small corrections for $\theta \neq 0°$. These small contributions are given in good approach by the perturbation theory using the correction up to the third order in the Zeeman energy [Kreissl (1990)]. In the case of $B \perp$ c ($\theta = 90°$), the corrected value is given by $g'_\perp = 2g_\perp\left[1-(3/16)(g_\perp\mu_B B/D)^2\right]$, which raises the $g_\perp$-value calculated with Eq. (5.7) only by 2.2×10^{-3} using the D-value of 2.75 cm^{-1} given by Estle *et al.* (1961). The SH parameters for the experimental spectra were obtained (see Table 5.2) by fitting the experimental spectra with the Minirock program [Denninger (2006)]. The analysis of the spectrum revealed that it consists of two components, A and B, as illustrated in Fig. 5.6 for $B \parallel c$.

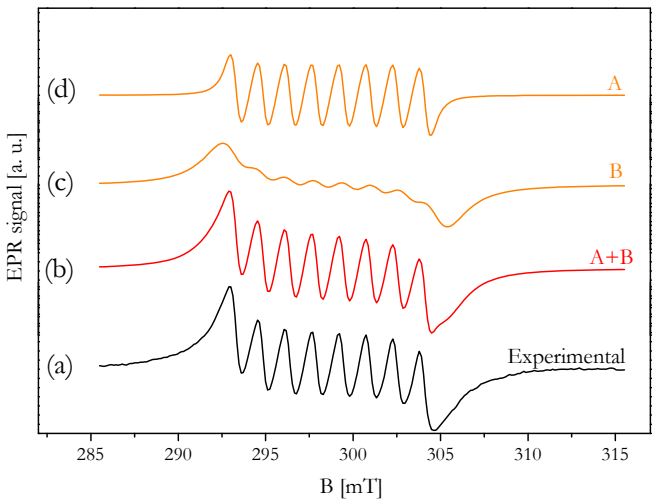

Fig. 5.6. (a) Experimental EPR spectrum of Co^{2+} in ZnO nanowires (nominal content of 5 at. %), measured in the X-band at 4.2 K for $B \parallel c$ ($\theta = 0°$); (b) result of the fitting of the experimental spectrum given by the sum of components A and B shown in (c) and (d), respectively.

These components follow the same angular and temperature dependencies. Using the intensity ratio between the two components, the ratio of the number of centres was determined $N_B/N_A = 1.4$. The calculated angular dependence of the experimental Co^{2+} EPR spectrum

together with the HF splitting using parameters given in Table 5.2 is shown in Fig. 5.7. In Fig. 5.8 the angular dependencies of the experimental line positions for both components A and B are compared with the calculated ones using Eq. (5.7) supplemented with the small third order corrections in the Zeeman energy [Kreissl (1990)].

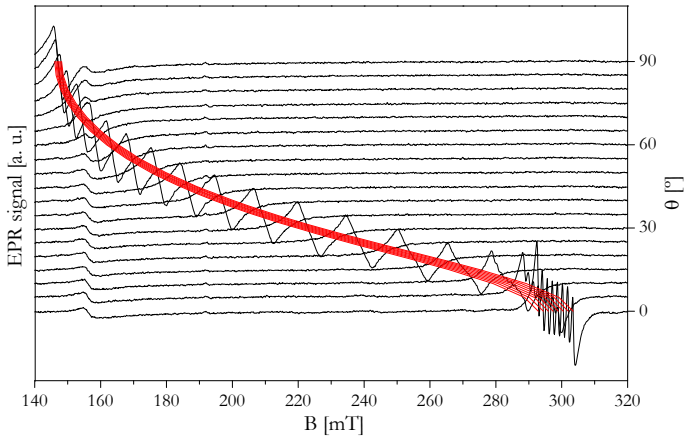

Fig. 5.7. Angular dependence of the EPR spectra of Co^{2+} in ZnO nanowires (nominal content of 5 at. %), measured in the X-band at 4.2 K. $\theta = 0°$ corresponds to $B \parallel c$. The result of the fitting of the angular dependence of the HF line positions is plotted in solid lines on top of the spectra.

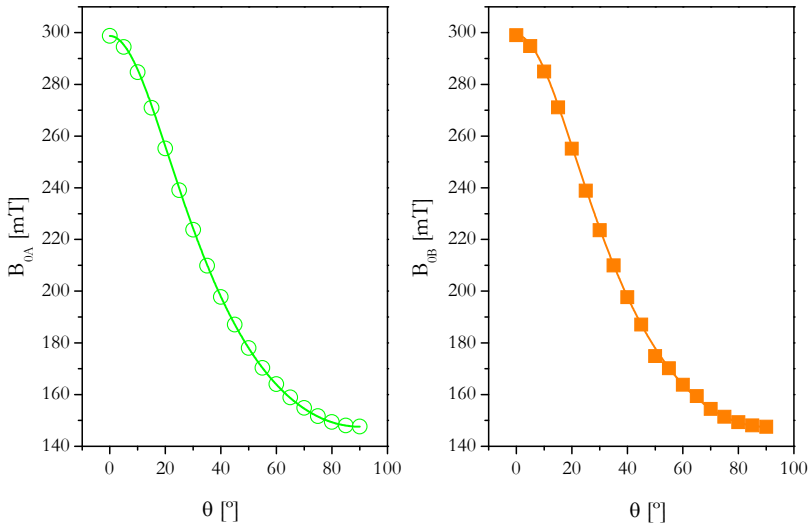

Fig. 5.8. Experimental values of the centres of gravity of the A (dots) and B (squares) EPR spectra, as extracted from the fittings, and calculated (solid lines) angular variations of the line positions of the $|\pm 1/2\rangle$ transitions for Co^{2+} in ZnO nanowires (nominal content of 5 at. %). The spectra were measured in the X-band at 4.2 K.

Table 5.2. SH parameters determined for the EPR spectrum measured at 4.2 K of Co^{2+} in ZnO nanowires nominally doped wit 5 at. % Co. Except for g, all values are given in 10^{-4} cm^{-1}.

signal	A	B	Estle and De Wit (1961)
$\|A_{\parallel}\|$	16.2 ± 0.6	16.8 ± 2.0	16.11 ± 0.05
$\|2A_{\perp}\|$	3.2 ± 1.0	3.2 ± 1.0	3.00 ± 0.03
$g_{\parallel}$	2.247 ± 0.001	2.245 ± 0.002	2.243 ± 0.001
$g_{\perp}$	2.276 ± 0.001	2.276 ± 0.007	2.2791 ± 0.002
D	-	-	2.75 ± 0.01

The line widths (for $B \parallel c$, $\Delta B_{pp} = 0.7$ and 1.9 mT for components A and B, respectively) were larger than that reported in the literature for epitaxial layers ($\Delta B_{pp} = 0.04$ mT for $B \parallel c$) [Jedrecy (2004)]. The observed broadening may be in part due to the presence of a high defect concentration and random strains in the NWs. However, the main part is probably caused by some irregularity of the NWs arrangement observed by SEM. All determined SH parameters, except $g_{\parallel}$, fairly agree with those reported in the literature for bulk crystals and epitaxial layers [Estle and De Wit (1961), Jedrecy (2004)]. The $g_{\parallel}$ values are slightly too large, lowering the line position by about 0.6 mT for component A. This suggests that the sample was slightly misoriented during the measurement, and that in this case we did not measure exactly the values for $B \parallel c$. Using the data from literature [Estle and De Wit (1961)] one finds that a misalignment of only ≈ 2.0º can be responsible for this deviation. Thus, the misalignment probably comes from the misorientation of the sample holder's surface in the cavity.

Additional information about the magnetic state of the NWs can be obtained from the variation of the EPR spectrum intensity I with the measurement temperature T. In the case of cations without exchange interaction, I is proportional to the difference in the population of the four lowest levels, whose energies can be calculated using the SH given by Eq. (5.4). In Fig. 5.9 we show the experimental temperature dependence between 5 and 40 K of the EPR spectrum for $B \parallel c$, which was the best resolved one. Although the spectrum could be detected up to 90 K, for $T > 40$ K the HF structure could not be resolved. In Fig. 5.10 we illustrate the EPR intensity and inverse intensity temperature dependences for both components of the spectra A and B,

together with the respective calculated curves of the temperature dependence for the $|\pm 1/2\rangle$ transition within the $S = 3/2$ manifold (using $D = 2.75$ cm^{-1} given by Estle and De Wit (1961).

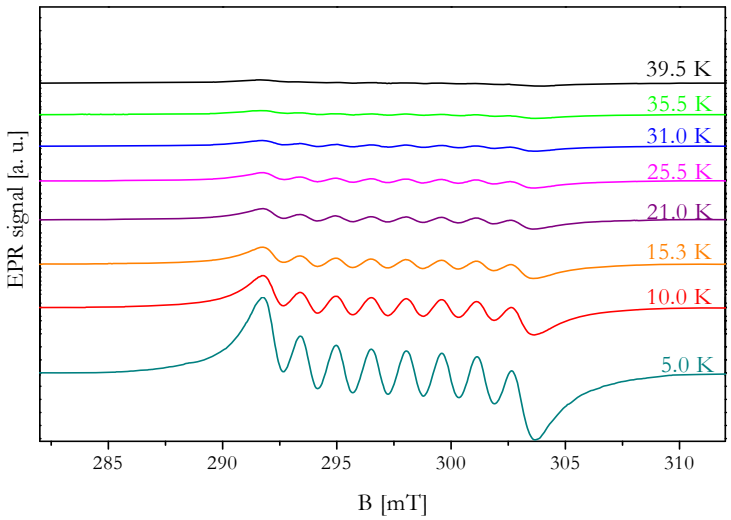

Fig. 5.9. Experimental temperature dependence of the EPR spectra for the Co^{2+} in ZnO nanowires (nominal content of 5 at. %), measured for $B \parallel c$ in the X-band.

This plot evidences that both components exhibit a paramagnetic behaviour. Moreover, in the same figure, we plot a simulation including a correction that takes into account a possible small intensity error linearly dependent on the temperature, and the simulation now perfectly agrees with the experimental data. This error might be caused by any of the following factors or a combination of them: (i) miscalibration of the thermoelement, (ii) variation of the quality factor of the microwave cavity with temperature, (iii) setting in of a saturation of the EPR transition with decreasing temperature due to increasing spin-lattice relaxation time (see below the discussion of the temperature behaviour of the line width). Because the correction necessary to perfectly fit the measured values is very small, none of the above reasons can be excluded. On the other hand, such small effects are difficult to be checked with certainty.

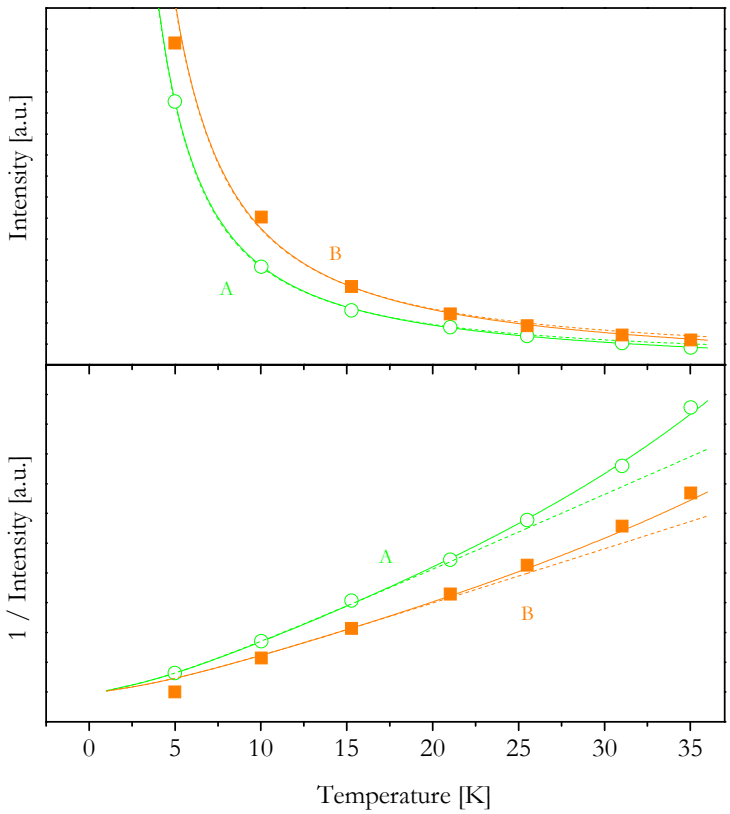

Fig. 5.10. Temperature dependence of the EPR intensity (top) and inverse intensity (bottom) of the A (dots) and B (squares) components of the $|\pm 1/2\rangle$ transition of the Co^{2+} spectrum in ZnO NWs (nominal Co content of 5 at. %), measured in the X-band for $B \parallel c$. The dashed lines are the calculated curves for the $|\pm 1/2\rangle$ transition within the $S = 3/2$ manifold, using the zero-field splitting of $D = 2.75$ cm^{-1} given by Estle and De Witt (1961). The solid lines represent the same calculated lines but including a correction that takes into account a small error that scales linearly with temperature.

The main feature of this analysis is that the curvature of the $1/I$ vs. T dependence caused by a large zero-field splitting can be misleading, giving the impression of the existence of a finite Curie-Weiss temperature. Thus, we do not believe to observe any ferromagnetic coupling between the Co^{2+} spins in our sample. Additional information may be extracted from the signal line width. Fig. 5.11 shows the temperature dependence of the line width. The increase of the line width with temperature due to increasing spin-lattice relaxation explains why the HF structure is no longer resolved for $T > 40$ K and the signal cannot be measured, at least with the same microwave power, for $T > 90$ K. Considering that both components, A and B, follow the same angular and temperature dependencies, and that the essential difference between them is the line width, we suggest that they represent two different environments of the Co^{2+} ions.

These different environments may be due to different local concentration of Co ions and/or different local strains.

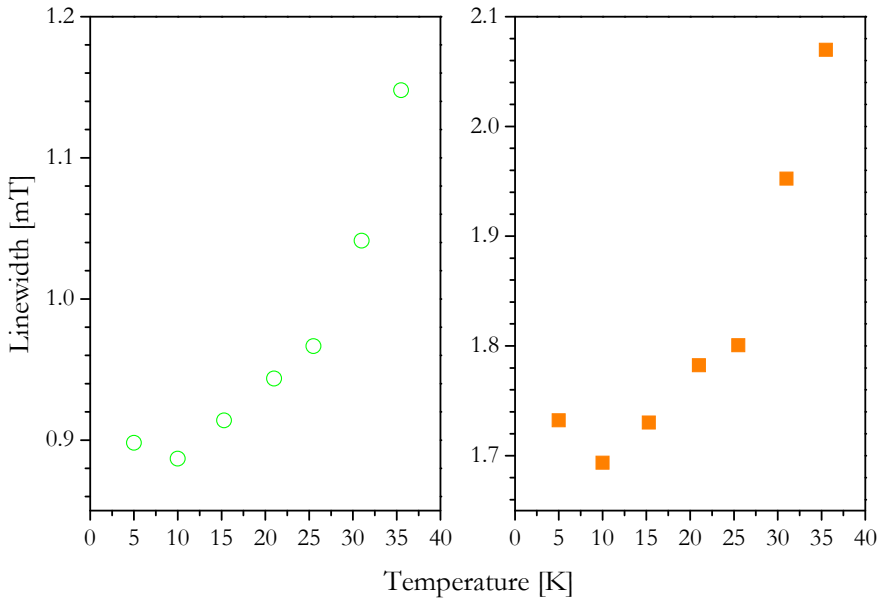

Fig. 5.11. Temperature dependence of the spectral widths for the Co^{2+} lines in ZnO nanowires (nominal content of 5 at. %), measured for $B \parallel c$ in the X-band. Dots belong to the A component and squares to the B component of the spectra.

5.3 Concluding remarks

We investigated the incorporation of Mn and Co into nanometric ZnO wires grown by PLD. For the lowest nominal concentrations, $x_{Mn} = 3$ at. % or $x_{Co} = 5$ at. %, the anisotropic EPR spectra of substitutional isolated Mn^{2+} ($3d^5$, ^6S) or Co^{2+} ($3d^7$, ^4F), respectively, has been measured. The ions could therefore be unambiguously identified by their HF structures due to a nonzero nuclear spin ($I = 5/2$ for ^{55}Mn and $I = 7/2$ for ^{59}Co with 100% natural abundance each), and their valence states could be concluded from the observed FSs. The detection of well resolved anisotropic spectra proved a coherent crystallographic orientation of the NWs. Moreover, in the case of the Co doped NWs it was possible to identify two different components of the spectra, A and B, which probably correspond to two different environments of the Co ions. The temperature dependence of the EPR intensity shows that both components exhibit paramagnetic behaviour. In summary, our samples have good crystalline quality and do not show any ferromagnetic coupling between the Co^{2+} or Mn^{2+} spins.

6 ZnO Transition Metal Doped Colloidal Nanocrystals

Several research groups have made great efforts towards achieving high quality ZnO nanocrystals (NCs), where surface related effects are especially relevant due to the high surface-to-volume ratio. In particular, for metal doped NCs, little is known about the effects of chemical surface modification strategies on doping. This section is dedicated to a detailed investigation of the magnetic and structural properties Co or Mn doped colloidal ZnO nanocrystals. The influence of the surface modification, namely polymer encapsulation and inorganic capping, on the magnetic properties of transition metal (TM) doped ZnO colloidal NCs was analysed. The structural properties were probed by X-ray diffraction (XRD) and transmission electron microscopy (TEM). Electron paramagnetic resonance (EPR) spectra have been measured and analysed to extract information on the incorporation of the ions in the lattice. A detailed analysis by means of simulations of the experimental EPR spectra was carried out. The results presented in this chapter were published in the following papers: (i) Physica Status Solidi (b), **246**, 766 (2009); and (ii) Journal of Applied Physics, **103**, 07D140 (2008).

6.1 Sample preparation

All chemicals were supplied by Aldrich, except ethyl acetate (Lab-Scan). All the chemicals were used as received, except the organic solvents which were dried over molecular sieves. The doped ZnO colloids were synthesized by A. S. Pereira at Chemistry Department of the University of Aveiro by the drop wise addition of 33.3 cm^3 of absolute ethanol containing tetramethylammonium hydroxide ($N(CH_3)_4OH.5H_2O$: 0.552 mol.dm-3) to Zn^{2+}:TM^{2+} dimethylsulfoxide (DMSO) solutions. These solutions were prepared by adding $TM(CH_3COO)_2.6H_2O$ to 100 cm^3 of a DMSO solution 0.101 $mol.dm^{-3}$ in $Zn(CH_3COO)_2.2H_2O$, to achieve a 5% nominal mole doping. Additionally, a sample with a 10% Mn nominal mole doping was prepared in a similar way. To extract the TM doped ZnO NCs as powders, ethyl acetate was added to the colloid; the formed precipitate was centrifuged and washed with ethyl acetate and methanol. In the case of the Co doped samples, surface modifications were carried out. Trioctylphosphine oxide (TOPO) capped Co doped ZnO NCs, obtained after thermal treatment of part of the raw sample at 150°C for 4 hours under a nitrogen stream, were

thoroughly washed with methanol and subjected to chemical surface modification by two distinct routes:

i. A miniemulsion polymerization technique was employed to prepare polystyrene (PS) nanocomposites containing Co^{2+} doped ZnO NCs. The miniemulsion was prepared by mixing a solution containing H_2O (17.7399 g), $NaHCO_3$ (11.9 mg) and SDS (57.5 mg), with another solution containing ZnO:Co (6 mg), styrene (4 ml), hexadecane (82.1 mg) and AIBN (11.5 mg). These two solutions were mixed and stirred for 30 min and sonicated for 5 min. The reacting mixture was held 2 h at 70ºC after being purged with N_2 for 20 min. The final nanocomposite was retrieved through centrifugation and washed with water to remove excess of PS.

ii. In another strategy, the surface modification of the NCs was achieved by dispersing them in 2 cm^3 of TOP and heating the mixture up to 280ºC under a N_2 stream. An excess of TOPSe (2 $mol.dm^{-3}$) was then injected into the hot mixture and the reaction was kept at this temperature for 4 hours, under N_2 atmosphere. During this process, the formation of ZnSe at the ZnO surfaces was monitored by UV/visible spectroscopy. The extraction and washing of the NCs was performed with a mixture (1:3) of methanol and isopropanol.

6.2 Structural Characterization

Figs. 6.1 to 6.4 show typical TEM images and the XRD measurements for all samples which are morphologically well-defined particles with an approximately spherical shape. XRD evidenced the formation of ZnO NCs with a hexagonal wurtzite crystal structure for all samples. No TM clusters or TM-related complexes were detected, at least within the sensitivity of the apparatus. Excluding instrument broadening effects (using a certified standard NIST SRM660a (LaB6 powder)) and applying the Scherrer equation, we estimate the crystallite size as a function of the peak width. In the case of the Co doped ZnO NCs, the raw, the PS capped, and the ZnSe capped samples yielded average diameters of 6 ± 2 nm, 6 ± 2 nm, and 12 ± 3 nm, respectively. For the Mn doped ZnO NCs, the estimated average diameters were of 13 ± 0.5 nm, and 8.2 ± 0.5 nm, for the 5 and 10% Mn, respectively.

The TEM image shown in Fig. 6.1 (b) reveals that each nanocomposite particle of the Co doped NCs results from the PS encapsulation of a group of ZnO:Co NCs forming morphologically well-defined particles with a ZnO phase (dark spots) dispersed in round shaped

PS beads, in agreement with previous findings for other systems [Esteves (2005), Martins (2007)]. Fig. 6.1 (c) shows a TEM image obtained after 20 minutes reaction with TOPSe evidencing fairly morphologically homogenous nanoparticles. Fig. 6.2. (c) and (d) show the histograms of the size distribution of the ZnO Mn doped NCs, revealing the average diameters of 11.8 ± 2.3 and 6.5 ± 1 .2 nm for 5 and 10% Mn contents, respectively. The discrepancy of the TEM and the XRD results for the NCs diameters appears due to the different averaging methods: in the case of the TEM, the weighted average values of the real diameters of the NCs observed in the microscope is calculated, while the XRD values are calculated by the Scherrer formula using the FWHM of a diffraction peak containing the average contribution by all the NCs.

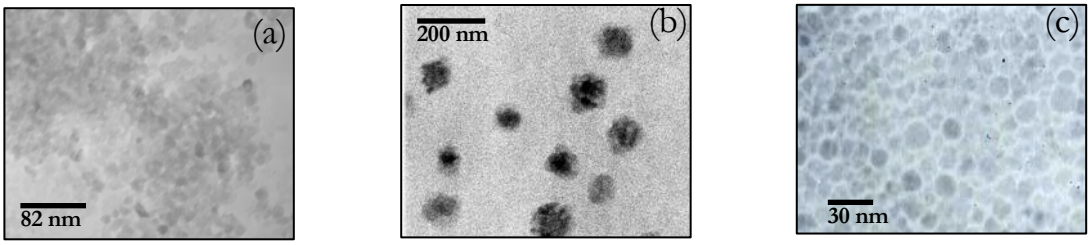

Fig. 6.1. TEM images of (a) ZnO:Co NCs, (b) polystyrene/ZnO:Co nanocomposites, and (c) ZnO:Co NCs capped with ZnSe.

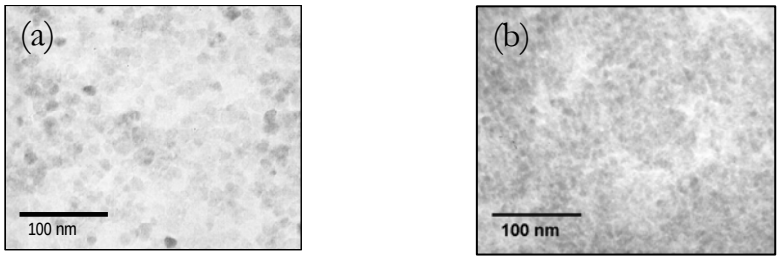

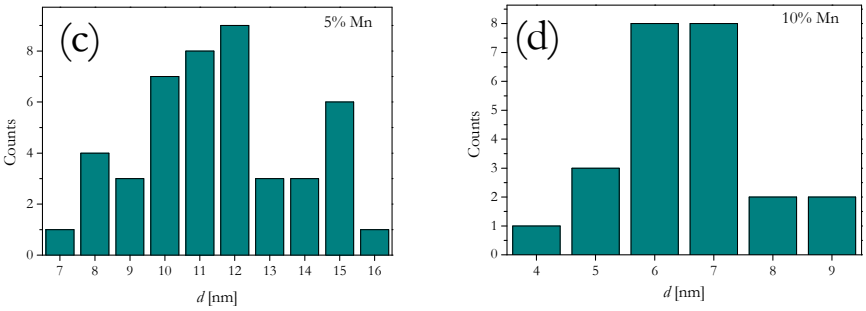

Fig. 6.2. TEM image of colloidal ZnO nanocrystals doped with nominally 5% (a) and 10% (b) of Mn showing average diameters of 11.8 nm and 6.5 nm, respectively. Histograms of the size distribution of the ZnO nanocrystals doped with (c) 5% and (d) 10% Mn.

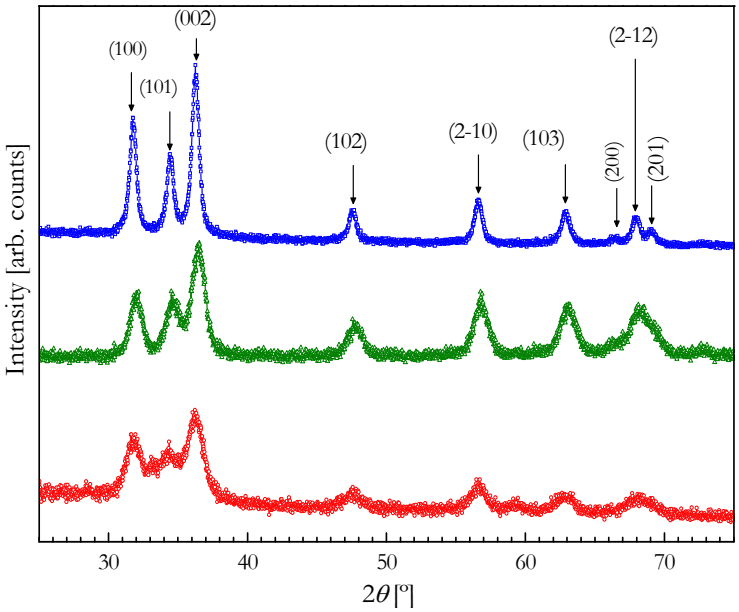

Fig. 6.3. X-ray diffraction measurements of Co doped ZnO NCs (red circles), polystyrene/ZnO:Co nanocomposites (green triangles), and ZnO:Co NCs capped with ZnSe (blues squares). The peak identification is identical for the three samples.

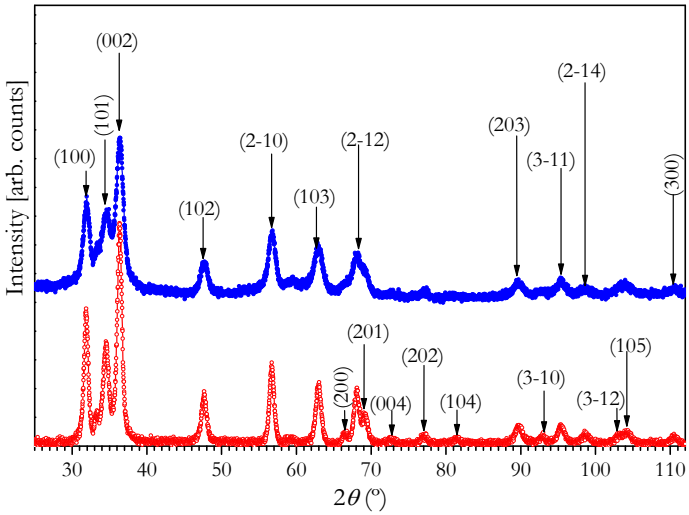

Fig. 6.4. X-ray diffraction patterns of ZnO nanoparticle powders doped with nominal Mn concentrations of 5% (open red circles) and 10% (closed blue circles), respectively. The indexing of the wurtzite ZnO lines is given in the three-index notation for directions and planes of hexagonal systems; (hk.l) is equivalent to the four-index notation (*hkil*), with $i = -(h + k)$.

6.3 EPR ANALYSIS

EPR measurements were performed in the X- (≈9.5 GHz) and Q- (≈34 GHz) bands for all ZnO NCs samples, at temperatures between 4 and 300 K, using a Bruker ESP 300E spectrometer equipped with Oxford Instruments continuous flow helium cryostats.

6.3.1 Co incorporation

As exposed in section 5.2.2, in the case of substitutional Co^{2+} ($3d^7$) on the Zn sites the ground state is the orbital singlet $^4A_2$ and, due to the strong hexagonal crystal field, the zero-field splitting (ZFS) is much larger than the Zeeman energy, consequently, only the electron spin transitions within the $|\pm 1/2\rangle$ doublet can be observed in the available magnetic field range. Thus, the formalism used to describe the spectra is the same as explained is section 5.2.2, considering an effective electron spin $S' = 1/2$ and a nuclear spin $I = 7/2$. The EPR powder spectra were simulated by diagonalization of the spin Hamiltonian (SH) (5.5) and fully integrating over the space angles using the EasySpin software package [Stoll (2006)].

Illustratively, the simulations of the three EPR signals for the raw Co doped NCs are shown in Fig. 6.5.

Fig. 6.6 presents the final result of the simulations of the EPR spectra for all samples, with the respective experimental traces. The analysis proves that part of the spectra (S_I) is due to substitutional Co^{2+} with the effective SH parameters $g'_{\parallel} = 2.2$, $g'_{\perp} = 4.6$, $A'_{\parallel} = 16.0 \times 10^{-4}$ cm^{-1} and $A'_{\perp} = 3.0 \times 10^{-4}$ cm^{-1}, in agreement with the bulk values [Estle and De Wit (1961)]. Additionally, there are two other Co lines, S_{II} and S_{III}, which stem from locally distorted environment and can be described by $g'_{\parallel} = 2.2$ and $g'_{\perp} = 5.3$, and $g'_{\parallel} = 2.2$ and $g'_{\perp} = 3.9$ for S_{II} and S_{III}, respectively, as confirmed by Q-band measurements (Fig. 6.7) which have a higher spectral resolution. The surface exchange reaction with TOPSe occurring during the preparation of the ZnSe capped NCs, in which ZnSe is formed at expense of Zn in the shell of the NCs, partially removes the S_{II} and S_{III} signals, revealing a core-shell structure. As expected, this effect is not so pronounced for the polymer capped NCs, as the surface is not removed by the PS encapsulation.

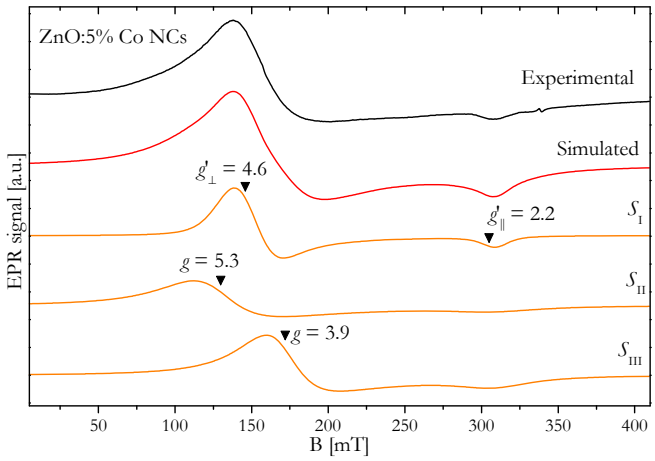

Fig. 6.5. Experimental X-band EPR spectrum at 10 K of ZnO:Co (nominal Co content of 5%) nanocrystals with the respective simulation carried out by adding the EPR signals S_I, S_{II} and S_{III}.

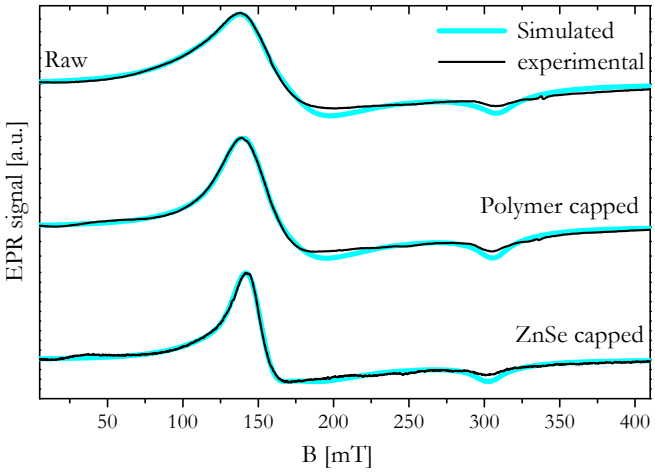

Fig. 6.6. Experimental X-band EPR spectrum at 10 K of ZnO:Co (nominal Co content of 5%) raw nanocrystals, of those after polymer encapsulation, or after reaction with TOPSe. The respective simulations are plotted in light blue carried out by adding the EPR signals S_{I}, S_{II} and S_{III}.

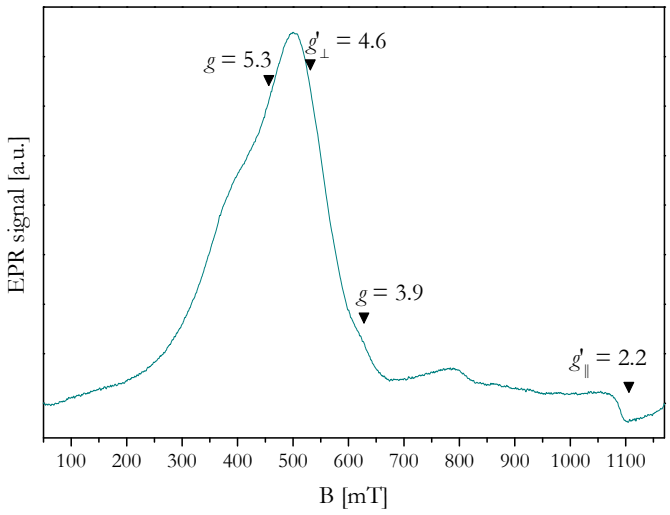

Fig. 6.7. Experimental Q-band EPR spectrum at 10 K of raw nanocrystals ZnO:Co (nominal Co content of 5%).

6.3.2 Mn incorporation

In the case of Mn incorporation, the main part of the signal in the EPR spectra of the NCs stems from substitutional Mn on Zn sites yielding a $3d^5$ electron valence configuration and a ${}^6A_1$ ground state, with a nuclear spin $I = 5/2$ and an electron spin $S = 5/2$. As in the case of the Mn doped ZnO NWs, the EPR data obtained for the Mn doped ZnO NCs described by the SH (5.1).

In these detailed EPR investigations, from the experimental point of view, the modulation amplitude plays a very important role. If this measurement parameter is too large, the lines are broadened and significant details are missed. On the other hand, too small modulation amplitudes mean considerable losses in terms of signal to noise ratio. Hence, a perfect compromise must be found. Fig. 6.8 illustrates this feature of the EPR measurements.

Another important aspect is the difference between the X- and Q-band spectra. If one calculates the angular dependence of the FS transitions, as given in Fig. 6.9, it is clear that for the central electron spin transitions $|\pm 1/2\rangle$ there is a clear shift of the line position due to second order effects in the ZFS.

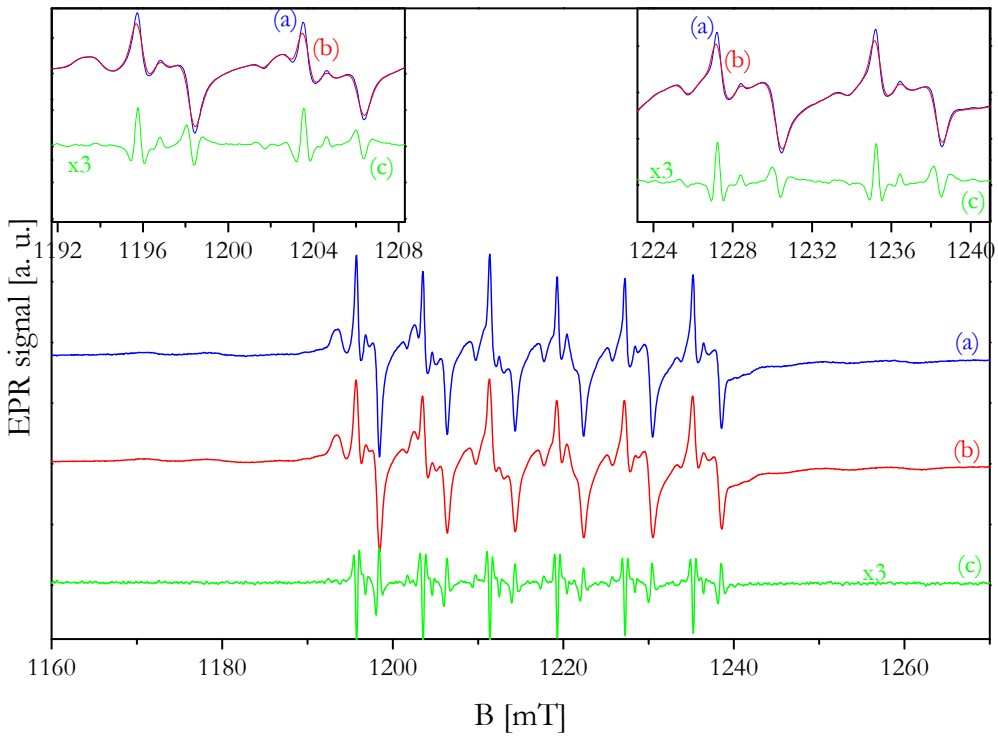

Fig. 6.8. Q-band EPR spectrum at 290 K of the raw Mn doped ZnO nanocrystals (nominal Mn content of 5 at. %), measured with a modulation amplitude of (a) 1.6 G and (b) 4 G. (c) Difference obtained by subtracting spectrum (a) to spectrum (b), showing the influence of the modulation amplitude on the details of the powder spectrum.

Also, the angular dependence is much more pronounced in the X-band. This happens because the higher order effects are smaller in the Q-band, as they are inversely proportional to the magnetic field. Nevertheless, as illustrated in Fig. 6.10, the difference between the powder spectra in the two bands disregarding the hyperfine (HF) structure is small. The real difference in the powder spectrum arises from the HF interactions. The reason is that in the X-band both the allowed (6 lines) and most of the forbidden (36 lines) HF transitions are detected. In the main directions ($B \parallel$ c, and $B \perp$ c), the forbidden transitions are not detectable, but for certain intermediate directions, these transitions are even more intense than the so-called allowed transitions. In the Q-band, the Zeeman interaction term is larger by a factor 3.5 and the spectrum is simplified, because the forbidden transitions are suppressed and more or less only the allowed transitions are measured. Thus, for an accurate measurement of the SH parameters, the Q-band is much more useful. Taking this into account, we chose the Q-band to extract the SH parameters of the measured powder spectra.

Note that in Fig. 6.9, the angular dependence of the fine structure (FS) line positions for substitutional Mn^{2+} in ZnO was calculated for the two equivalent Zn sites, A and B, with C_{3V} point symmetry in the hexagonal ZnO unit cell. These two physically equivalent sites are caused by the ABAB stacking sequence of the wurtzite structure, and can be distinguished by EPR for electron spin systems with $S \geq 2$. In the case of the powder spectrum, these sites are no longer distinguishable, since the integration over the space angle smears out the difference between them (A and B swap positions upon a rotation of $\varphi = 60^{\circ}$).

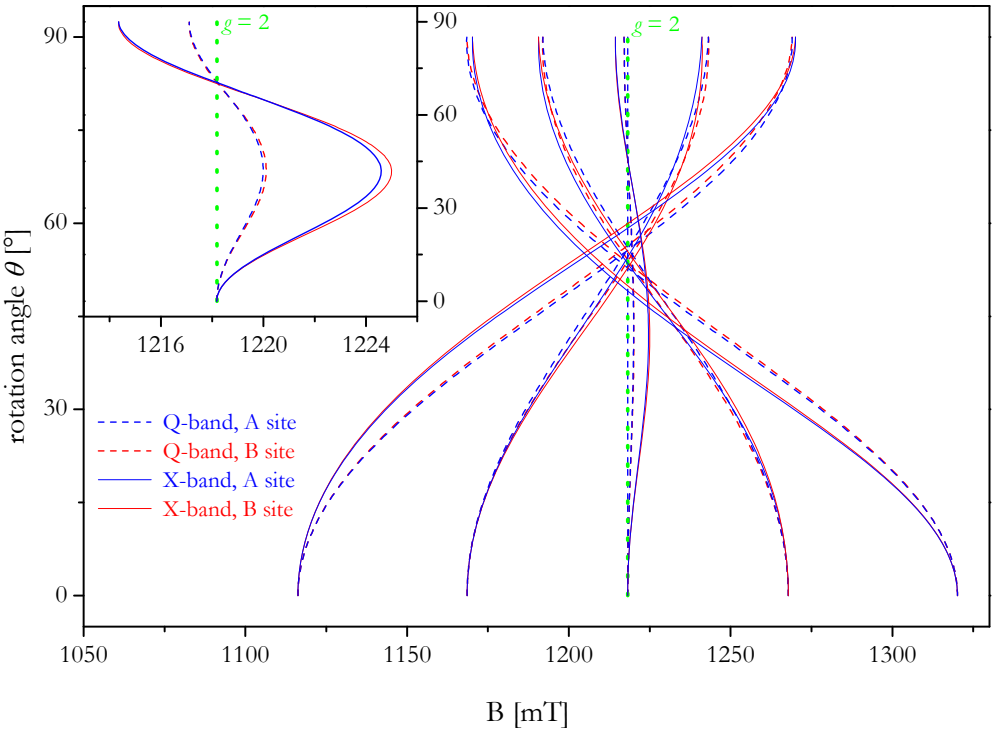

Fig. 6.9. Comparison of the X- and Q-band angular dependence of the fine structure line positions for substitutional Mn^{2+} in ZnO calculated for both A and B sites, using EasySpin software package [Stoll (2006)] and the SH parameters obtained by Schneider *et al.* (1962, 1963). To superimpose both dependences, the X-band values were shifted by 878.8073 mT to the right so that the spectra for $g = 2$ are superimposed. The dotted green line corresponds to $g = 2$. θ is the angle between the applied magnetic field and the c-axis of ZnO.

An additional feature of the EPR spectra that plays a significant role in small structures is the strain. To describe the line broadening coming from strain one has to introduce a strain-induced distribution of the FS parameter D. The influence of this distribution is illustrated in Fig. 6.11.

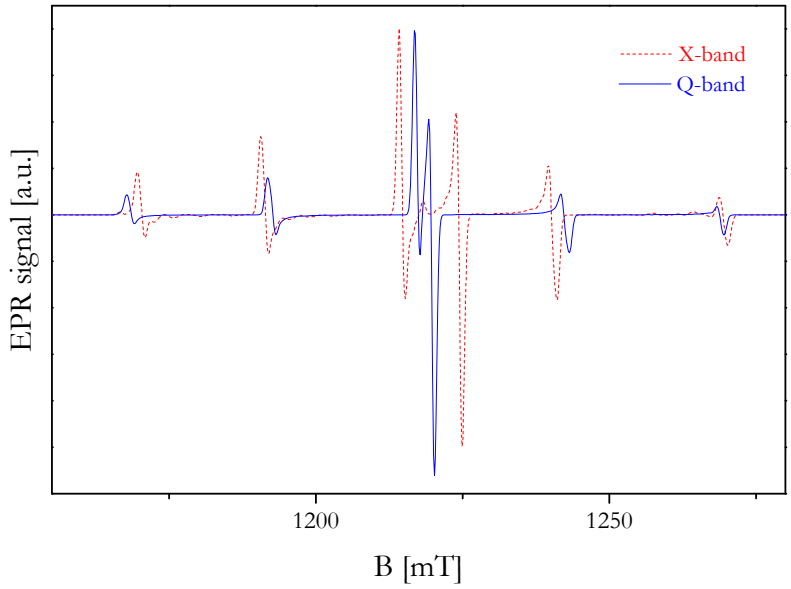

Fig. 6.10. Comparison of the X- and Q-band powder spectrum for substitutional Mn^{2+} in ZnO calculated disregarding the hyperfine interactions, using EasySpin software package [Stoll (2006)] and the SH parameters obtained by Schneider *et al.* (1962, 1963). To superimpose both dependences, the X-band spectrum shifted by 878.8073 mT to the right so that the spectra for $g = 2$ are superimposed.

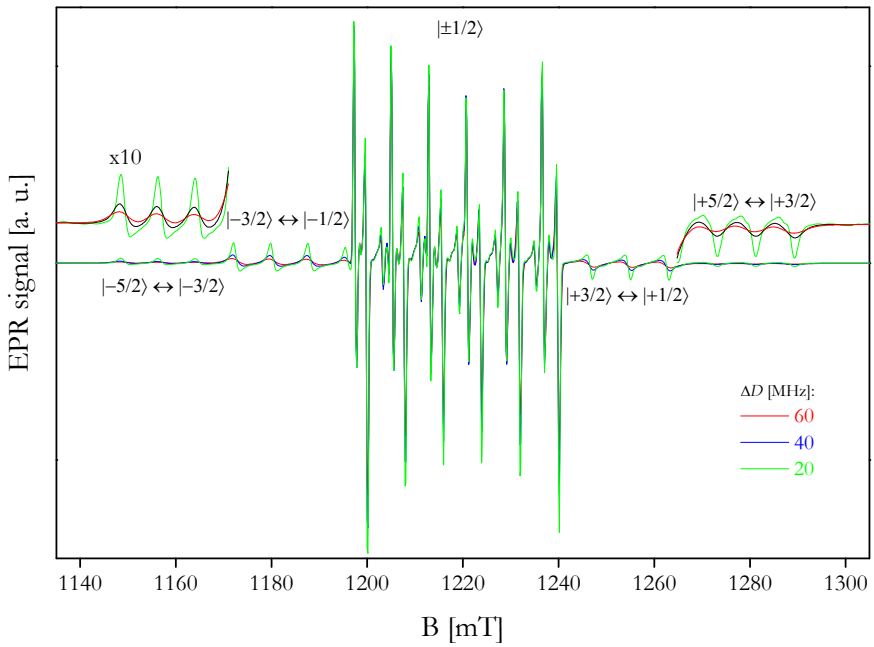

Fig. 6.11. Influence of the strain distribution on the Q-band powder spectrum for substitutional Mn^{2+} in ZnO calculated using EasySpin software package [Stoll (2006)] and the SH parameters obtained by Schneider *et al.* (1962, 1963).

In Fig. 6.12 are presented the Q-band powder spectra measured with modulation amplitude of 2 G for the 5 and 10 % Mn doped ZnO NCs. The outer transitions are magnified for a better visualization. These powder-like spectra contain a wealth of information about the Mn incorporation in the ZnO NCs, as will be revealed by the detailed analysis of the experimental spectra.

From Eq. (5.1) the splitting of the energy levels within the ground state $^6A_1$ for a zero-magnetic field (FS splitting) can be written as a function of the parameters *a*, *D* and (*a*-*F*) [Abragam and Bleany (1986)]:

$$\begin{aligned}\Delta E_1 &= E\left[{}^6\mathrm{A}_1\left(\pm\frac{5}{2}\right)\right]-E\left[{}^6\mathrm{A}_1\left(\pm\frac{1}{2}\right)\right] = \pm\frac{1}{3}\left[(18D+a\text{-}F)^2+80a^2\right]^{1/2},\\ \Delta E_2 &= E\left[{}^6\mathrm{A}_1\left(\pm\frac{3}{2}\right)\right]-E\left[{}^6\mathrm{A}_1\left(\pm\frac{1}{2}\right)\right] = \frac{3}{2}(a-F)-D\pm\frac{1}{6}\left[(18D+a\text{-}F)^2+80a^2\right]^{1/2},\end{aligned} \tag{6.1}$$

where the signs "+" and "-" correspond to $D > 0$ and < 0, respectively. The extent of the FS splitting of the spectra is determined by the magnitude and symmetry of the local electrical field and the covalent bonding with surrounding ions.

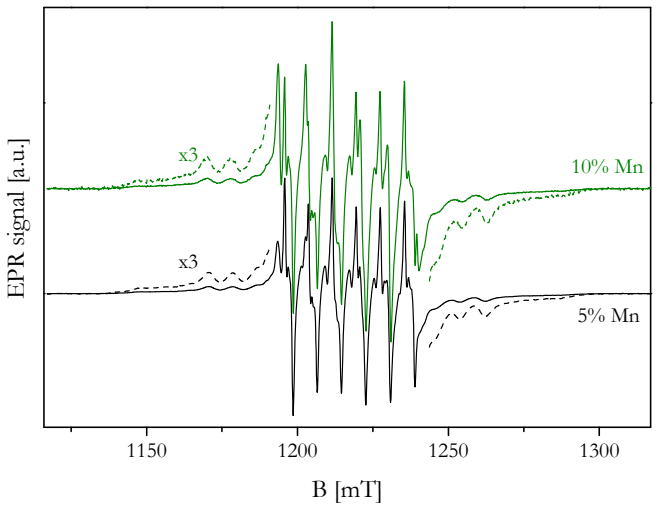

Fig. 6.12. Experimental Q-band EPR spectrum at 290 K of raw nanocrystals ZnO:Mn (nominal Mn content of 5 and 10 at. %). For a better visualization, the outer transitions are magnified (dashed lines).

The magnitude of the HF splitting given by the second term in the SH (5.1) is very sensitive to changes in the wave function of the Mn^{2+} $3d^5$ electrons. Besides the HF transitions of the central FS transition $M_S = -1/2 \leftrightarrow M_S = +1/2$ previously reported in other EPR studies

of Mn-doped ZnO NCs [Zhou (2003), Viswannatha (2004)], we have also been able to directly detect some HF components of the outer Mn FS transitions. The magnifications of the spectra given in Fig. 6.12 show the part of the HF lines due to the outer Mn FS transitions $M_S = \pm 5/2 \leftrightarrow M_S = \pm 3/2$ that are not completely overlapped by the other transitions. The visible amplitude of the outer FS transitions $M_S = \pm 5/2 \leftrightarrow M_S = \pm 3/2$ and $M_S = \pm 3/2 \leftrightarrow M_S = \pm 1/2$ is always strongly suppressed as compared to that of the central FS transition $M_S = -1/2 \leftrightarrow M_S = +1/2$, which is mainly caused by the stronger angular dependence of the line positions of the outer transitions and the random orientation of the centre axes in the powder samples. Also in single crystals, stochastic strain fields created by point defects and dislocations are a common source of inhomogeneous broadening of the line width. Therefore, only the centres having orientations of the centre axes that give an evanescent slope of the line positions contribute to a detectable signal. The contributions of the other centre orientations are smeared out and cannot be detected. Because the experimental spectra enable us to distinguish the HF structure of the different FS transitions directly, the weighted average of the FS parameters D and $(a\text{-}F)$ over the possible local configurations can be obtained from the investigated powder spectra with high accuracy. However, the FS parameters can also be obtained by computer simulation in cases where the outer FS lines are broadened beyond the detection, because the shape of the HF spectrum related to the central FS transition is affected by the magnitude of these FS terms in higher order of perturbation theory [Koh (1984)]. Therefore, the influence of strain and size effects as well as the changes in the covalent bonding on the spectra can be analyzed with high accuracy by computer simulation using the complete SH (5.1).

For the NWs, the SH parameters could be obtained by an analysis of the line positions of the different spin transitions for special directions, as described in section 5.2.1 for the case of $B \parallel c$. However, in the case of powder spectra the centre axes are randomly distributed, and therefore one has in addition to fully integrate over the space angles in order to calculate the spectra and to determine the SH parameters by fitting the spectra.

Using the EasySpin software package [Stoll (2006)] we have solved the SH (5.1) by exact diagonalization and simulated the respective spectra. The results of such simulations together with the experimental spectra are shown in Fig. 6.13. We started our fitting procedure by simulating the substitutional Mn^{2+} spectrum S_1 using, in a first step, the SH parameters for bulk ZnO [Schneider (1962, 1963)] and found that this was not enough to fully describe the

experimental Mn^{2+} spectrum. In order to evidence the part of the spectrum still lacking description, we determined the difference between the spectra of the 5 and 10% Mn doped NCs, given in Fig. 6.14.

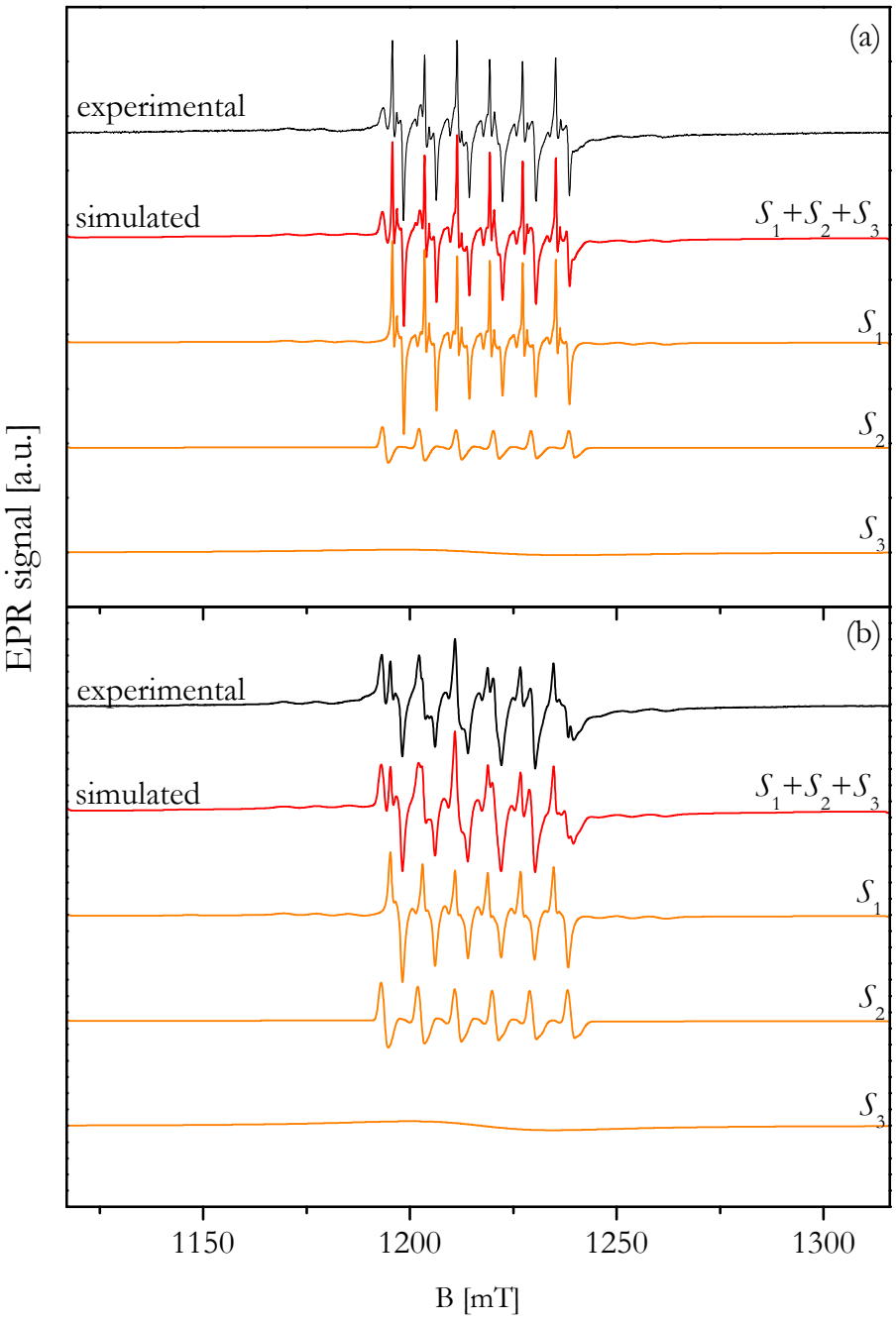

Fig. 6.13. EPR spectrum for (a) 5% and (b) 10% Mn doped colloidal ZnO nanocrystals, measured in the Q-band at 290 K, along with the respective simulations carried out by adding the EPR signals S_1, S_2, and S_3.

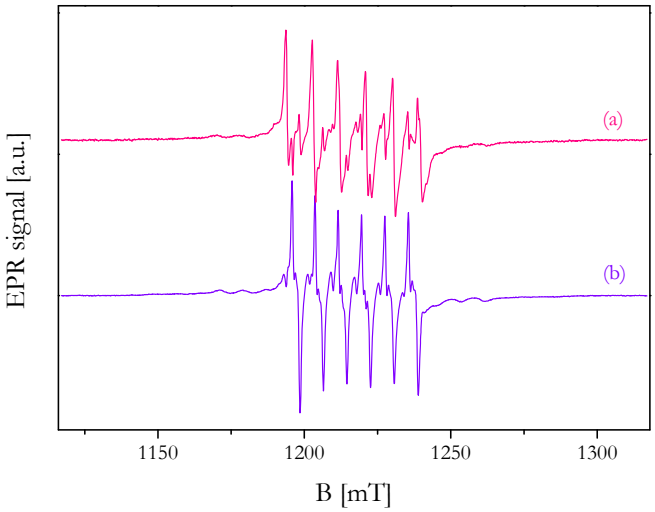

Fig. 6.14. Difference obtained by the subtraction of the experimental Q-band EPR spectrum, taken at 290 K, of the raw Mn doped ZnO nanocrystals (nominal Mn content of 5 and 10%), yielding (a) 10% Mn spectrum - 5% Mn spectrum, and (b) 5% Mn spectrum - 10% Mn spectrum.

This procedure clearly revealed a second signal S_2 with a behaviour similar to that of the Mn^{2+} EPR spectrum S_1, but with a 14% larger HF splitting, and a 20% smaller D. To fully describe the powder spectrum, we still had to add a broad Lorentzian line, S_3, which is commonly present in highly Mn doped ZnO due to local regions with higher Mn concentrations. The SH parameters describing the three parts of the spectrum were varied around the values obtained in the first step to obtain an optimal fit to the experimental spectrum. Furthermore, in order to achieve a sound simulation of the observed line broadening of the spectra S_1 and S_2 we had to introduce a distribution ΔD of the zero-field parameter D describing the local lattice distortions in the vicinity of the Mn impurity in the different regions of the NCs. In the case of the spectrum S_1, we found that this distribution could not be simply Gaussian (random distribution), but had to be a sum of at least three Gaussian distributions with different centres and widths. In the case of the spectrum S_2, an orthorhombic distortion had to be added to the strain distribution.

Finally, the intensity of the spectra S_1, S_2 and S_3 were determined by double integration. We obtained the intensity I_2/I_1 ratios of 0.2 and 0.3 for the 5% and 10% Mn-doped samples, respectively. The resulting SH parameters are given in Table 6.1.

Table 6.1. SH parameters determined for the Q-band EPR spectra of the Mn doped ZnO nanocrystals. Except for the *g*-values and the line width, all values are given in 10^{-4} cm^{-1}.

x	5%			10%			Schneider (1962, 1963)
EPR signal	S_1	S_2	S_3	S_1	S_2	S_3	bulk crystal
$g_{\|\|}$	2.0010 ± 0.0002	2.0011 ± 0.0002	1.9993 ± 0.0005	2.0010 ± 0.0002	2.0006 ± 0.0002	1.9993 ± 0.0005	2.0012 ± 0.0002
$g_{\perp}$	2.0009 ± 0.0002	2.0010 ± 0.0002		2.0009 ± 0.0002	2.0006 ± 0.0002		
$A_{\|\|}$	-73.9 ± 0.3	-84.4 ± 0.3	–	-73.9 ± 0.3	-84.4 ± 0.3	–	-74.10 ± 0.05
$A_{\perp}$	-73.8 ± 0.3	-84.4 ± 0.3	–	-73.8 ± 0.3	-84.4 ± 0.3	–	
D	-232.8 ± 0.3	-183.5 ± 0.3	–	-25.3 ± 0.2	-200.1 ± 0.3	–	-236.2 ± 0.4
ΔD	53.67 ± 0.3	130.1 ± 0.3	–	4.0 ± 0.5	133.4 ± 0.3	–	–
$(a–F)$	6.20	6.20	–	6.20	6.20	–	6.20 ± 0.05
FWHM [mT]	0.71 ± 0.01	0.9 ± 0.1	70 ± 2	0.70 ± 0.01	0.9 ±0.1	60 ± 2	–

The symbols || and ⊥ stand for parallel and perpendicular to the *c*-axis, respectively. FWHM stands for full width at half maximum.

Previous investigations have also shown that, in addition to the corresponding bulk-like spectra, another six-line spectrum similar to S_2, but with a larger HF splitting, appears in Mn doped CdS and ZnS [Kennedy (1995), Borse (1999), Zhou (2006b)] as well as in Mn doped ZnO NCs [Norberg (2004), Zhou (2003), Viswannatha (2004)]. Based on ionicity arguments these spectra were ascribed to Mn in the surface shell of the NCs. The decrease of the NC size (increase of the surface-to-volume ratio) detected by XRD and TEM and the increase of the determined intensity ratio I_2/I_1 of the EPR spectra with increasing Mn content allows us first to ascribe S_1 and S_2 to the manganese in the core and in the surface shell of the NCs, respectively; and second to estimate the thickness of the surface shell using a simplified model with spherical NCs and average Mn concentrations in the interior and surface region of the nanoparticles [Gehlhoff (2008)]. In the present case quite similar transition probabilities can be assumed for the transitions that form the spectra S_1 and S_2. Therefore, the intensity ratio I_2/I_1 is given by the number of Mn centres in the surface layer and the interior of the NCs, respectively. Assuming that the NCs are spherical, the intensity ratio is simply given by:

$$\frac{I_2}{I_1} = \frac{V_{shell}}{V_{core}} \cdot \frac{n_{shell}}{n_{core}}, \tag{6.2}$$

where the volume of the shell is $V_{shell} = \frac{1}{6}\pi\left[d^3 - (d-t)^3\right]$, with d being the NC diameter, and t being the shell thickness, $V_{core} = \frac{1}{6}\pi(d-t)^3$ is the volume of the core, and n_{shell} and n_{core} are the Mn concentration in the shell and the core respectively. Thus, the intensity ratio may be written as:

$$\frac{I_2}{I_1} = \frac{n_{shell}}{n_{core}} \frac{d^3 - (d-t)^3}{(d-t)^3}. \tag{6.3}$$

On the other hand, we observe a broadening of the single EPR lines in the shell. In the case of the single lines, the broadening is due to the dipole-dipole interaction and, for a Lorentzian line shape, the full width at half maximum (FWHM) is given by the expression [Zhidomirov (1985)]:

$$FWHM = \left(\frac{8\pi^2}{9\sqrt{3}}\right) k g \mu_B n. \tag{6.4}$$

where $k = 3/2$ for spins in resonance, and n is the centre concentration. From this relation we can calculate the concentration ratio in the shell and in the core $n_{shell}/n_{core} = 1.3$, demonstrating an accumulation of the Mn concentration in the shell.

The resulting intensity ratios I_2/I_1 for some layer thicknesses are shown in Fig. 6.15 as a function of the average diameters of the NCs. Using the diameters of the NCs $d_{XRD}(a) = (13.0 \pm 0.5)$ nm and $d_{XRD}(b) = (8.2 \pm 0.5)$ nm estimated by XRD measurements and the determined intensity ratios I_2/I_1 of 0.2 and 0.3 we obtain a thickness of the surface layer of $t_a = 0.55$ nm and $t_b = 0.61$ nm for the 5% and 10% Mn doped NCs, respectively. With the average diameters of the NCs estimated by TEM the values $t_a(\text{av}) = 0.44$ nm and $t_b(\text{av}) = 0.55$ nm are obtained.

The relatively small difference between the values calculated with the different diameters obtained by XRD and TEM are due to the fact that in first order the surface layer thickness is only determined by the diameter ratio d_a/d_b. Additionally, the determined values are sensitively dependent on the intensity ratio I_2/I_1. Therefore, a very careful determination of this ratio is an absolute prerequisite for a quantitative analysis. However, besides all experimental uncertainties and the used simplification we obtained the unique result that the surface layer thickness is very small, of the order of 0.4 to 0.6 nm, and that the Mn is not uniformly incorporated in the NCs, but there is an accumulation of Mn in the shell region. Moreover, the enrichment of the Mn in

the surface region was confirmed experimentally by the strong decreasing of the I_2/I_1 if the surface is treated with ZnSe removing part of the ZnO surface. The production of a set of NCs doped with an array of different Mn concentrations and with a narrower size distribution would allow a more precise determination of the thickness of the surface layer and of the distribution of the incorporated Mn between the core and the shell region.

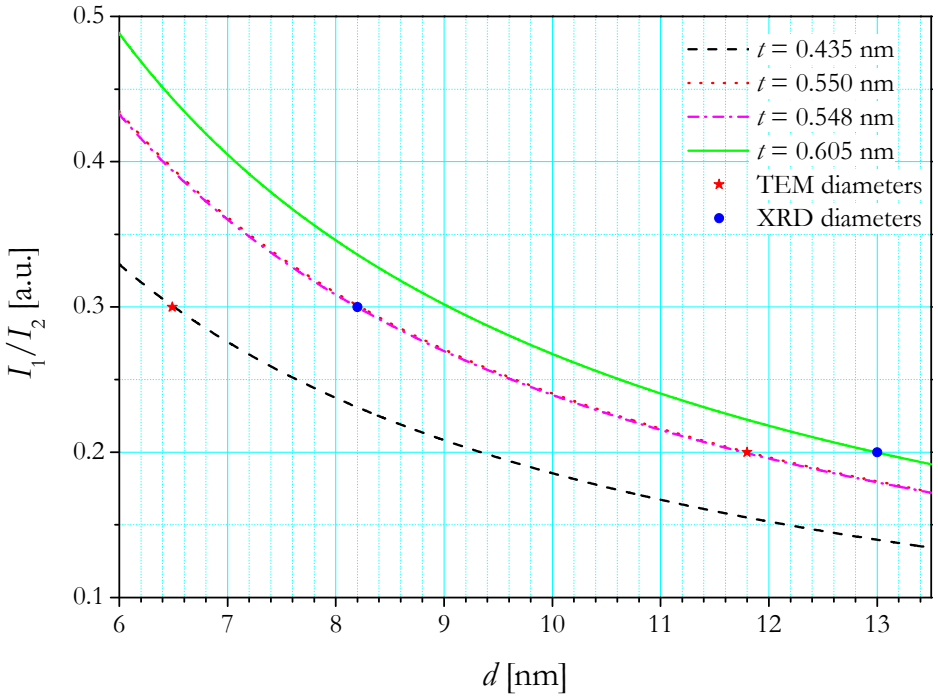

Fig. 6.15. Ratio of the intensities of the EPR signals S_2 and S_1 as a function of the nanocrystals average diameters.

As mentioned above, the quantitative determination of the intensities of the spectra S_1 and S_2 have to consider the experimentally observed line broadening. Neglecting deviations from the C_{3V} symmetry for the Mn site we modelled the strain-induced line broadening of the spectrum S_1 by a sum of three Gaussian distributions of D with the mean values D = 250.2, 235.2, and 193.5 × 10^{-4} cm^{-1} and FWHM of ΔD = 93.4, 40.0, and 93.4 × 10^{-4} cm^{-1}, respectively. In the case of S_2, we were able to model the strain-induced line broadening simply with one Gaussian distribution of D with ΔD = 130.1×10^{-4} cm^{-1} and 133.4×10^{-4} cm^{-1} for the 5 and 10% Mn doped NCs, respectively. The presence of the large D distribution reflects a stronger variation of the crystal field (CF) distortions in the NCs as compared to bulk crystals [Schneider (1962, 1963)] and epitaxial layers [Diaconu (2005b)]. The observed increase of the ΔD variation

for Mn in the shell region as compared to Mn in the core of the NCs can be explained by a greater capacity of the shell to structurally relax in different ways.

Theoretical predictions of the FS parameters for d^5 configuration ions (both Mn^{2+} and Fe^{3+}) need to take into account spin-orbit coupling in higher orders in the considered CFs and admixture of the wave functions of the excited states with those of competing contributions [Wan-Lun and Min-Guang (1988), Newman and Ng (1989), Kuang (1996)]. Deviations of the parameters *D*, *a*-*F* and *a* from the experimental data can be explained by local lattice distortions in terms of the superposition model [Newman and Ng (1989)] and by complete diagonalizing of the energy matrix for a d^5 configuration in a trigonal CF [Kuang and Chen (1987)]. For hexagonal GaN:Mn^{2+} and GaN:Fe^{3+} a displacement of the TM ions towards the N ligand along the lattice direction *c* is predicted [Zheng (2001)]. For ZnO:Fe^{3+} the calculation indicates a compression distortion around Fe^{3+} upon retention of the C_{3V} symmetry [Ju-Fen (2006)]. This compression may be ascribed by the facts that the ionic radius of Fe^{3+} (r = 0.64 Å) is smaller than that of the host Zn^{2+} (r = 0.74 Å) and the effective charge of Fe^{3+} is larger than that of Zn^{2+}. For ZnO:Mn detailed calculations do not exist. However, the larger radius of Mn^{2+} (r = 0.80 Å) in comparison to Zn^{2+} suggests a dilatation of the trigonally distorted MnO tetrahedron embedded in the ZnO lattice. EPR measurements have shown that the value of the axial FS parameter *D* of Mn^{2+} both in $Zn_{1-x}Mn_xO$ films and bulk materials is strongly correlated with the macroscopic strain induced by the heteroepitaxy on sapphire and the Mn content [Diaconu (2005b,c)]. With increasing Mn concentration, a decrease of the absolute value of *D* both for films and single crystals is observed [Diaconu (2005b,c)]. The sign and the value of the *D*-shift are determined by the special Mn-induced local distortion of the ZnO material. For substitutional Mn in the core of the NCs, the absolute *D*-value is approximately equal to the value obtained for bulk ZnO (Table 6.1). The smaller absolute *D*-value observed for the Mn in the shell region can be caused by changes of the local distortions due to the proximity of the surface and its passivation that depends on the especial preparation of the NCs. Empirically it was found that the absolute *D*-value increases markedly with decreasing covalency of the Mn^{2+}-anion bonds in II-VI crystals [Title (1963)]. Large spin-orbit coupling coefficients of the ligands can also make a large positive contribution to the ZFS via the covalence effects [Kuang (1996)]. The competition between the different contributions from the local crystal distortions, covalence as well as number and kind of ligands near the surface results in the smaller absolute

D-value observed in the shell related Mn signal. To estimate the different and partly compensating contributions to the ZFS, independent measurements of the local distortion of the regular ZnO lattice structure by the incorporation of Mn in ZnO NCs are necessary. Recently, extended X-ray absorption fine structure spectroscopy (EXAFS) was performed to obtain information on the local arrangement of Mn ions incorporated in nanocrystalline ZnO [Koteski (2007)] consisting of ZnO/$Zn(OH)_2$ core-shell structure. In these samples, the surface is passivated, due to the chosen preparation, by a thin layer of amorphous $Zn(OH)_2$ [Zhou (2002), Zhou (2003)]. The fit of the EXAFS results exhibits a strong lattice distortion around the Mn as compared to pure ZnO. However, the experimental data can be fitted with different parameter sets, and the authors could not differentiate between Mn^{2+} in the core and in the surface shell. According to one possible parameter set the Mn-O bond length of the MnO_4 entity (tetrahedron) embedded in ZnO indicates a sizeable increase in the 1-fold subshell (bond direction || *c*), while the bond length in the 3-fold coordinated first subshell is slightly reduced as compared to the ZnO_4 entity [Koteski (2007)]. While the increase of the Mn-O bond length in the *c*-direction is in agreement with the expected increase of the dimension of the MnO_4 tetrahedron, considering the difference in the ionic radii of Mn^{2+} and Zn^{2+}, the reduction of the non-axial Mn-O bond length is in disagreement with such a simple model and the experimental results, indicating that the lattice parameters *a* and *c* of ZnO NCs increase linearly with increasing Mn content [Lou (2005)].

Let us now address in more detail the question of the location of the Mn ions and the value of the HF constant *A*. Analyzing substitutional Mn^{2+} in various compounds, Simanék and Müller (1970) have shown that the absolute value of *A* decreases monotonically with the covalency *C* of the bond between Mn^{2+} and its *m*-nearest neighbours X of the MnX_m cluster embedded in the compounds. For more ionically bonded compounds like the II-VI semiconductors, even a linear relationship holds within the relatively large uncertainty of the calculated *C*/*m* ratio resulting from the empirical electronegativity data. The increase of the averaged HF constant $A_{av} = 1/3A_{\|} + 2/3A_{\perp}$ from the value $A_{av}(c) = (-73.9 \pm 0.3)\times10^{-4}$ cm^{-1} for Mn^{2+} in the core to $A_{av}(s) = (-84.0 \pm 0.3)$ mT for Mn^{2+} within the surface corresponds to the expected increase of the HF constant *A* for the transition from a MnO_4 to a MnO_6 cluster. The measured value $A_{av}(s)$ is nearly identical to the HF constant $A = (-81.0 \pm 0.2) \times10^{-4}$ cm^{-1} mT for the octahedrally bonded Mn^{2+} in MgO [Low (1957)] that has a quite similar Mn-O bonding

length. The quantitative agreement between the measured average HF constant in the surface shell and the calculated value for the MnO_6 cluster as well as the observed A-value for Mn^{2+} in MgO convincingly supports the assumption that the Mn^{2+} ion in the surface shell is sixfold bonded in a distorted octahedral environment. Corresponding results were also observed for the other Mn-doped II-VI compounds [Gehlhoff (unpublished)]. The observed strong intensity decrease of this component of the Mn^{2+} spectrum through the surface treatment that reduces the surface-to-volume ratio of the NCs excludes the possibility that this part of the spectrum is caused by interstitial Mn^{2+} in the core of the NCs.

Thus, we have distinguished three different EPR signals comprising the Mn spectrum of the ZnO NCs: a) a broad Lorentzian line coming from regions with a higher local Mn content; b) a signal clearly stemming from substitutional Mn^{2+} on Zn sites in the core of the NCs; and c) a signal caused by Mn in the surface shell of the NCs with a larger HF splitting that is attributed to Mn^{2+} at substitutional sites with distorted octahedral symmetry.

6.4 Concluding remarks

We have succeeded to incorporate Mn and Co ions in ZnO colloidal NCs and to characterize the local environment of the ions in the NCs using EPR spectroscopy. No evidence of ferromagnetism was found in any case. For both types of doping, the TM incorporation was heterogeneous in the sense that the EPR spectra were always composed partly of a signal stemming from substitutional TM ions on Zn sites, and partly of that coming from TM ions in distorted or TM enriched environments. Furthermore, we have proved that the TM doped colloidal ZnO NCs exhibit a core-shell structure revealed by the relative intensities of the EPR spectra and by the performed surface modifications.

In the case of the Co doped NCs, we are able to distinguish three different signals: one coming from substitutional Co^{2+} in the NC core with SH parameters similar to the bulk ones, and two other Co lines caused by locally distorted environment in the shell. The core-shell structure is also proved by partially removing the shell signal when ZnSe is formed at the expense of Zn in the shell of the NCs, *i.e.* "etching" the shell. As the surface shell is not

removed by the PS encapsulation, this effect is not so pronounced for this surface modification procedure.

In the case of the Mn doped ZnO NCs, we distinguish three components of the Mn^{2+} EPR spectrum, one coming from regions with a higher Mn concentration, another one stemming from substitutional Mn^{2+} in the NC core, and a third one being produced by Mn^{2+} in the surface shell of the NCs exhibiting a larger HF splitting. These features are unambiguously obtained by the simulation and fitting of the experimental powder spectra and described by the determined SH parameters. The Mn ions incorporated in the NCs are subjected to a larger strain in comparison with bulk crystals, which is particularly reflected by the variation of the FS parameter *D*. The covalency of the Mn-O bond is reflected in the HF constant and in the *D*-value. The higher value for the HF constant found for the Mn^{2+} in the shell region can be explained with the formation of MnO_6 clusters in this part of the NCs. We also find that, as the Mn content increases, the surface-related component shows increasing relative intensity. These results are in agreement with the XRD and TEM measurements that show decreasing NC size and increasing lattice distortions for increasing Mn content. Using a simple spherical core-shell model for the size of the NCs we determined the distribution of the manganese and the thickness of the shell from the measured intensities of the EPR signals produced by the Mn^{2+} in the core and the surface shell region. In spite of all experimental uncertainties and used simplifications we obtained the unique result that the surface layer thickness is very small, in the order of 0.4 – 0.6 nm, and that the Mn atoms are not uniformly incorporated in the NCs but that there is an accumulation of the Mn atoms in the shell region.

7 Co, Al or Mn, Al co-doped ZnO films

In this chapter, Co and Al or Mn and Al co-doped ZnO thin films grown by pulsed laser deposition (PLD) are investigated by means of different techniques. The main objective is to determine the role of charge carriers in the occurrence of ferromagnetism.

7.1 Samples

Four ZnO films, co-doped either with Co and Al or Mn and Al, were grown at the University of Leipzig from $Zn_{0.945}Mn_{0.05}Al_{0.005}O$ or $Zn_{0.945}Co_{0.05}Al_{0.005}O$ ceramic targets, respectively, on 10×10 mm^2 *a*-plane sapphire substrates by means of PLD, using a KrF excimer laser. The samples are labelled TF1, TF2, TF3 and TF4, according to Table 7.1. The background oxygen pressure was varied between 4×10^{-5} and 0.005 mbar and the substrate temperature between 343 and 726°C, respectively. The film thickness was controlled during the PLD growth by the number of laser pulses, and ex situ determined by ellipsometry measurements. The free carrier concentration n was determined by Hall effect measurements and controlled between 10^{18} and 10^{20} cm^{-3} by the variation of the oxygen pressure, substrate temperature, and film thickness during the film preparation. The composition of the films was measured by combined Rutherford backscattering spectrometry (RBS) and particle induced X-ray emission (PIXE). The Al content in the films could not be determined, due to the underlying Al_2O_3 substrate. The Co and Mn contents in the films turned out to be larger than in the corresponding PLD targets and amounted to about 9 at. %. The crystal structure of the films was characterized by X-ray diffraction (XRD), which indicated the highly *c*-axis-oriented ZnO films without any visible impurities.

The growth parameters, the electron concentration n, and the film thicknesses are given in Table 7.1.

Table 7.1. PLD growth parameters, electron concentration *n*, and film thicknesses for the ZnO thin films.

Sample	Target composition	Oxygen partial pressure [mbar]	Substrate temperature [ºC]	Number of pulses	Film thickness [nm]	*n* (5 K) [cm^{-3}]
TF1	$Zn_{0.945}Mn_{0.05}Al_{0.005}O$	4×10^{-5}	343	1500	36	2.13×10^{20}
TF2	$Zn_{0.945}Mn_{0.05}Al_{0.005}O$	0.005	726	30300	782	9.96×10^{18}
TF3	$Zn_{0.945}Co_{0.05}Al_{0.005}O$	4×10^{-5}	450	1800	43	1.42×10^{20}
TF4	$Zn_{0.945}Co_{0.05}Al_{0.005}O$	0.001	726	30300	685	4.35×10^{18}

7.2 MAGNETIC PROPERTIES

Both magnetoresistance (MR) and Hall effect were measured with the field applied parallel to the *c*-axis of the films (perpendicular to film surface) in the van der Pauw configuration. Fields up to 6 T were applied over a wide temperature range from 5 to 290 K. The charge carriers were confirmed to be *n*-type by Hall measurements for all the samples.

The MR was measured at 5 K for all samples, and is represented as a function of the applied field in Fig. 7.1. The two Mn doped films and the Co doped film with the lower electron concentration show a positive MR at low temperature. In magnetically doped ZnO, the positive MR is usually related to quantum corrections to the conductivity due to the influence of the spin-split conduction band on the electron-electron interaction [Xu (2007b)].

The electronic properties of *n*-type semiconductors depend on the ratio between the mean distance between donors $r = [3/(4\pi n)]^{1/3}$ and their effective Bohr radius a_B. In the dilute case, $r >> a_B$, and electrons are bound to individual impurities, so that low-temperature conduction proceeds by means of phonon-assisted tunnelling between occupied and empty states. In this case, the semiconductor is in the insulating regime. In the opposite limit, $r << a_B$, the electrons are in the impurity band that may overlap with the conduction band, and the low-temperature mobility is determined by ionized impurity scattering. The critical electron concentration n_c, at which the metal to insulator transition occurs, was estimated for a Co doped film by Xu *et al.* (2006): $n_c = 4\times10^{19}$ cm^{-3}. From the estimated n_c, one expects delocalized wave functions for $n > 4\times10^{19}$ cm^{-3}, and localized wave functions for $n < 4\times10^{19}$ cm^{-3}. This explains the low temperature negative MR ($n > n_c$) as observed for the Co doped film with the larger electron concentration. Moreover, semiconductors are considered in the weakly localized regime when the product of the Fermi wave vector (k_F) and the mean free path (l) defined as

$k_F l = \hbar\left(3\pi^2\right)^{2/3} / \left(e^2 \varrho n^{1/3}\right)$ is larger than 1 [Andrearczyk (2005)], as it is in the case of sample TF4 ($k_F l$ = 3.12). For Co doped ZnO, the attribution of the origin of the negative MR to the field suppression of the weak localization has been found to be in good agreement with the experimental data [Xu (2007b)].

Furthermore, the MR clearly increases with decreasing n for all samples, in agreement with the results reported by Kim *et al.* (2003) and Xu *et al.* (2007a), indicating that the electron concentration is primarily influenced by polarons, electron localization and defects.

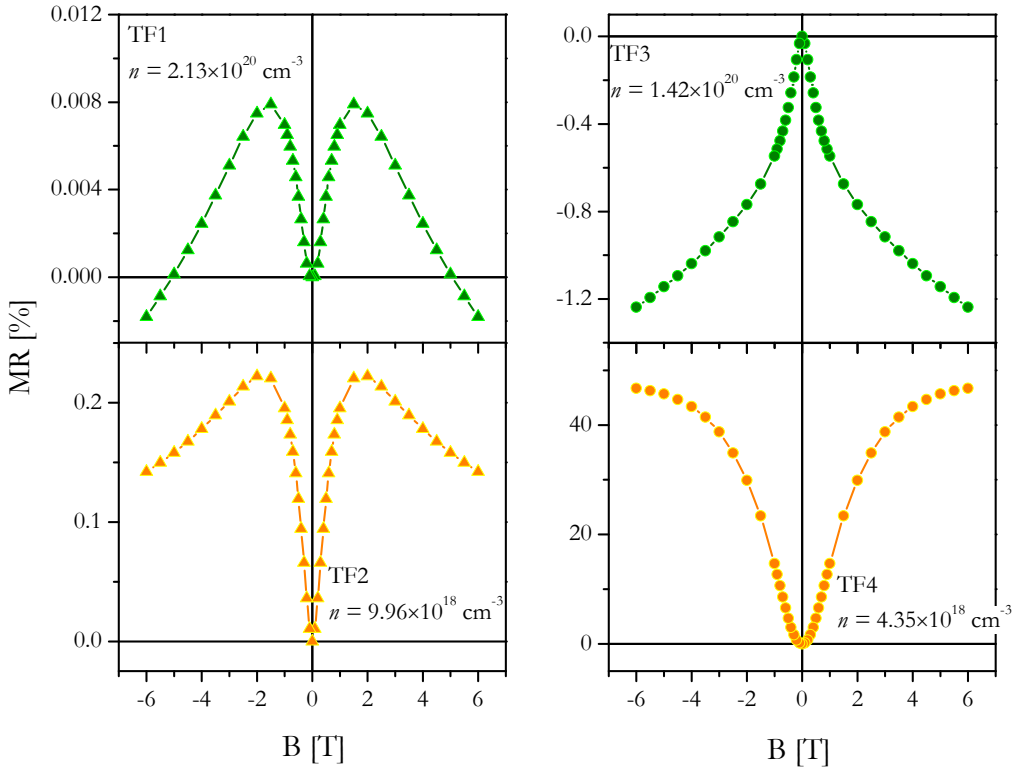

Fig. 7.1. Field dependent magnetoresistance measured at 5 K, for the Mn doped ZnO films on the left, and the Co doped ZnO films on the right.

A possible ferromagnetic response of charge carriers in ferromagnetic semiconductors is the anomalous Hall effect (AHE). The measured Hall curves after subtracting the ordinary Hall term (see section 4.4) are given in Fig. 7.2. In order to eliminate any magnetic field effects which are an even function of field, *i.e.*, MR, a simple subtraction was used $\varrho = 1/2[\varrho(B) - \varrho(-B)]$. The Mn doped films and the Co doped film with the larger n show no AHE. Nevertheless, the Co

doped film with the lower n (TF4) shows an AHE at 5 K, revealed by the pronounced s-shaped curve. This may be an indication of intrinsic ferromagnetism, although the observed AHE does not uniquely prove ferromagnetism [Xu (2008c)].

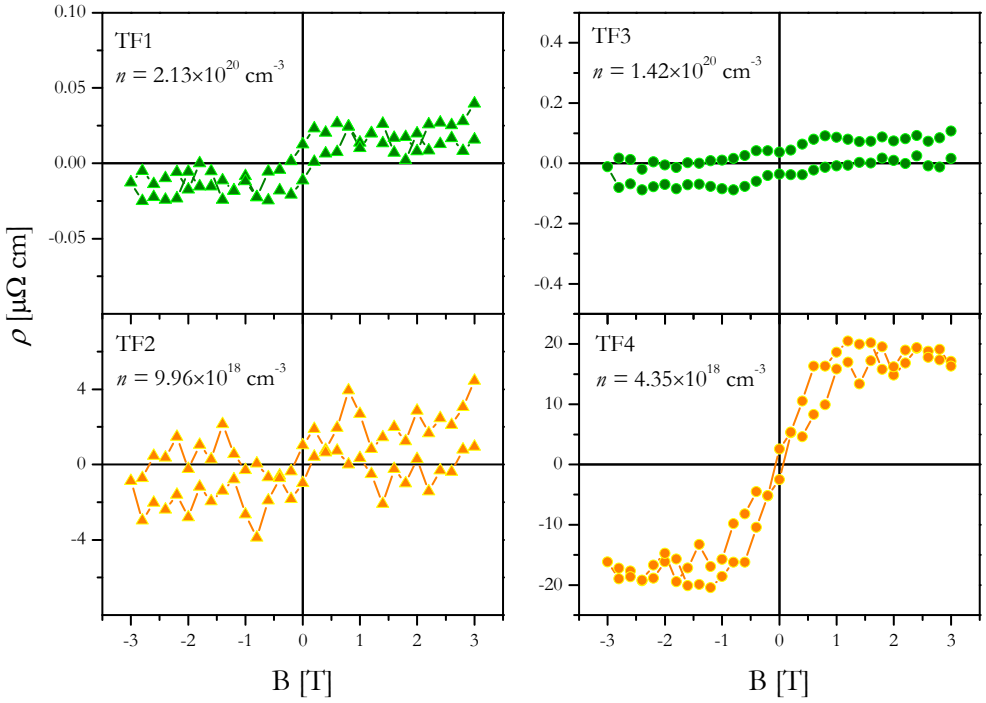

Fig. 7.2. Hall resistivity (after the subtraction of the ordinary Hall contribution) at 5 K as a function of the applied magnetic field, for the Mn doped ZnO films on the left and the Co doped ZnO films on the right.

The electron magnetic resonance (EMR) is a unique method to clarify the incorporation of transition (TM) ions into semiconductor hosts. Figs. 7.4 and 7.5 show the angular dependences of the X-band EPR signals at low temperature for the Mn and the Co doped ZnO films, respectively. θ is the angle between the applied magnetic field and the c axis of the ZnO films, hence $\theta = 0^{o}$ corresponds to the magnetic field perpendicular to the film surface. For the Mn doped ZnO thin films, only an unresolved approximately isotropic electron paramagnetic resonance (EPR) signal near $g = 2$ was detected. This signal corresponds to the spectrum of ZnO with a high content of paramagnetic substitutional Mn^{2+} ions on Zn sites. Conversely, in the case of the Co doped ZnO, the paramagnetic signal of substitutional Co^{2+} was not found. This result can be associated either to the absence of substitutional paramagnetic Co^{2+} due to

some type of Co agglomeration or to the position of the Fermi level, and could be clarified by means of XPS measurements, which are underway. On the other hand, an unusual broad signal with $g_{eff} > 2$ was detected at low temperature. This signal is more intense and further broadened with the increase of the electron concentration in the Co doped films. The signal intensity is be related to the film thickness which is one order of magnitude smaller in sample TF3. For both Co doped films, the signal is quenched at around 12 K, as illustrated in Fig. 7.5. The angular dependence of the line position is plotted in Fig. 7.6. This w-shaped angular dependence is typical of ferromagnetic resonance (FMR) measured in magnetic films [Vonsovskii (1966)]. The fact that the angular dependence shown in Fig. 7.6 lies entirely below the resonance field corresponding to paramagnetic resonance with $g = 2$ ($B \approx 3.48$ mT in the X-band) can be caused by two reasons: i) the magnetization at the resonance field is not saturated (see Fig. 7.7), and in this case the usual FMR theory [Vonsovkii (1966)] is not applicable; and ii) we suggest that we observe the spectrum not of a continuous magnetic film, but that of a heterogeneous distribution of the Co ions, composed by Co enriched and Co poor regions (spinodal decomposition), exhibiting a residual texture. Note that an ideal powder FMR spectrum is obtained from the integration of the spectra of the individual crystallites in the same manner as the EPR powder spectrum, as discussed in section 3.1.9. Verdes *et al.* (2001) performed Monte Carlo simulations including dipolar and exchange interactions among randomly distributed particles. The authors demonstrated that the exchange effects always lower the observed resonance field, sometimes appreciably.

Our observations of some kind of ferromagnetic order in Co doped ZnO films is in agreement with the results of Xu *et al.* (2008a) which demonstrate the spin polarization through the measurement of tunnelling MR at 5 K in magnetic tunnel junctions based on Co doped ZnO. On the other hand, very recent calculations by Raebiger *et al.* (2009) employing a band-structure-corrected theory show that Co doped ZnO is a possible DMS, but only under extreme donor doping conditions (≈3%). This condition may be achieved in our samples only locally due to fluctuations of the conduction band, but this would be in accordance with the previous discussion of the angular dependence of the FMR spectra. Additionally, we found no FMR related to Co clusters, as measured by von Bardeleben *et al.* (2008).

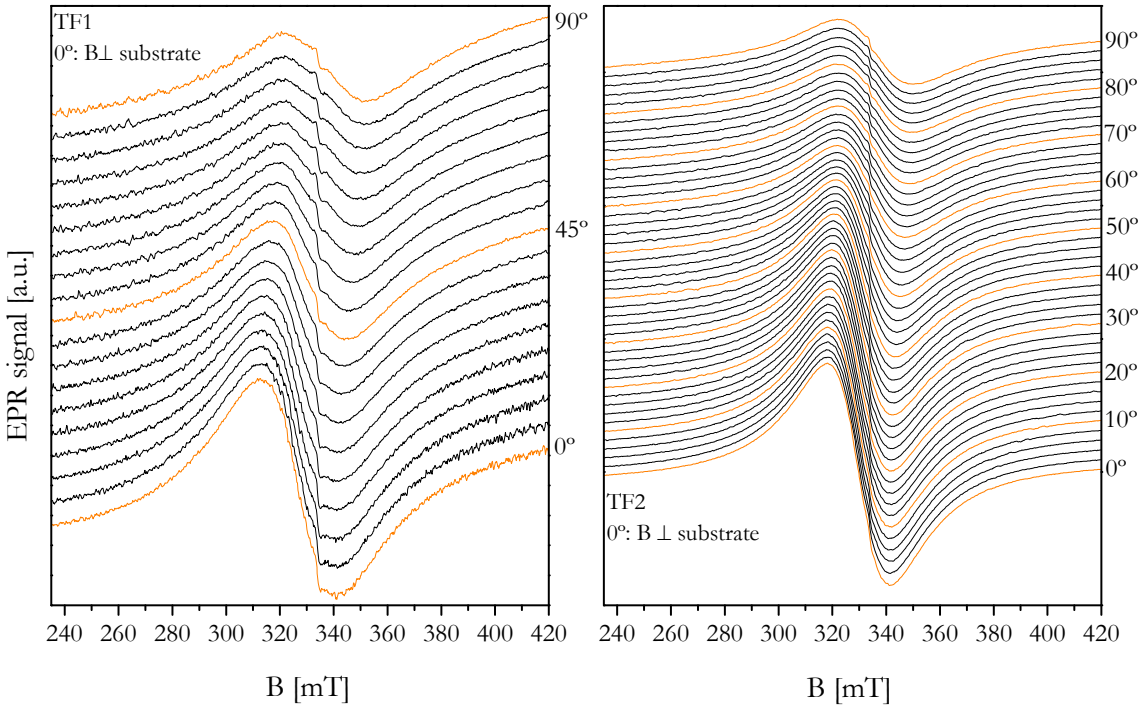

Fig. 7.3. Angular dependence of the EPR signal measured in the X-band at 4.4 K, for the Mn doped ZnO thin films.

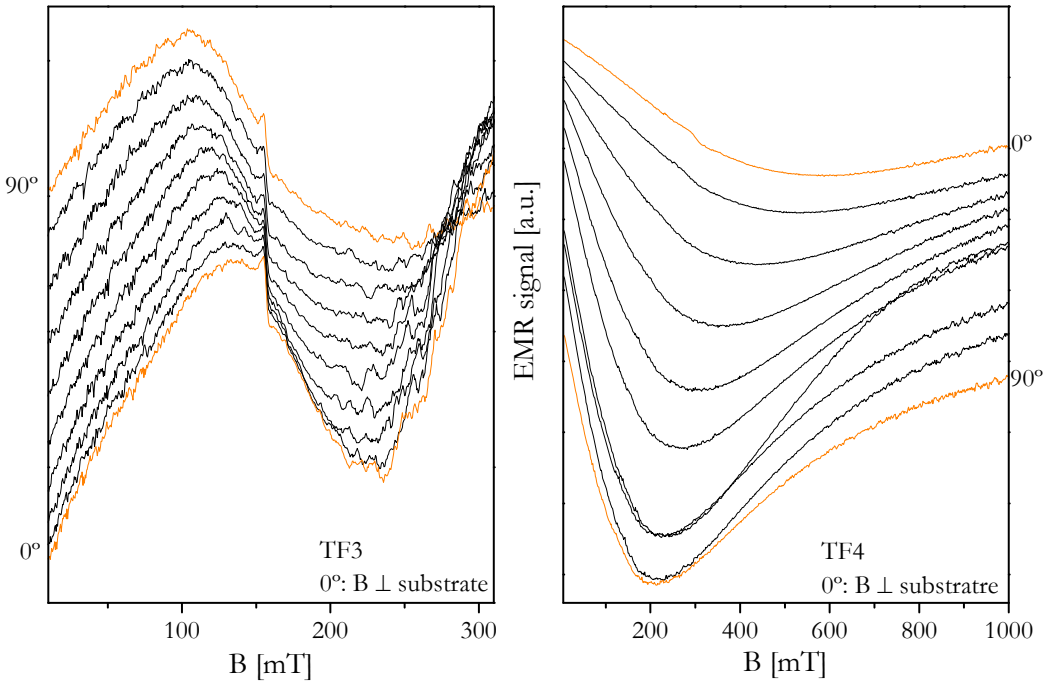

Fig. 7.4. Angular dependence of the EMR signal measured in the X-band at 4.3 K, for the Co doped ZnO thin films.

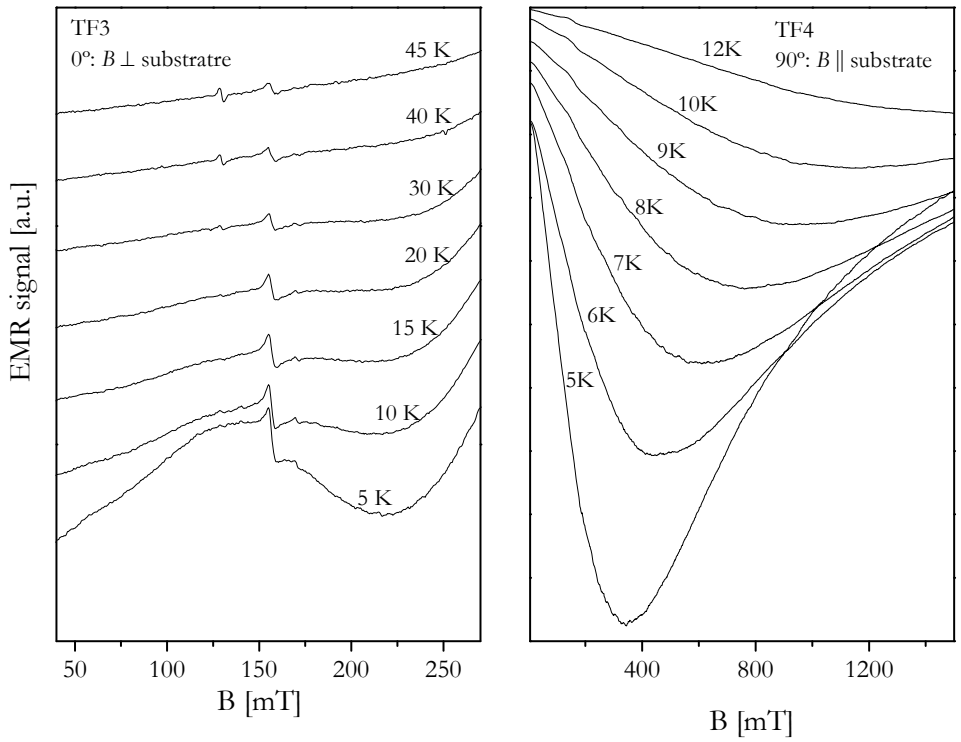

Fig. 7.5. Temperature dependence of the EMR signal measured in the X-band, for the Co doped ZnO thin films.

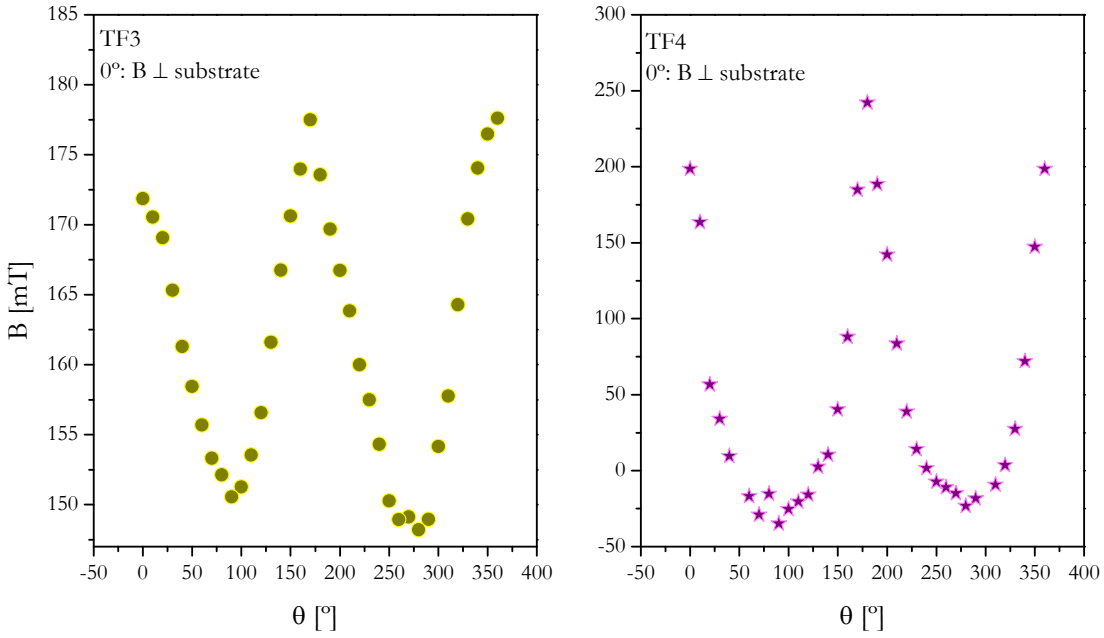

Fig. 7.6. Angular dependence of the line position of the EMR signal measured in the X-band at 4.3 K, for the Co doped ZnO films.

To further clarify the magnetic properties of the Co doped films, we used SQUID measurements. The results are represented in Fig. 7.7. Hysteresis loops were recorded for both Co doped films at 5 K. Sample TF3 shows insignificant hysteresis and only at low temperature. On the other hand, sample TF4 exhibits weak ferromagnetism at 5 K. At 300 K sample TF4 shows no hysteresis anymore. For this sample, the temperature-dependent magnetization was recorded under field cooling (FC) and zero field cooling (ZFC) conditions.

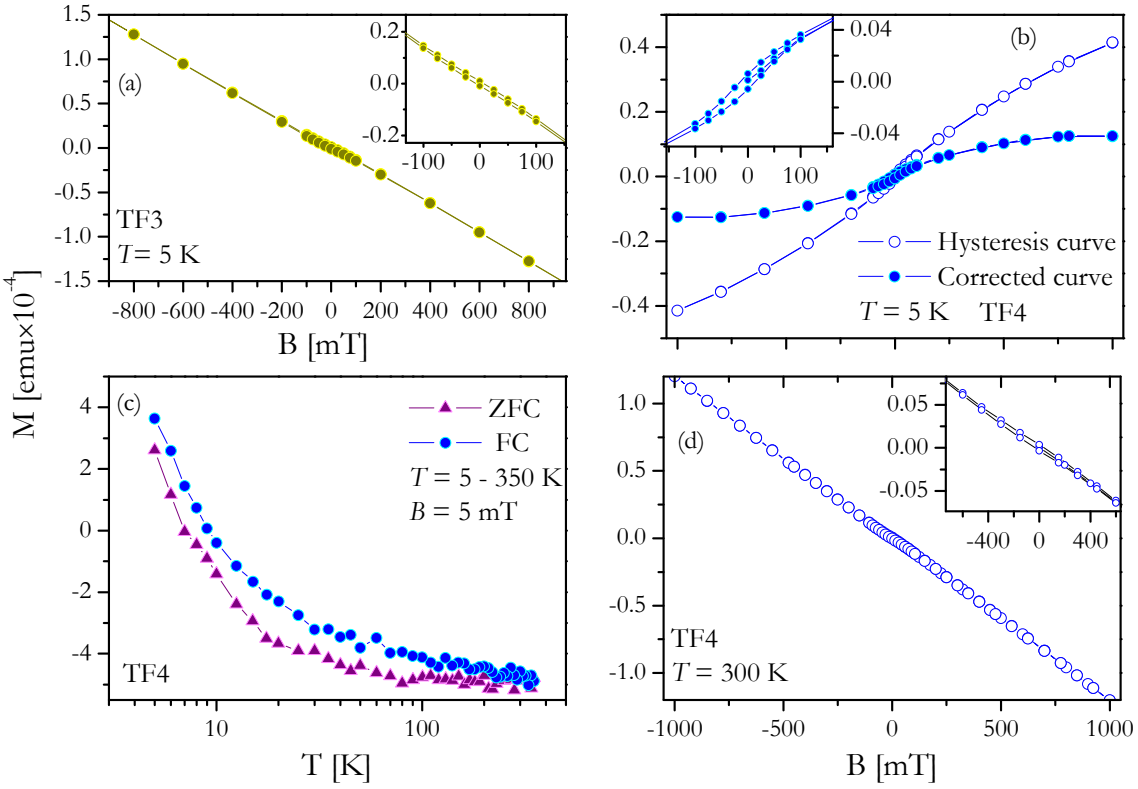

Fig. 7.7. Low temperature hysteresis loops for the Co doped ZnO films with (a) high and (b) low electron concentrations. (c) Zero field cooling (ZFC) and field cooling (FC) magnetization curves measured with 5 mT on the Co doped ZnO film with the lower electron concentration. (d) Room temperature hysteresis loop for the Co doped ZnO film with the lower electron concentration.

The subtraction of ZFC from FC data eliminates para- and diamagnetic contributions. Simultaneously, a nonzero difference indicates the presence of hysteresis, *i.e.*, ferromagnetic ordering, if the measuring field is lower than the maximum field at which hysteresis is observed, as in the present case. From the temperature dependence of the FC and ZFC curves it can also be excluded that the nonzero difference between FC and ZFC is due to spin-glass ordering or superparamagnetism, since neither a kink or blocking temperature is observed in the curves.

The overall magnetic properties show no evidence of carrier mediated ferromagnetism, since the sample exhibiting larger magnetic order is the one with lower carrier concentration.

7.3 XRD MEASUREMENTS

The magnetic measurements point to some kind of ferromagnetic order in the Co doped thin films. In order to further clarify the origin of the found magnetic properties, XRD measurements were performed in the θ - 2θ geometry. The XRD patterns, shown in Fig. 7.8, were collected from 30º to 90º with a step size of 0.01º for 2 s per step. Additionally, the pole figures given in Fig. 7.9 were performed around the $CoAl_2O_4$ (440) and $CoAl_2O_4$ (224) directions. A higher resolution beam collimated with a 2 bounce Ge (220) monochromator was used in order to collect the symmetric reciprocal space maps (RSMs), given in Fig. 7.10.

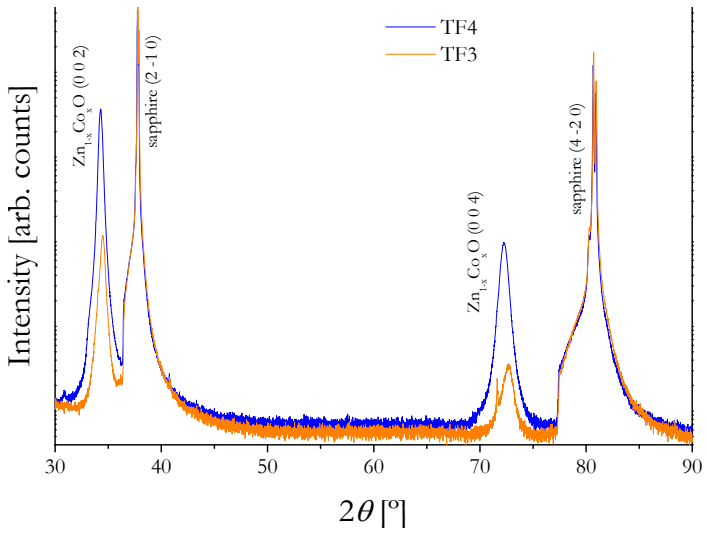

Fig. 7.8. X-ray diffraction patterns of the Co doped ZnO films with different electron concentrations. The diffraction peaks are identified for each structure by the Miller indices of the planes.

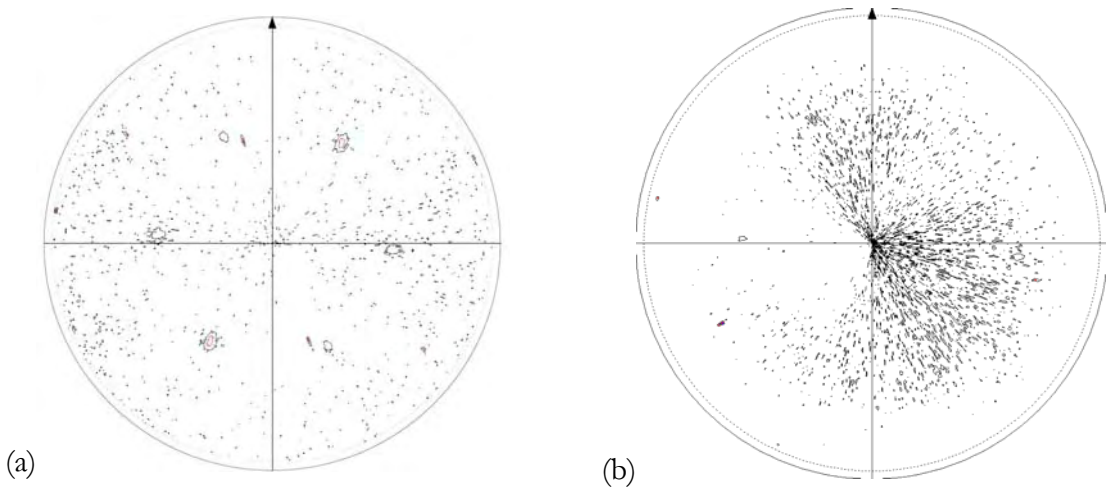

Fig. 7.9. Pole figures around (a) (440) $CoAl_2O_4$ and (b) (224) $CoAl_2O_4$, for the Co doped film TF4.

The 2θ-θ diffractograms (Fig. 7.8) show that the $Zn_{1-x}Co_xO$ films have a monocrystalline structure with the ZnO (001) crystallographic planes aligned with the sapphire (2-10) planes for both samples. Furthermore, despite an especial effort to find metallic Co nanocrystals (like in Ref. [Coey and Chambers (2008)]), no corresponding peaks were detected, although it does not mean that they are absent.

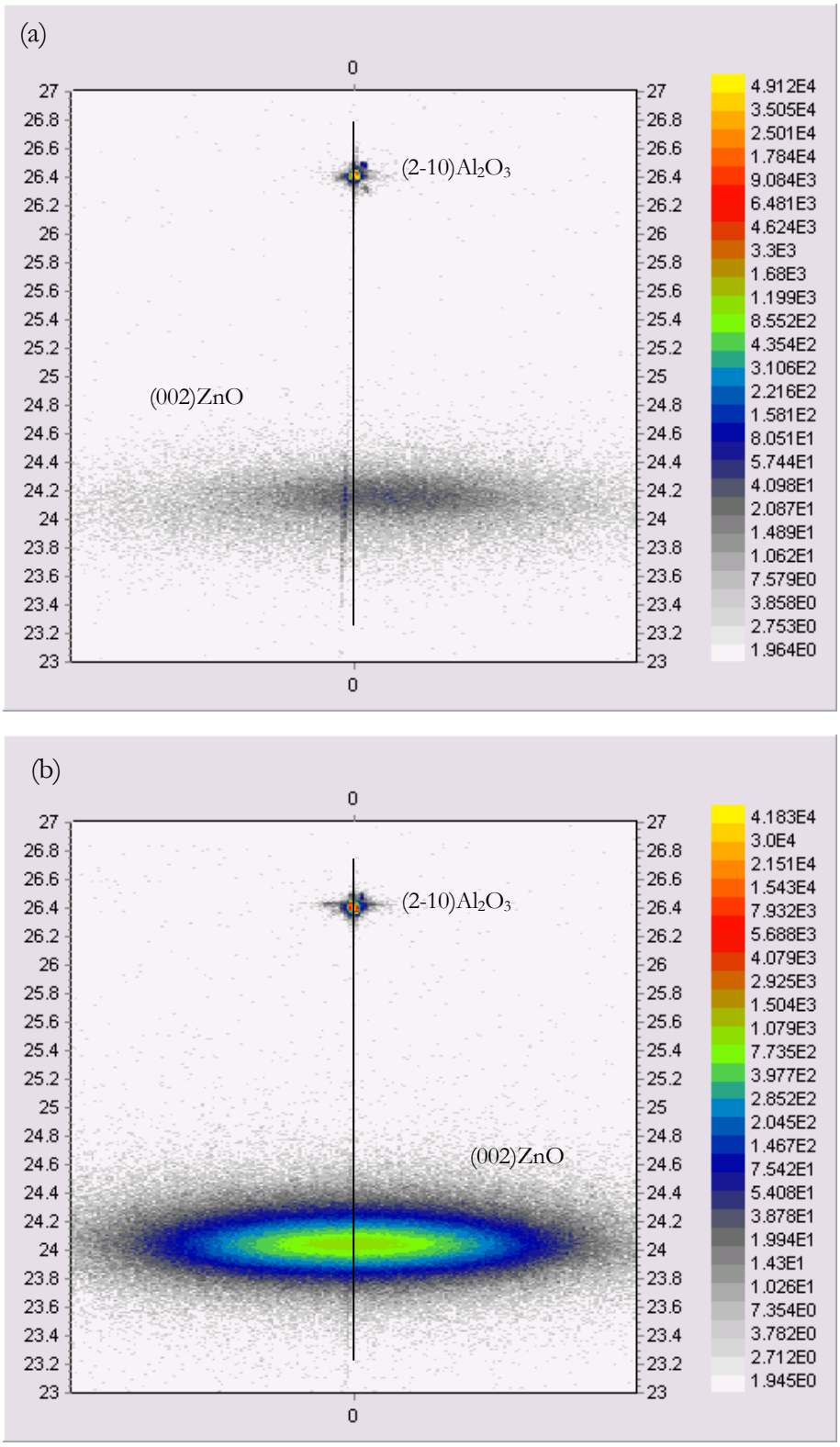

Fig. 7.10. Reciprocal space maps of samples (a) TF3 [(002)ZnO + (2-10)Al_2O_3] and (b) TF4 [(002)ZnO + (2-10)Al_2O_3].

The pole figures around (440) and (224) reflections show no evidence of a second phase. The RSMs indicate that there is a slight angular deviation between the (002) ZnO and the (2.10) Al_2O_3 planes for sample TF4, while no deviation was observed for sample TF3. Moreover, the *c* lattice parameter was determined through the RSMs to be 5.2267 Å sample TF3, and 5.1986 Å sample TF4, indicating an expansion of the ZnO lattice upon the increase of the Co concentration.

The fact that no evidence of second phase precipitates was found supports our interpretation of the magnetic properties arising from spinodal decomposition.

7.4 Concluding remarks

The magnetic and structural properties of Mn and Al or Co and Al co-doped ZnO films grown by PLD were investigated. The Mn doped ZnO samples were clearly paramagnetic, the Mn ions being substitutional on Zn sites, as revealed by the EPR measurements. On the other hand, the EPR signature of substitutional Co^{2+} on Zn sites was not found in the Co doped samples. Instead, a resonance signal with $g_{eff} > 2$ was recorded, which behaves as FMR in the case of non-saturated magnetization. Also, the MR, the Hall effect, and the SQUID measurements point to some kind of ferromagnetic order in the Co doped samples. A first glance of the results may make one think about carrier mediated ferromagnetism. Nevertheless, we believe that the formation of small precipitates, second phases, or spinodal decomposition is the origin of the weak observed ferromagnetism, since the Co content is very large and the EPR investigations clearly show that the Co is not mainly incorporated as substitutional Co^{2+} in the ZnO lattice. Hence, we found no clear evidence of carrier mediated ferromagnetism in our co-doped samples. Measurements of the XPS are underway to clear the valence state of the Co atoms (ions).

8 Fe alloyed ZnO films

In this chapter, Fe alloyed ZnO thin films deposited by pulsed injection metalorganic chemical vapour deposition (PIMOCVD), using different Fe concentrations, are investigated by means of different techniques in order to further clarify the role of secondary phases in the occurrence of ferromagnetism.

8.1 Sample preparation

Iron alloyed ZnO thin films were grown by R. P. Borges at the University of Lisbon on sapphire (0001) substrates by PIMOCVD [Sénateur (2000)]. Solid precursors were dissolved in an organic solvent (monoglyme) forming a solution that was kept at room temperature in order to avoid the thermal decomposition of the precursors. An electrically driven valve allowed the controlled injection of small droplets of the solution into the reactor. The injected droplets were flash vaporized forming a stable gas-phase composition that was carried by a stream of Ar and O_2 towards a heated substrate (550 ºC) where the deposition took place. After the deposition the films were slowly cooled down to room temperature in 1 bar of oxygen. In this work, a single solution containing the Zn and Fe precursors was used for each film. By changing the fraction of Fe precursor in the solution (Fe/(Zn + Fe)), from 0 to 0.35, films with different nominal Fe alloying were obtained.

The films thickness was determined using a single-wavelength ($\lambda = 632.8$ nm) ellipsometer. The obtained values for the sample series lie in the range 50-60 nm, as expected from the deposition conditions [Sénateur (2000)].

8.2 Structural characterization

The Fe content (x = Fe/(Zn + Fe)) of the grown films was estimated by energy dispersive X-ray spectroscopy (EDS). The determined values were generally higher than those of the precursor solution used for each film, and were also higher than the reported solubility limits for Fe in ZnO [Jin (2001), Mandal (2006)]. The correspondence between the Fe content in the films and in the precursor solution, shown in Fig. 8.1 (a), indicates that under the used growth

conditions the deposition rate for Fe was larger than for Zn for solution concentrations higher than 0.25. In the discussion below all values of Fe content refer to the determined EDS values.

The films texture was analysed by X-ray diffraction (XRD) in the θ - 2θ geometry. XRD patterns of the full series of films are shown in Fig. 8.1 (b).

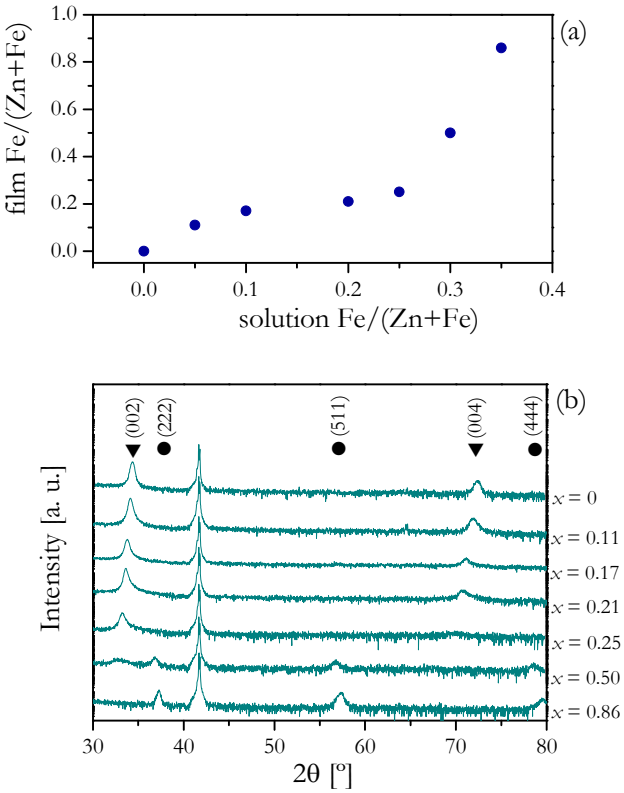

Fig. 8.1. (a) The correspondence between the Fe content in the precursor solution and in the films, measured by energy dispersive X-ray spectroscopy. (b) XRD plots for the series of ZnO films with different Fe concentrations. The diffraction peaks are indicated by the symbols ▼ for the ZnO wurtzite structure and ● for both $ZnFe_2O_4$ and Fe_3O_4. Miller indices of the planes are indicated for each structure.

For Fe contents ranging from $x = 0$ to $x = 0.25$ only the (002) and (004) planes of the wurtzite lattice could be observed indicating that the films are well textured with the *c*-axis of ZnO perpendicular to the plane of the film and with the *c* lattice parameter increasing with Fe content. For $x = 0.50$ the wurtzite peaks almost disappear, and a new set of peaks identified as belonging to spinel structures appear. The observed broad peaks could be attributed to both $ZnFe_2O_4$ and Fe_3O_4, as shown in Fig. 8.1 (b), given that both compounds have a face centred cubic (fcc) structure and similar lattice parameters (a = 0.8441 nm for $ZnFe_2O_4$ [JCPDS 22-

1012] and $a = 0.8396$ nm for Fe_3O_4 [JCPDS 19-0629]). The sixfold symmetry of both sapphire and ZnO imposes a [111] texture in these phases as the fcc structure is also sixfold symmetric along that direction. With increasing x from 0.5 to 0.86, the (222), (333) and (444) peaks shift to higher θ values, which might indicate that the volume fraction of Fe_3O_4 becomes dominant over that of the $ZnFe_2O_4$ phase upon the increase of the Fe content.

8.3 MAGNETIC PROPERTIES

The temperature dependence of the magnetization M was measured after zero-field cooling (ZFC) and field cooling (FC) procedures for temperatures between 5 and 400 K. The ZFC and FC magnetization curves for an applied field of 50 mT after removal of the diamagnetic component of sapphire are shown in Fig. 8.2. For samples with $x \geq 0.21$ the results evidence the onset of a low temperature antiferromagnetic phase as observed from the downturn in both ZFC and FC magnetization curves near 10 K. This transition is still observed for the sample with $x = 0.50$ while for the higher concentration value, $x = 0.86$, this feature is not detected and the curves display a spin-glass like behaviour with a large irreversibility, corresponding to the difference between the ZFC and FC curves at low temperatures. For the whole sample series the low temperature magnetic moment increases with increasing x, and the magnetic signal persists up to 400 K, even for the films with the lowest doping values.

The hysteresis loops performed at 300 K for the films with $x = 0.11$, 0.21 and 0.25 (which show only the wurtzite phase in the X-ray diffraction pattern) are shown in Fig. 8.3. The results confirm the existence of ferromagnetism at this temperature and evidence a magnetic signal that increases with x. In the case of $x = 0.86$, the coercive field is only about 40 Oe, while for all other films in this sample series the coercivities lie in the range 120 - 170 Oe, suggesting a different magnetic phase.

The overall magnetic behaviour of the films can be understood as due to the presence of $ZnFe_2O_4$ and Fe_3O_4 inclusions. In the spinel $ZnFe_2O_4$, the oxygen ions form a close-packed fcc structure with the Zn^{2+} and Fe^{3+} ions occupying either tetrahedral A or octahedral B interstitial sites (see Fig. 8.4). In the normal spinel the Zn^{2+} ions, with zero magnetic moment due to the $3d^{10}$ orbital configuration, occupy the tetrahedral sites, and the Fe^{3+} ions are in octahedral sites. Due to the superexchange interaction between Fe^{3+} ions in octahedral sites [Schiessl (1996)] the

normal spinel $ZnFe_2O_4$ is antiferromagnetic with a Néel temperature of $T_N = 10$ K. The low temperature transition observed in Fig. 8.2 (a) for the samples with x up to 0.50 can be explained by considering the presence of this normal spinel phase. For $x = 0.86$ the kink at 10 K disappears in agreement with the predominance of a different magnetic phase.

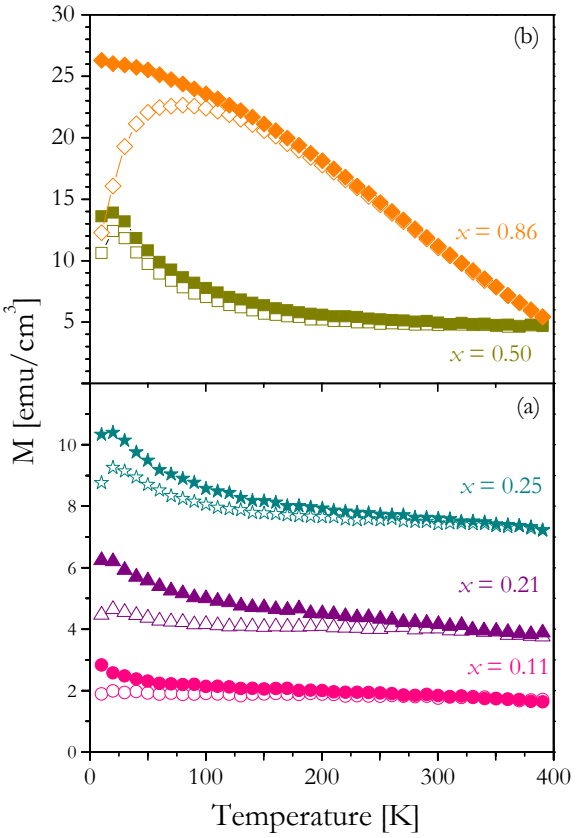

Fig. 8.2. Zero field cooling (ZFC) (empty symbols) and field cooling (FC) (full symbols) magnetization curves measured with 50 mT for (a) Fe alloyed ZnO films where only ZnO XRD peaks are visible, and for (b) films where the XRD shows the presence of the $ZnFe_2O_4$ or Fe_3O_4 phases.

Furthermore, it is well known that the increase of Fe content in the normal spinel $ZnFe_2O_4$ leads to the formation of spinel structures with different degrees of inversion. In these structures the strong interaction between Fe^{3+} ions in octahedral and tetrahedral sites results in a ferromagnetic signal that can persist above room temperature. Moreover, as observed in the XRD results, the higher Fe deposition rate in the case of high Fe precursor solution concentration (see Fig. 8.1) leads to the formation of a predominant Fe_3O_4 phase for the films with $x \geq 0.50$, even if the occurrence of this phase for the low Fe content films cannot be

excluded. Fe_3O_4 is ferrimagnetic with a transition temperature of 858 K and a high magnetization value at room temperature. Thus, the presence of the iron oxide and of the inverted spinel zinc ferrite can account for the observed room temperature hysteresis loops.

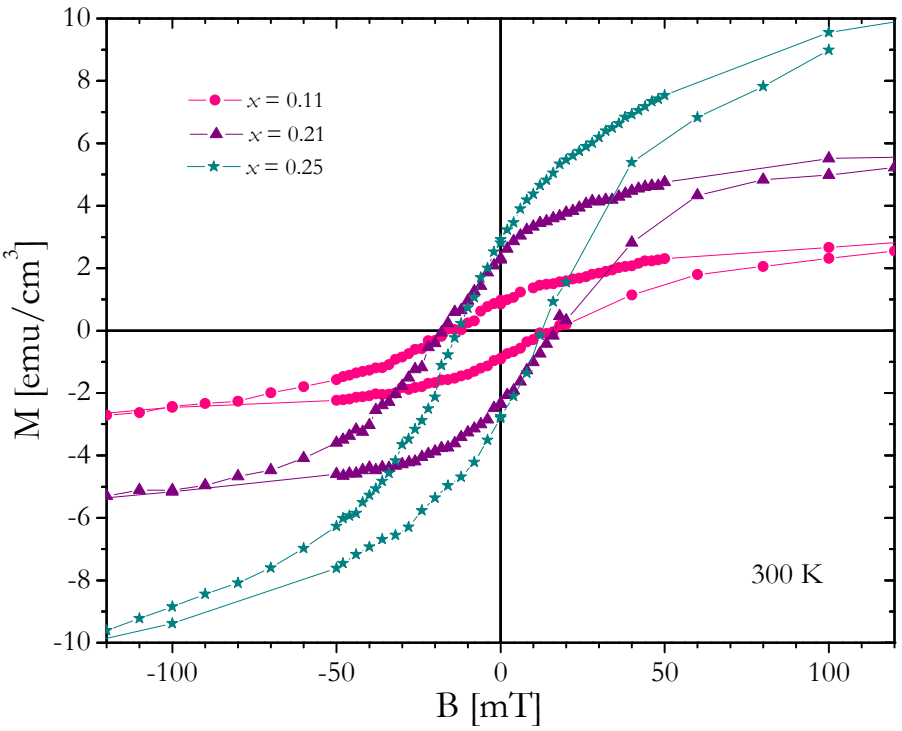

Fig. 8.3. Room temperature hysteresis loops for films which only exhibit ZnO XRD peaks.

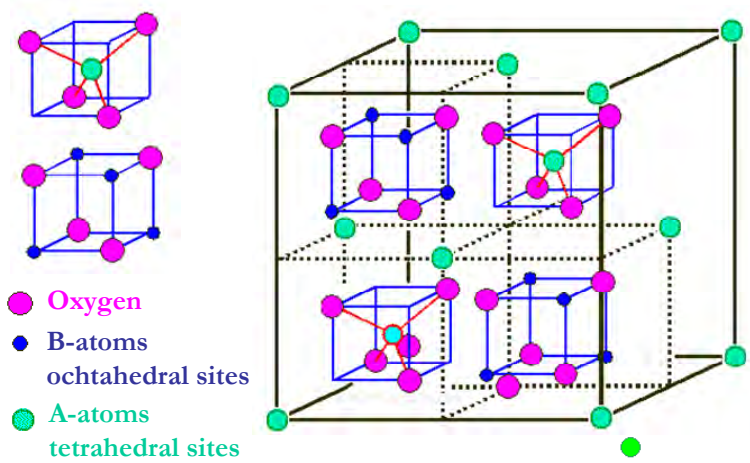

Fig. 8.4. AB_2O_4 spinel crystal structure. The blue cubes are also contained in the back half of the unit cell.

For the highest Fe content film $x = 0.86$, the presence of Fe_3O_4 also explains the detected large fraction of Fe, since if we were to consider the Zn ferrite phase alone the value of x should be only 0.66. In this case, the coexistence of antiferromagnetic and ferromagnetic exchange couplings can explain the spin-glass like behaviour illustrated in Fig. 8.2 (b). The saturation magnetization value of 39 emu.cm^{-3} obtained for this sample at $T = 10$ K is about one order of magnitude smaller than the values reported for the $ZnFe_2O_4$ inverted spinel [Philip (2007)] and for Fe_3O_4 [Horng (2004)]. Two aspects concur for the low observed values. First, there is a clear underestimation of the saturation magnetization, since this value is determined using the total film volume instead of the (unknown) volumes associated with each spinel phase. Secondly, the degree of inversion of the $ZnFe_2O_4$ spinel, not controlled in this experiment, is not accounted for in the calculations.

To further clarify the magnetic properties of this material, ferromagnetic resonance (FMR) was used as a selective probe, in particular to determine the magnetic anisotropy parameters of the magnetic phases. The out-of-plane angular dependences for $x = 0.21$, 0.25, 0.86 are given in Figs. 8.5, 8.6, and 8.7, respectively. The temperature dependence of the FMR signal, tracked for temperatures up to 400 K, was measured both for magnetic field perpendicular and parallel to the sample surface plane, $B \parallel c$ ($\theta_B = 0^\circ$) and $B \perp c$ ($\theta_B = 90^\circ$ or 270°), respectively, in the temperature range $4 \leq T \leq$ (300 or 400) K. For the samples with $x < 0.21$, a weak (for $x = 0.11$) or no (for $x = 0.17$) FMR signal was found. For higher Fe contents ($x \geq 0.21$) reasonable FMR signals were observed, especially at room temperature. The intensity of these signals grew with increasing percentage of Fe. In-plane and out-of-plane angular dependences of the spectra were measured, and no in-plane anisotropy was found.

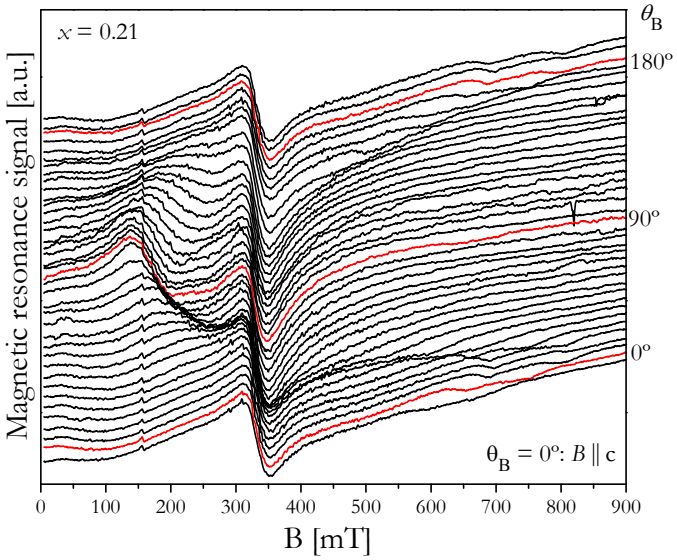

Fig. 8.5. Out-of-plane angular dependence of the FMR spectra taken at 150 K for the Fe alloyed ZnO films with $x = 0.21$.

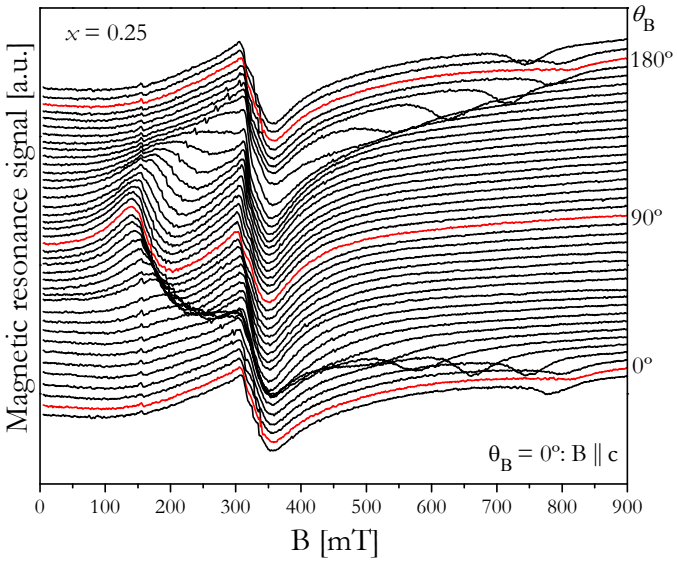

Fig. 8.6. Out-of-plane angular dependence of the FMR spectra taken at 150 K for the Fe alloyed ZnO films with $x = 0.25$.

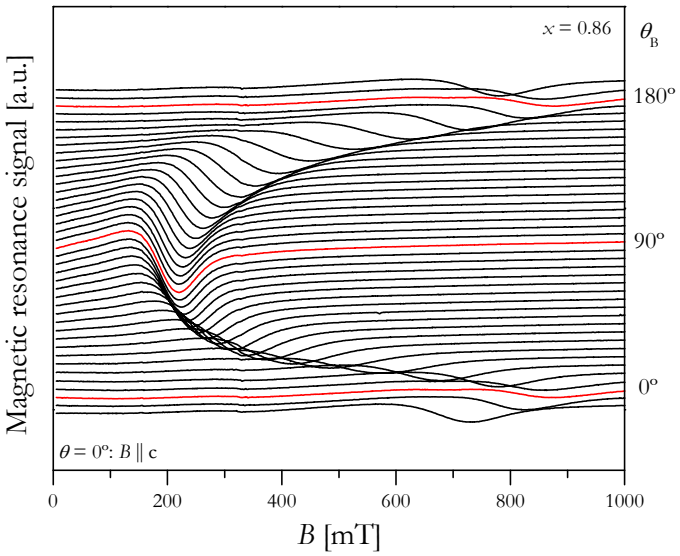

Fig. 8.7. Out-of-plane angular dependence of the FMR spectra taken at 150 K for the Fe alloyed ZnO films with $x = 0.86$.

The out-of-plane angular dependence of the resonance field for the main FMR bands observed in samples with different Fe concentrations was fitted by a non-linear algorithm that minimizes the free energy of the film under an applied field B. Within the model used for the determination of the magnetic anisotropy parameters [Lenz (2005)], the free energy of a thin film is given by:

$$E = -BM\left[\sin\theta\sin\theta_B + \cos\theta\cos\theta_B\right] - \left(2\pi M^2 - K_{2\perp}\right)\sin^2\theta - \frac{1}{2}K_{4\perp}\cos^4\theta\,, \qquad (8.1)$$

with the first term corresponding to the Zeeman energy, and the next two corresponding to the first and second order magnetocrystalline anisotropy energy, respectively. θ is the polar angle of the magnetization M with respect to the surface normal (c-axis of ZnO), and $K_{2\perp}$ and $K_{4\perp}$ are the first and second order out-of-plane anisotropy constants. As it is difficult to determine the true microscopic magnetization M of the ferromagnetic phase in the films, we limited ourselves to calculate the anisotropy fields $B_{a1} = 4\pi M - 2K_{2\perp}/M$ and $B_{a2} = 4K_{4\perp}/M$. The results of the fittings are illustrated in Figs. 8.8, 8.9, and 8.10. The g-factors and anisotropy fields obtained by our fittings are given in Table 8.1.

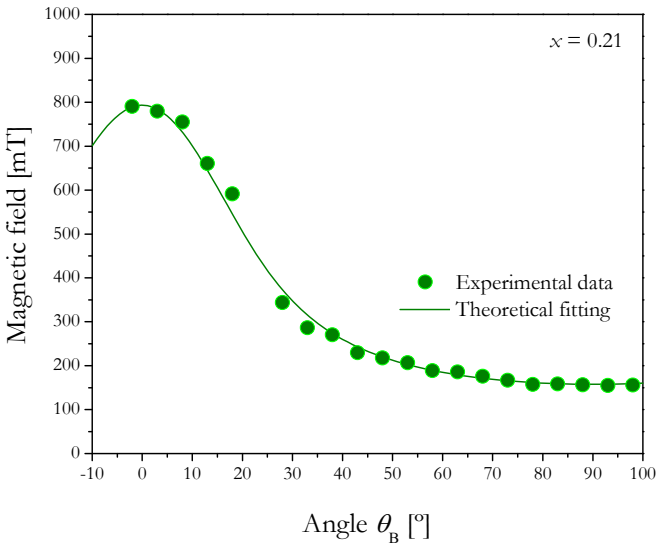

Fig. 8.8. Experimental data (dots) and theoretical fitting (line) of the out-of-plane angular dependence of the resonance field of the strongest band obtained by the evaluation of FMR spectra for the Fe alloyed ZnO films with $x = 0.21$ presented in Fig. 8.5.

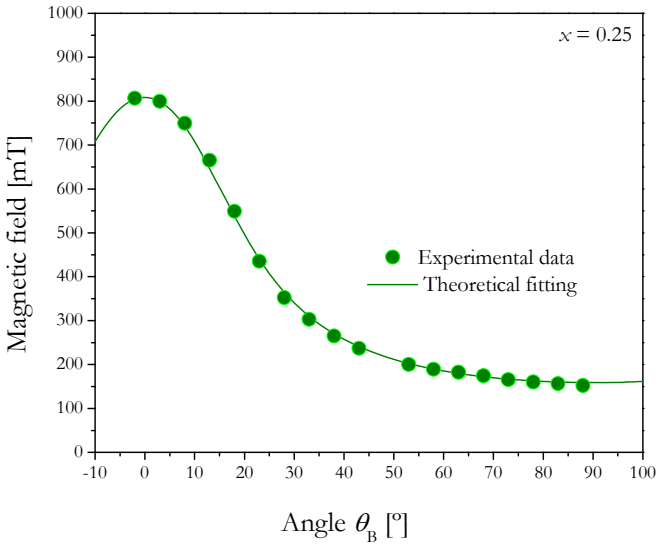

Fig. 8.9. Experimental data (dots) and theoretical fitting (line) of the out-of-plane angular dependence of the resonance field of the strongest band obtained by the evaluation of FMR spectra for the Fe alloyed ZnO films with $x = 0.25$ presented in Fig. 8.6.

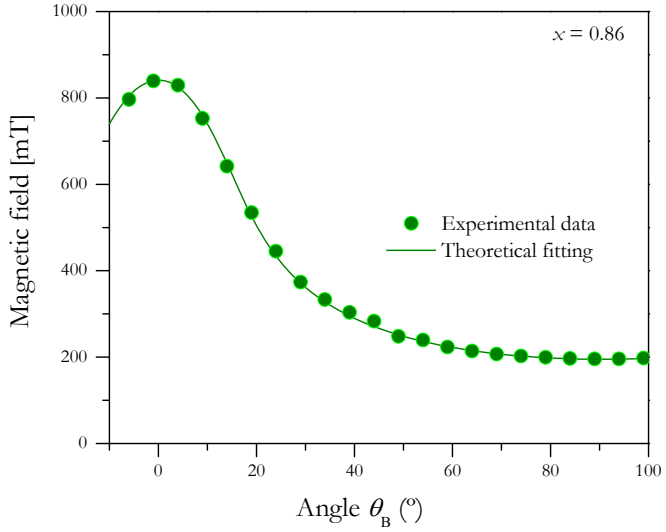

Fig. 8.10. Experimental data (dots) and theoretical fitting (line) of the out-of-plane angular dependence of the resonance field of the strongest band obtained by the evaluation of FMR spectra for the Fe alloyed ZnO films with $x = 0.86$ presented in Fig. 8.7.

Table 8.1. Anisotropy fields (in mT) and g-factor determined by the fitting of Eq. (8.1) to the experimental data taken at 150 K.

x	B_{a1}	B_{a2}	g
0.21	480 ± 10	30 ± 5	2.02 ± 0.05
0.25	490 ± 10	20 ± 5	2.03 ± 0.05
0.86	475 ± 10	–30 ± 5	1.93 ± 0.02

Let us first analyze the spectra of the $x = 0.86$ sample. There is a very good agreement between the fitting and the experimental data (see Fig. 8.10). The hard magnetization axis is perpendicular to the film plane and thus parallel to the c-axis of ZnO. As illustrated in Fig. 8.11, the FMR signal was tracked for temperatures up to 400 K. The analysis of the spectra of the samples with $x = 0.21$ and 0.25, shown in Fig. 8.5 and Fig. 8.6, reveals that the magnetic phase found in them differs from that detected in the $x = 0.86$ film. First, the temperature dependence of the resonance field is different (Fig. 8.11). Secondly, for $x = 0.21$ and 0.25 the g-factor is larger and the B_{a2} anisotropy field is positive and not negative as in the $x = 0.86$ case, see Table 8.1. (The B_{a1} field is equal in all three samples only by the merest chance, as the angular

dependences have been evaluated for T = 150 K, at which the line positions for $B \parallel c$ and $B \perp c$ coincide, see Fig. 8.11.)

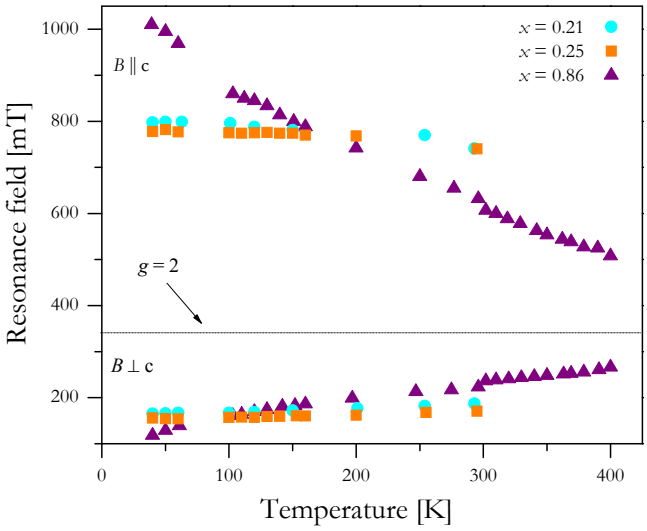

Fig. 8.11. Temperature dependence of the resonance fields of the strongest bands for the orientations $B \parallel c$ and B $\perp$ c for Fe alloyed ZnO films with three different x values. The measurements between 10 and 300 K and between 300 and 400 K were performed with two microwave cavities having slightly different resonance frequencies, which accounts for a small discontinuity of the curves for the x = 0.86 sample occurring at 300 K.

Importantly, for all films, the overall temperature dependence of the resonance field is compatible with the behaviour of the magnetization: for x = 0.86 it is stronger than for x = 0.21 and 0.25 (cf. Fig. 8.2). When the field is applied parallel to the surface plane, the resonance field increases with temperature, and the opposite occurs when the field is applied perpendicular to it, as shown in Fig. 8.11. Thus, the resonance fields approach the value of the paramagnetic resonance with g = 2 as the temperature increases towards the Curie point. This means that the values of the saturation magnetization and/or magnetic anisotropy constants decrease with rising temperature.

It is noteworthy that other, weaker resonance bands could be observed in the spectra of the samples with Fe contents of x = 0.21 and x = 0.86. The observation of such bands indicates the existence of other magnetic phases or of the same phases as those responsible for the main resonance bands but in different states of strain (*e.g.*, relaxed and non-relaxed).

The values obtained by us for the *g*-factor are smaller than those known for bulk Fe ($g = 2.09$) [Landolt-Boernstein (1986)] and single crystalline Fe_3O_4 ($g = 2.12$) [Kale (2001), van der Heijden (1998)]. This result may be related to the fact that the Fe alloyed ZnO system is not homogeneous, so that the orbital momentum of the Fe ions is not completely quenched [Sénateur (2000)]. Castel *et al.* [Castel (2007)] observed, *e.g.*, that the gyromagnetic ratio γ (which is proportional to *g*) decreases as the concentration of Ni in ZnO increases. This might validate our *g*-factor value. We could not find any FMR data on single-crystalline $ZnFe_2O_4$ in the literature in order to make a comparative analysis.

Zhang *et al.* (2006) investigated amorphous inhomogeneous magnetic Fe alloyed ZnO semiconductors with average Fe concentrations in the range from 62% to 86% synthesized by alternately sputtering of Fe and ZnO layers under thermal non-equilibrium conditions. Their results for the anisotropy fields are very similar to ours.

8.4 Concluding remarks

ZnO films alloyed with Fe at concentrations above the reported solubility limit (≈2.2 mol% [Fukumura (2001)]) were grown by PI-MOCVD. For the lower Fe contents ($x \leq 0.25$) the X-ray diffractograms show only peaks associated with the ZnO wurtzite structure, while for $x > 0.25$ peaks related to the fcc spinel structure appear. All samples exhibit ferromagnetic hysteresis loops at 300 K, and for the films with iron content $x \leq 0.50$ the temperature dependence of the magnetization shows an antiferromagnetic transition at 10 K attributed to the presence of the normal spinel $ZnFe_2O_4$ phase. FMR measurements confirm the existence of a ferromagnetic behaviour at temperatures at least up to 400 K, which is compatible with the presence of both Fe_3O_4 and the inverted $ZnFe_2O_4$ spinel formed in the ZnO layers. The intensity of the FMR signal increases with increasing Fe content. Between $x = 0.50$ and $x = 0.86$ a change of the magnetic phase occurs, leading to a different behaviour of the magnetization vs. temperature and to the appearance of a new FMR spectrum.

In conclusion, our results support the indication that secondary phases, not detected by standard XRD, are accountable for the magnetic behaviour detected in many transition metal alloyed ZnO systems in contrast to the assumption of being in the presence of an intrinsic diluted ferromagnetic system.

9 SUMMARY AND OUTLOOK

This work focuses on the study of the promising ZnO wide band gap semiconductor, doped with different transition metals for applications in spintronic devices. The investigations carried out in the framework of this thesis demonstrate that the initial optimism over achieving a diluted magnetic semiconductor (DMS) based on ZnO, derived from theoretical predictions which prompted research all over the world, was somewhat misleading, since no experimental evidence of a net ferromagnetic effect due to the diluted magnetic ions was found. Nevertheless, through this research we have learned more about this material system, which can be realized in different structures by several techniques, and may be used for different applications.

In this thesis, detailed investigations of the structural and magnetic properties of ZnO based structures, namely nanowires (NWs), nanocrystals (NCs), and thin films, were carried out. Transition metal ™ ions, specifically Co, Mn and Fe, were introduced in these structures during growth. Several growth methods were used. TM doped ZnO NWs and thin films were grown by pulsed laser deposition (PLD), TM doped ZnO colloidal NCs were synthesized by a wet chemical process, and Fe alloyed ZnO films were grown by pulsed injection metalorganic chemical vapour deposition (PIMOCVD). Various experimental techniques, such as x-ray diffraction (XRD), scanning electron microscopy (SEM), transmission electron microscopy (TEM), electron paramagnetic resonance (EPR), SQUID, and transport measurements were employed to structurally and magnetically characterize these samples.

The investigations of the Mn and Co doped ZnO NWs grown by PLD revealed that the TM ions were mainly incorporated as substitutional isolated Mn^{2+} ($3d^5$, ^6S) or Co^{2+} ($3d^7$, ^4F), respectively. Moreover, in the case of the Co doped NWs it was possible to identify two different components of the EPR spectrum, A and B, which were ascribed to two different environments of the Co ions. Additionally, the temperature dependence of the EPR intensity showed that both components exhibit pure paramagnetic behaviour.

In the case of the ZnO colloidal NCs, both Mn and Co ions were successfully incorporated, yielding the EPR spectra of isolated Mn^{2+} or Co^{2+}, respectively, on Zn sites. For both types of doping, the TM incorporation was heterogeneous in the sense that the EPR spectra were composed partly of a signal stemming from isolated substitutional TM ions on Zn sites, and partly of that coming from TM ions in distorted or TM enriched environments.

Furthermore, the relative intensities of the EPR spectra and the performed surface modifications showed that the NCs exhibit a core-shell structure. In addition, we were able to distinguish signals caused by locally distorted environment in the shell. Furthermore, we found that the TM ions incorporated in the NCs are subjected to a larger strain in comparison with bulk crystals, which is particularly reflected by the variation of the fine structure (FS) parameter *D*. In the case of the Mn doped NCs, we also show that the higher value for the hyperfine (HF) *A* constant found for the Mn^{2+} in the shell region can be explained with the formation of MnO_6 clusters in this part of the NCs. Moreover, our results evidence decreasing NC size and increasing lattice distortions for increasing Mn content. Finally, combining the measured intensities and line widths of the EPR signals produced by the Mn^{2+} in the core and the shell regions with a simple spherical core-shell model for the size of the NCs allowed us to determine the distribution of the manganese and the thickness of the shell. Hence, we obtained the unique result that the shell thickness is very small, in the order of 0.4 – 0.6 nm, and that the Mn atoms are not uniformly incorporated in the NCs but that there is an accumulation of the Mn atoms in the shell region. Future work would include the production of a set of NCs doped with an array of different Mn concentrations and with a narrower size distribution which would allow a more precise determination of the thickness of the shell and of the distribution of the incorporated Mn between the core and the shell. Additionally, the variation of the FS parameter *D* could be more clearly understood by an estimation of the different and partly compensating contributions to the zero-field splitting, through independent measurements of the local distortion of the regular ZnO lattice structure by the incorporation of Mn in ZnO NCs.

To clarify the role of charge carriers in mediating ferromagnetic interactions, the magnetic and structural properties of Mn and Al or Co and Al co-doped ZnO films grown by PLD were investigated. The Mn doped ZnO samples were clearly paramagnetic, the Mn ions being substitutional on Zn sites. On the other hand, the EPR signature of substitutional Co^{2+} on Zn sites was not found in the Co doped samples. Instead, the magnetic characterization through several techniques, namely electron magnetic resonance (EMR), SQUID, magnetoresistance and Hall effect pointed to some kind of ferromagnetic order in the Co doped samples. Nevertheless, since the Co content is very large and the EPR investigations clearly show that the Co is not incorporated as substitutional Co^{2+}, we believe that the formation of small precipitates, second phases, or spinodal decomposition, is the origin of the observed weak ferromagnetism. To

confirm our suspects, further work is needed, and measurements of the X-ray photoelectron spectroscopy (XPS) are underway to clear the valence state of the Co atoms (ions).

The ZnO nanostructures grown by different methods exhibited good crystalline quality. No evidence of carrier mediated ferromagnetism was observed in any case. Our experiments show that the EPR analysis allows us to directly demonstrate whether and where the TM ions are incorporated and evidence the importance of the surface effects at material dimensions below ≈15 nm, for which core-shell structures are formed.

Comparative investigations of Fe alloyed ZnO films grown by PIMOCVD were performed. As expected, for $x > 0.25$, second phases of spinel and iron oxide were found by XRD. All samples exhibited ferromagnetic hysteresis loops at 300 K, and for the films with iron content $x \leq 0.25$ the temperature dependence of the magnetization showed an antiferromagnetic transition at 10 K attributed to the presence of the normal spinel $ZnFe_2O_4$ phase. Ferromagnetic resonance (FMR) and SQUID measurements confirmed the existence of a ferromagnetic behaviour at temperatures at least up to 400 K, which is compatible with the presence of both Fe_3O_4 and the inverted $ZnFe_2O_4$ spinel formed in the ZnO layers. The intensity of the FMR signal increased with increasing Fe content. Between $x = 0.50$ and $x = 0.86$ a change of the magnetic phase occurred, leading to a different behaviour of the magnetization vs. temperature and to the appearance of a new FMR spectrum. These results support the indication that secondary phases are accountable for the magnetic behaviour detected in many systems.

In general, the studies carried out in ZnO based structures revealed that the investigated samples didi not exhibit intrinsic DMS behaviour, and that comprehensive investigations are needed to assert the nature of the observed magnetic properties. Nevertheless, there are possibilities for applying ZnO based magnetic materials in the spintronic technology, since the extrinsic magnetism may still be revealed as controllable and tuneable by growth parameters, co-doping and post growth treatments. A possibility is a hybrid system in which NCs are embedded and self-organized in the ZnO host [Dietl (2007)]. Here, the NC type, size, and distribution have to be controlled for applications. Further investigations in this area are needed for novel room-temperature device development to be possible.

Recent investigations [Pan (2007), Zhou (2008c)] turned the spotlight to d^0 ferromagnetism, were oxygen related defects are a prime suspect as the source of the observed magnetic order. This field represents a great opportunity for achieving reproducible results in

order to realize magnetic devices based on ZnO. We personally tried to reproduce the results obtained by Zhou *et al.* (2008c), but we were unfortunately unsuccessful. Nevertheless, further work is necessary to test this possibility, and it is especially important that electronic structure theory and modelling is developed to elucidate the role of structural defects in this kind of magnetic ordering. Combining the possibility of defect based ferromagnetism with the shape and size of nanostructures would trace an interesting path of research for applications in nanotechnology.

The findings of this work evidence the importance of surface effects when dealing with low dimensional materials, such as NCs. The formation of core-shell structures represents a possibility to tune the properties of the surface shell by varying the dopant content and type, while preserving the bulk properties in the core. Another possibility would be to investigate the surface functionalization with specific markers, for instance to track cancerous cells in the human body and help eliminate them.

In summary, the wide band gap DMS based on ZnO, which was thought to be a promising material for the next generation of spin electronic devices, has been carefully studied. Through a comprehensive investigation, this material was shown to not necessarily obey the traditional paradigms applicable to more well-established DMSs, such as $Ga_{1-x}Mn_xAs$. On the other hand, new properties of this material have been explored, revealing that there is still much work to be done and many prospects of applications to be investigated.

BIBLIOGRAPHY

Abragam A and Bleaney A, *Electron Paramagnetic Resonance of Transition Metal Ions* (Oxford University Press, Oxford, United Kingdom, 1986).

Abragam A and Pryce M H L, Proc. Roy. Soc. (London) **A205**, 135 (1951), **A206**, 164, 173 (1951).

Abraham D W, Frank M M, and Guha S, Appl. Phys. Lett., **87**, 252502 (2005).

Ando K, Saito H, Jin Z, Fukumura T, Kawasaki M, Matsumoto Y, and Koinuma H, J. Appl. Phys., **89**, 7284 (2001a).

Ando K, Saito H, Jin Z, Fukumura T, Kawasaki M, Matsumoto Y, and Koinuma H, Appl. Phys. Lett., **78**, 2700 (2001b).

Andrearczyk T, Jarosyński J, Grabecki G, Dietl T, Fukumura T, and Kawasaki M, Phys. Rev. B, **72**, 121309(R) (2005).

Ankiewicz A O, Carmo M C, Sobolev N A, Gehlhoff W, Kaidashev E M, Rahm A, Lorenz M, Grundmann M, J. Appl. Phys., **101**, 024324 (2007).

Baselgia L, Warden M, Waldner F, Hutton L, Drumheller E, He Y Q, Wigen P E, Maryško M, Phys. Rev. B, **38**, 2237 (1988).

Belghazi Y, Stoeffler D, Colis S, Schmerber G, Ulhaq-Bouillet C, Rehspringer J L, Berrada A, Aubriet H, Petersen J, Becker C, Ruch D, and Dinia A, J. Appl. Phys., **105**, 113904 (2009).

Blasco J, Bartolome F, Garcia L M, Garcia J, J. Mater. Chem., **16**, 2282 (2006).

Bleany B, Trenam R S, Proc. R. Soc. A, **228**, 157 (1955).

Blundell S, *Magnetism in Condensed Matter* (Oxford University Press Inc., New York, United States,2001).

Borse P H, Srinivas D D, Shinde R F, Date S K, Vogel W, and Kilkarni S K, Phys. Rev. B, **60**, 8659 (1999).

Bruno P, Phys. Ver. B, **39**, 865 (1989).

Bundesmann C, Schubert M, Spemann D, Butz T, Lorenz M, Kaidashev E M, Grundmann M, Ashkenov N, Neumann H, and Wagner G, App. Phys. Lett., **81**, 2376 (2002).

Bundesmann C, Rahm A, Lorenz M, Grundmann M, and Schubert M, J. Appl. Phys., **99**, 113504 (2006).

Cao B Q, Lorenz M, von Wenckstern H, Czekalla C, Brandt M, Lenzner J, Benndorf G, Biehne G, Grundmann M, Proc. SPIE, **6895**, 68950V (2008a).

Cao B, Lorenz M, Brandt M, von Wenckstern H, Lenzner J, Biehne G, Grundmann M, Phys. Stat. Sol.(RRL), **2**, 37 (2008b).

Castel V, Youssef J B, and Brosseau C, J. Nanomater., 27437 (2007).

Chambers S A, Surface Science Reports, **61**, 345 (2006).

Chia C H, Makino H, Tamura K, Segawa Y, Kawasaki M, Ohtomo A, and Koinuma H, Appl. Phys. Lett., **82**, 1848 (2003).

Chiba D, Sawicki M, Nishitani Y, Nakatani Y, Matsukura F, and Ohno H, Nature, **455**, 515 (2008).

Cho Y M, Choo W K, Kim H, Kim D and Ihm Y E, Appl. Phys. Lett,. **80**, 3358 (2002).

Chye Y, White M E, Johnson-Halperin E, Gerardot B B,Awschalom D D, Petroff P M, Phys. Rev. B, **66**, 201301(R) (2002).

Claflin B, Look D C, Park S J, and Cantwell G, J. Cryst. Growth, **287**, 16 (2006).

Coey J M D, Venkatesan M, Fitzgerald C B, Nat. Mater., **4**, 1763 (2005).

Coey J M D, and Chambers S A, MRS Bulletin, **33**, 1053 (2008).

de la Cruz R M, Pareja R, Gonzalez R, Boatner L A, and Chen Y, Phys. Rev. B, **45**, 6581 (1992).

Denardin J C, Knobel M, Zhang X X, Pakhamov A B, J. Magn. Magn. Mater., **262**, 15 (2003).

Denninger G, Minirock V3.4, (05.04.2006) (private communication).

Diaconu M, Schmidt H, Hochmuth H, Lorenz M, Benndorf G, Lenzner J, Spemann D, Setzer A, Nielsen K W, Esquinazi P and Grundmann M, Thin Solid Films **486**, 117 (2005a).

Diaconu M, Schmidt H, Pöppl A, Böttcher R, Hoentsch J, rahm A, Hochmuth H, Lorentz M, Grundmann M, Phys. Rev. B, **72**, 085214 (2005b).

Diaconu M, Schmidt H, Pöppl A, Böttcher R, Hoentsch J, Rahm A, Hochmuth H, Lorenz M and Grundmann M, Superlattices Microstruct., **38**, 413 (2005c).

Diaconu M, Schmidt H, Hochmuth H, Lorenz M, Benndorf G, Spemann D, Setzer A, Esquinazi P, Pöppl A, von Wenckstern H, Nielsen K-W, Gross R, Schmidt H, Mader W, Wagner G, and Grundmann M, J. Mag. Mag. Mat., **307**, 212 (2007).

Dietl T, Ohno H, Matsukura M, Cibert J, and Ferrand D, Science, **287**, 1019 (2000).

Dietl T, J. Phys.: Condens. Matter., **19**, 165204 (2007).

Edmonds K W, Farley N R S, Johal T K, van der Laan G, Campion R P, Gallagher B L, Foxon C T, Phys. Rev. B, **71**, 064418 (2005).

Erwin S C, Hellberg C S, Phys. Rev. B, **68**, 245206 (2003).

Esteves A C C, Barros-Timmons A, Monteiro T and Trindade T, J. Nanosc. Nanotech., **5**, 766 (2005).

Estle T and De Wit M, Bull Am. Phys. Soc., **6**, 445 (1961).

Fassbender J and McCord J, J. Magn. Magn. Mater., **320**, 579 (2008).

Fukumura T, Jin Z, Kawasaki M, Shono T, Hasegawa T, Koshihara S and Koinuma H, Appl. Phys. Lett. **78**, 958 (2001).

Furdyna J K, J. Appl. Phys., **64**, R29 (1988).

Gehlhoff W, Azamat D, and Hoffmann A, Phys. Stat. Sol. (b), **243**, 687 (2006).

Gehlhoff W, private communication (2008).

Gehlhoff W, unpublished.

Ghosh S, Sih V, Lau W H, Awschalom D D, Bae S-Y, Wang S, Vaidya S, and Chapline G, Appl. Phys. Lett,. **86**, 232507 (2005).

Han S-J, Song J W, Yang C H, Park S H, Appl. Phys. Lett., **81,** 4212 (2002).

Han S-J, Jang T-H, Kim Y B, Park B G, Park J H, and Jeong Y H, Appl. Phys. Lett., **83**, 920 (2003).

Hausmann A and Huppertz H, J. Phys. Chem. Solids **29**, 1369 (1968).

Heo Y W, Ivill M P, Ip K, Norton D P and Pearton S J, Appl. Phys. Lett., **84**, 2292 (2004a).

Heo,Y W, Norton D P, Tien L C, Kwon Y, Kang B S, Ren F, Pearton S J, and LaRoche J R, Materials Science and Engineering, **R 47**, 1 (2004b).

Higgins J S, Shinde S R, Ogale S B, Venkatesan T, and Greene R L, Phys. Rev. B, **69**, 073201 (2004).

Horng L, Chern G, Chen M C, Kang P C, and Lee D S, J. Magn. Magn. Mater., **270**, 389 (2004).

Iwata K, Sakemi T, Yamada A, Fons P, Awai K, Yamamoto T, Shirakata S, Matsubara K, Tampo H, Sakurai K, Ishizuka S, and Niki S, Thin Solid Films, **480**, 199 (2005).

Jagadish C, and Pearton, *Zinc oxide bulk, thin films and nanostructures: processing, properties and applications* (Elsevier, Oxford, Unietd Kingdom, 2006).

Janotti A, and Van de Walle C G, Appl. Phys. Lett., **87**, 122102 (2005).

JCPDS - International Centre for Diffraction Data, No. 19-0629.

JCPDS - International Centre for Diffraction Data, No. 22-1012.

Jedrecy N, Bardeleben H J, Zheng Y, and Cantin J-L, Phys. Rev. B, **69**, 041308(R) (2004).

Jin Z, Fukumura T, Kawasaki M, Ando K, Saito H, Sekiguchi T, Yoo Y Z, Murakami M, Matsumoto Y, Hasegawa T, Koinuma H, Appl. Phys. Lett., **78**, 3824 (2001).

Ju-Fen L, Xiao-Yu K, Ai-JieM, Xiao-Ming T, Chemical Physics Letters, **429**, 266 (2006).

Jung S W, An S-J, Yi G-C, Jung C U, Lee S I and Cho S, Appl. Phys. Lett., **80**, 4561 (2002).

Kale S, Bhagat S M, Lofland S E, Scabarozi T, Ogale S B, Orozco A, Shinde S R, Venkatesan T, Hannoyer B, Mercey B, and Prellier W, Phys. Rev. B, **64**, 205413 (2001).

Kane M H, Shalini K, Summers C J, Varatharajan R, Nause J, Vestal C R, Zhang Z J and Ferguson I T, J. Appl. Phys. **97**, 023906 (2005).

Kaspar T C, Droubay T, Heald S M, Nachimuthu P, Wang C M, Shutthanandan V, Johnson C A, Gamelin D R, and Chambers S A, New J. Phys., **10**, 055010 (2008a).

Kaspar TC, Droubay T, Heald S M, Engelhard M H, Nachimuthu P, and Chambers S A, Phys. Rev. B, **77**, 201303(R) (2008b).

Katayama-Yoshida H, Sato K and Yamamoto T, JSAP Int., **6**, 20 (2002).

Kennedy T K, Glaser E R, Klein P B, and Bhargava R N, Phys. Rev. B, **52**, R14356 (1995).

Kim J H, Kim H, Ihm Y E and Choo W K, J. Appl. Phys., **92**, 6066 (2002).

Kim J H, Kim H, Kim D, Ihm Y E, and Choo W K, Physica B, **327**, 304 (2003).

Kittel C., *Introduction to Solid State Physics* (John Wiley & Sons, New York, USA, 1996).

Kittilstved K R, Norberg N S, and Gamelin D R, Phys. Rev. Lett., **94**, 147209 (2005).

Klug H P and Alexander L E, *X-Ray Diffraction Procedure for Polycrystalline and Amorphous Materials* (second ed., Wiley, New York, USA, 1974).

Kneubühl F K, J. Chem. Phys., **33**, 1074 (1960).

Koh A K, Miller D J, and Grainger C T, Phys. Rev. B **29**, 4904 (1984).

Koidl P, Phys. Rev. B, **15**, 2493 (1977).

Kolesnik S, and Dabrowski B, J. Appl. Phys., **96**, 5379 (2004).

Koteski V, Zhou H, Farangis B, Hofmann D M, Meyer B K, and Mahnke H-E, Phys. Stat. Sol. (b), **244**, 1578 (2007).

Kreissl J, Gehlhoff W, Omling P, and Emanuelsson P, Phys. Rev. B, **42** 1731 (1990).

Kuang X Y, Phys. Lett., **A213**, 89 (1996).

Kuang X Y, and Chen Z H, Phys. Rev B, **36**, 712 (1987).

Kundaliya D C, Ogale S, Lofland S E, Dhar S, Metting C J, Shine D R, Ma Z, Varughese B, Ramanujachary K V, Salamanca-Riba L, Venketesan T, Nat. Mater., **3**, 709 (2004).

Landolt-Boernstein, *Numerical Data and Functional Relationships in Science and Technology*, (New Series, Vol. III 19a, Magnetic Properties of Metals, Springer, 1986).

Lee H-J, Jeong S-Y, Cho C R and Park C H, Appl. Phys. Lett., **81**, 4020 (2002).

Lee W, Jeong M C and Myoung J M, Appl. Phys. Lett., **85**, 6167 (2004).

Lenz K, Kosubek E, Baberschke K, and Wende H, Phys. Rev. B, **72**, 144411 (2005).

Lin C C, Chen H P and Chen S Y, Chem. Phys. Lett., **404**, 30 (2004).

Liu K, Chien C L, Searson P C and Yu-Zhang K, Appl. Phys. Lett., **73**, 1436 (1998).

Liu C H, Yiu W C, Au F C K, Ding J X, Lee C S, and Lee S T, Appl. Phys. Lett., **83**, 3168 (2003).

Liu C, Yun F and Morkoç H, J. Mat. Sci.: Mat in Elect., **16**, 555 (2005).

Liu X X, Lin F T, Sun L L, Cheng W J, Ma X M, Shi W Z, Appl. Phys. Lett., **88**, 062508 (2006).

Look D C, Semicond. Sci. Technol., **20**, S55 (2005a).

Look D C, Farlow G C, Reunchan P, Limpijumnong S, Zhang S B, and Nordlund K, Phys. Rev. Lett., **95**, 225502 (2005b).

Lorenz M, Kaidashev E M, Rahm A, Nobis Th, Lenzner J, Wagner G, Spemann D, Hochmuth H, and Grundmann M, Appl. Phys. Lett., **86**, 143113 (2005).

Lorenz M, *Pulsed Laser Deposition of ZnO-based Thin Films*, chapter 7 in: Ellmer K, Klein A, and Rech B (eds.), *Transparent Conductive Zinc Oxide Basics and Applications in Thin Film Solar Cells"* (Springer Series in Materials Science Vol. 104, Berlin, Germany, 2008).

Lou J, Liang J K, Liu Q LF S, Zhang Y, Sun B J, and Rao G H, J. Appl. Phys., **97**, 086106 (2005).

Low W, Phys. Rev., **105**, 793 (1957).

Maensiri S, Laokul P, and Promarak V, Journal of Crystal Growth, **289**, 102 (2006).

Mandal S K, Das A K, Nath T K, and Karmakar D, Appl. Phys. Lett., **89**, 144105 (2006).

Martins M A, Neves M C, Esteves A C C, Girginova P I, Guiomar A J, Amaral V S and Trindade T, Nanotechnology, **18**, 215609 (2007).

Matsukura F, Ohno H, Shen A, Sugawara Y, Phys. Rev. B, **57,** R2037 (1998).

Matsumoto Y, Murakami M, Shono T, Hasegawa T, Fukumura T, Kawasaki M, Ahmet P, Chikyow T, Koshihara S-Y, Koinuma H, Science, **291**, 854 (2001).

Nazmul A M, Sugahara S, Tanaka M, arXiv:cond-mat/0208299v1, (2002).

Neamen D A, *Semiconductor Physics and Devices: Basic Principles* (McGraw-Hill, New York, USA, 2003).

Newman D J, and Ng B, Rep. Prog. Phys., **52**, 699 (1989).

Ney A, Kammermeier T, Ney V, Ollefs K, and Ye S, J. Magn. Magn. Mater., **320**, 3341 (2008).

Norberg N S, Kittilstved K R, Amonette J E, Kukkadapu R K, Schwartz D A and Gamelin D R, J. Am. Chem. Soc., **126**, 9387 (2004).

Norton D P, Overberg M E, Pearton S J, Pruessner K, Budai J D, Boatner L A, Chisholm M F, Lee J S, Khim Z G, Park Y D, and Wilson R G, Appl. Phys. Lett., **83**, 5488 (2003a).

Norton D P, Pearton S J, Herbard A F, Theodoropoulou N, Boatner L A and Wilson R G, Appl. Phys. Lett., **82**, 239 (2003b).

Ohno H, Young D K, Beschoten B, Matsukura F, Ohno K, Awschalom D D, Nature, **402**, 790 (1999)

Ono T, Miyajima H, Shigeto K, Mibu K, Hosoito N, and Shinjo T, Science, **284**, 468 (1999).

Özgür U, Alivov Y I, Liu C, Tke A, Reschikov M A, Dogan S, Avrutin V, Cho S J, and Morkoc H, J. Appl. Phys., **98**, 041301 (2005).

Pake G E, J. Chem. Phys., **16**, 327 (1948).

Pan H, Yi J B, Shen L, Wu R Q, Yang J H, Jin J Y, Feng Y P, Ding J, Van L H, and Yin J H, Phys. Rev. Lett., **99**, 127201 (2007).

Pan F, Song, C, Liu X J, Yang Y C, and Zeng F, Mater. Sci. Eng. R, **62**, 1 (2008).

Pereira R N, *Estudo de Defeitos Paramgnéticos em Diamante*(phD thesis,Univesity of Aveiro, Portugal, 2002).

Philip J, Gnanaprakash G, Panneerselvam G, Antony M P, Jayakumar T, and Raj B, J. Appl. Phys., **102**, 054305 (2007).

Philipose U, Nair S V, Trudel S, de Souza S F, Aouba S, Hill R H, and Ruda H E, Appl. Phys. Lett., **88**, 263101 (2006).

Pilbrow J R, *Transition Ion Electron Paramagnetic Resonance* (Oxford University Press, Oxford, United Kingdom, 1990).

Poole C P, *Electron Paramagnetic Resonance: A Comprehensive Treatise on Experimental Techniques*

(Dover Publications, Inc., Mineola, New York, USA, 1983).

Radovanovic P V, Gamelin D R, Phys. Rev. Lett., **91**, 157202 (2003).

Raebiger H, Lany S, and Zunger A, Phys. Rev. B, **79**, 165202 (2009).

Rahm A, Kaidashev E M, Schmidt H, Diaconu M, Pöppl A, Böttcher R, Meinecke C, Butz T, Lorenz M, and M. Grundmann, Microchim Acta, **156**, 21 (2006).

Risbud A S, Spaldin N A, Chen Z Q, Stemmer S, Seshadri R, Phys. Rev. B, **68**, 205202 (2003).

Saeki H, Tabata H and Kawai T, Solid State Commun., **120**, 439 (2001).

Saitoh E, Nature, **455**, 474 (2008).

Salzer R, Spemann D, Esquinazi P, Hohne R, Setzer A, Schindler K, Schmidt H, and Butz T, J. Magn.Magn. Mater., **317**, 53 (2007).

Sands R H, Phys. Rev., **99**, 1222 (1955).

Sato K and Katayama-Yoshida H, Jpn. J. Appl. Phys., Part 2, **39**, L555 (2000).

Schiessl W, Potzel W, Karzel H, Steiner M, Kalvius G M, Martin A, Krause M K, Halevy I, Gal J, Schäfer W, Will G, Hillberg M, and Wäppling R, Phys. Rev. B, **53**, 9143 (1996).

Schneider J, Sircar S R, and Räuber A, Z. Naturforschung **18 a**, 980 (1963); Schneider J and Sicar S R, Z. Naturforschung, **17 a**, 570 (1962), **17 a**, 651(1962).

Schwartz D A, Norberg N S, Nguyen Q P, Parker J M and Gamelin D R, J. Am. Chem. Soc., **125**, 13205 (2003).

Sellmyer D J, Zheng M and Skomski R, J. Phys.: Cond. Matter, **13**, R433 (2001).

Sénateur J-P, and Dubourdieu C, Weiss F, Rosina M, Abrutis A, Adv. Mater. Opt. Electron., **10** 155 (2000).

Sharma P, Gupta A, Rao K V, Owens F J, Sharma R, Ahuja R, Osorio Guillen J M, Johansson B and Gehring G A, Nature Mater., **2**, 673 (2003).

Shim J H, Hwang T, Lee S, Park J, Han S-J, and Jeong Y H, Appl. Phys. Lett., **86**, 082503 (2005).

Shinagawa T, Izaki M, Inui H, Murase K, AND Awakura Y, Chem. Mater., **18**, 763 (2006).

Shinde S R, Ogale S B, Higgins J S, Zheng H, Millis A J, Kulkarni V N, Ramesh R, Greene R L, Venkatesan T, Phys. Rev. Lett., **92**, 166601 (2004).

Simanek E, and Müller K A, J. Phys. Chem. Solids, **31**, 1027 (1970).

Song C, Geng K W, Zeng F, Wang X B, Shen Y X and Pan F, Phys. Rev. B, **73**, 024405 (2006).

Stoll S and Schweiger A, J. Magn. Reson., **178**, 42 (2006).

Story T, Galazka R R, Frankel R B, Wolf P A, Phys. Rev. Lett., **56**, 777 (1986).

Thomas D G, J. Phys. Chem. Solids, **3**, 229 (1957).

Title R, Phys. Rev., **130**, 17 (1963).

Tiwari A, Jin C, Kvit A, Kumar D, Muth J F, Narayan J, Solid State Commun., **121**, 371 (2002).

Triboulet R, and Perriere J, Prog. Cryst. Growth Charact. Mater. , **47**, 65 (2003).

Tsukazaki A, Ohtomo A, Onuma T, Ohtani M, Makino T, Sumiya M, Ohtani K, Chichibu S F, Fuke S, Segawa Y, Ohno H, Koinuma H, and Kawasaki M, Nat. Mater., **4**, 42 (2005).

Tuan A C, Bryan J D, Pakhamov A B, Shutthanandan V, S. Thevuthasan, McCready D E, Gaspar D, Engelhard M H, Rogers Jr. J W, Krishnan K M, Gamelin D R, Chambers S A, Phys. Rev. B, **70**, 054424 (2004).

Tuomisto F, Saarinen K, Look D C, and Farlow G C, Phys. Rev. B, **72**, 085206 (2005).

Ueda K, Tabat H and Kawai T, Appl. Phys. Lett., **79**, 988 (2001).

Vainshtein B K, *Fundamentals of Crystals* (Springer-Verlag, Berlin-Heidelberg-New York, 1994).

van der Heijden P A A, van Opstal M G, Swiiste C H W, Bloemen P H J, Gaines J M, and de Jonge W J M, J. Magn. Magn. Mater., **182**, 71 (1998).

van Dorpe P, Liu Z, van Roy W, Motsnyi V F, Sawicki M, Borghs G, de Boeck J, Appl. Phys. Lett., **84**, 3495 (2004).

van Vleck J H, *Electric and Magnetic Susceptibilities* (Oxford University Press, Oxford, United Kingdom, 1932).

Venkatesan M, Fitzgerald C B, Lunney J G, and Coey J M D, Phys. Rev. Lett., **93**, 177206 (2004).

Verdes C G, Ruiz-Diaz B, Thompson S M, Chantrell R W, and Stancu Al., J. Appl. Phys., **89**, 7475 (2001).

Viswannatha R, Sapra S, Gupta S S, Satpati B, Satyam P V, Dev B N, and Sarma D D, J .Phys. Chem. B, **108,** 6303 (2004).

Volbers N, Zhou H, Knies C, Pfisterer D, Sann J, Hofmann D M and Meyer B K, Appl. Phys. A, **88**, 153 (2007).

von Bardeleben H J, Jedrecy N, and Cantin J L, Appl. Phys. Lett., **93**, 142505 (2008).

Vonsovskii S, *Ferromagnetic Resonance* (Pergamon Press, Oxford, United Kingdom, 1966).

Wakano T, Fujimura N, Morinaga Y, Abe N, Ashida A and Ito T, Physica E, **10**, 260 (2001).

Wang Z L, J. Phys.: Condens. Matter, **16**, R829 (2004).

Wan-Lun Y, and Min-Guang Z, Phys. Rev. B, **37**, 9254 (1988).

Weil J A, Bolton J R, and Wertz J E, *Electron Paramagnetic Resonance: Elementary Theory and Practical Applications* (John Wiley & Sons, Inc., New York, USA, 1994).

Williamson G K and Hall W H, Acta Metall., **1**, p. 22 (1953).

Wolcott A, Smith W A, Kuykendall T R, Zhao Y, and Zhang J Z, Adv. Funct. Mater., **19**, 1 (2009).

Xiang B, Wei P, Zhang X, Dayeh S A, Aplin D P R, Soci C, Yu D and Wang D, Nano Lett., **7**, 323 (2007).

Xu Q, Hartmann L, Schmidt H, Hochmuth H, Lorenz M, Schmidt-Grund R, Sturm C, Spemann D, and Grundmann M, Phys. Rev. B, **73**, 205342 (2006).

Xu Q, Hartmann L, Schmidt H, Hochmuth H, Lorenz M, Schmidt-Grund R, Sturm C,

Spemann D, and Grundmann M, J. Appl. Phys., **101**, 063918 (2007a).

Xu Q, Hartmann L, Schmidt H, Hochmuth H, Lorenz M, Spemann D, and Grundmann M, Phys. Rev. B, **76**, 134417 (2007b).

Xu Q, Hartmann L, Zhou S, Mcklich A, Helm M, Biehne G, Hochmuth H, Lorenz M, Grundmann M, and Schmidt H, Phys. Rev. Lett., **101**, 076601 (2008a).

Xu Q, Schmidt H, Hochmuth H, Lorenz M, Setzer A, Esquinazi P, Meinecke C, and Grundmann M, J. Phys. D: Appl. Phys., **41**, 105012 (2008b).

Xu Q, Schmidt H, Zhou S, Potzger K, Helm M, Hochmuth H, Lorenz M, Setzer A, Esquinazi P, Meinecke C, and Grundmann M, Appl. Phys. Lett., **92**, 082508 (2008c).

Xu Q, Zhou S, Markó D, Potzger K, Fassbender J, Vinnichenko M, Helm M, Hochmuth H, Lorenz M, Grundmann M, and Schmidt H, J. Phys. D: Appl. Phys., **42**, 085001 (2009).

Yoon S W,Cho S-B, We S C, Yoon S, Suh B J, Song H K, and Shin Y J, J. Appl. Phys., **93**, 7879 (2003).

Yu C, Li D, Pearson J and Bader S D, Appl. Phys. Lett., **79**, 3848 (2001).

Zener C, Phys. Rev., **81**, 440 (1951a).

Zener C, Phys. Rev., **82**, 403 (1951b).

Zener C, Phys. Rev., **83**, 299 (1951c).

Zhang S B, Wei S-H, and Zunger A, Phys. Rev. B, **63**, 075205 (2001).

Zhang Y, Yan S, Liu Y, Tian Y, Liu G, Chen Y, Mei L, and Liu J P, Sol. State Commun., **140**, 405 (2006).

Zheng W-C, Wu S-Y, and ZiZ J, Naturforsch., **56 a**, 473 (2001).

Zhidomirov G M, Lebedev Ya S, Dobryakov S N, Shteinshneider N Ya, Chirkov A K, and Gubanov V A, *Interpretation of complex EPR spectra* (Oxonian Press, New Delhi, India, 1985).

Zhou H, Alves H, Hofmann D M, Kriegseis W, Meyer B K, KaczMarczyk G, and Hoffmann A, Appl. Phys. Lett., **80**, 210 (2002).

Zhou H, Hofmann D M, Hofstaetter A, and Meyer B K, J. Appl. Phys., **94**, 1965 (2003).

Zhou S, Potzger K, Zhang G, Eichhorn F, Skorupa W, Helm M, and Fassbender J, J. Appl. Phys., **100**, 114304 (2006a).

Zhou H, Hofmann D M, Alves H R, and Meyer B K, J. Appl. Phys., **99**,103502 (2006b).

Zhou S, Potzger K, Talut G, Reuther H, von Borany J, Grötzschel R, Skorupa W, Helm M, and Fassbender J, Volbers N, Lorenz M, and Herrmannsdörfer T, J. Appl. Phys., **103,** 023902 (2008a).

Zhou S, Potzger K, Talut G, Reuther H, Kuepper K, Grenzer J, Xu Q, Mücklich A, Helm M, Fassbender J, and Arenholz E, J. Phys. D: Appl. Phys., **41**, 105011 (2008b).

Zhou S, Xu Q, Potzger K, Talut G, Grötzschel R, Fassbender J, Vinnichenko M, Grenzer J, Helm M, Hochmuth H, Lorenz M, Grundmann M, and Schmidt H, Appl. Phys. Lett., **93**, 232507 (2008c).